Archean Paleosols on Earth and Mars

Dissertation zur Erlangung des Doktorgrades der Naturwissenschaften des Fachbereichs für Geowissenschaften der

Freien Universität Berlin

vorgelegt von Sami Nabhan

Freie Universität Berlin

Berlin, August 2016

Diese Arbeit wurde vom Promotionsausschuss des Fachbereichs Geowissenschaften am 28. April 2016 genehmigt.

Erstgutachter:	Prof. Dr. Ralf Jaumann Freie Universität Berlin Deutsches Zentrum für Luft- und Raumfahrt
Zweitgutachterin:	Prof. Dr. Anne Bernhard Freie Universität Berlin
Drittgutachter:	Prof. Dr. Christoph Heubeck Friedrich-Schiller-Universität Jena

Tag der Disputation: 06.01.2017

Erklärung

Hiermit erkläre ich, Sami Nabhan, dass diese Arbeit ausschließlich auf Grundlage der angegebenen Hilfsmittel und Hilfen selbstständig von mir verfasst wurde. Diese Arbeit ist nicht in einem früheren Promotionsverfahren eingereicht worden.

Berlin, den 04. August 2016

Sami Nabhan

Kurzfassung

Paleoböden sind hervorragend geeignet, um physikalische und chemische Prozesse an der Schnittstelle zwischen Gestein und der Atmosphäre, der Hydrosphäre und der Biosphäre zu dokumentieren; sie dienen somit als Informationsspeicher der Vergangenheit. Dies ist besonders im Archaikum wichtig, als dramatische Änderungen der Umwelt, wie kratonales Wachstum, atmosphärischer Umbau und die Entstehung einer Biosphäre stattfanden. Archaische Paleoböden sind jedoch aufgrund von starker Deformation, Metamorphose und limitierter Aufschlüsse oft schwer als solche zu erkennen und zu charakterisieren, obwohl die Anzahl neuer Funde in den letzten Jahrzehnten stark zugenommen hat. Gut erhaltene palaeoarchaische, randmarine und terrigene Abfolgen sind derzeit lediglich aus dem Pilbara Block in Nordwest-Australien und dem Barberton Greenstone Belt (BGB) des Kaapvaal-Kratons im südlichen Afrika bekannt.

Diese Arbeit beschreibt kartierbare frühdiagenetische bis pedogene Konkretionen, die sich in Sanden fluviatiler Küstenebenen bildeten und in der ~3.22 Ga alten Moodies-Gruppe des BGB in Südafrika erhalten sind. Sie treten teilweise gesteinsbildend in mehreren Einheiten auf und bestehen aus Megaquarz-Pseudomorphosen nach Gips, Baryt und Kalzit. Ansammlungen der Konkretionen sind stratiform und oft assoziierbar mit fluviatil umgelagerten, feinklastischen, tuffigen Sedimenten rhyodazitischer Zusammensetzung. Sie können zu faustgroßen Agglomeraten zusammenwachsen und bilden Horizonte von mehreren zehner Metern lateraler Ausdehnung. Verwitterung von Feldspäten und tuffigem Material lieferte alkalische Kationen wie Ca^{2+}, Ba^{2+} und K^{+}, während Karbonat wahrscheinlich durch Silikatverwitterung mafischer bis ultramafischer Vulkanite in Kontakt zur CO_2-reichen Atmosphäre entstand. Das Konkretionswachstum fand offenbar unter pedogenen bis frühdiagenetischen Bedingungen in lockerem, grobem Sediment in der vadosen Zone statt und wurde von saisonalen Fluktuationen des Grundwasserspiegels unter evaporitischen Bedingungen dominiert. Die Konkretionen repräsentieren wahrscheinlich die ältesten bisher bekannten terrestrischen Evaporite und sind Teil der ältesten bekannten komplexen Paleoböden. Ihre Entstehung und Zusammensetzung belegen das lokale Auftreten von Sulfat in der archaischen Atmo- und Hydrosphäre, ihre Wechselwirkung mit der entstehenden Biosphäre, dem Verwitterungsregime, dem lokalen Klima und der Hydrodynamik der vadosen Zone.

Die pedogenen Konkretionen der Moodies-Gruppe sind mit mm- dünnen, überwiegend aus Pyrit bestehenden Schwerminerallaminae wechselgelagert. Diese Pyrite zeigen gerundete, detritische Kerne, die durch Porenwässer, verbunden mit der Entstehung der Konkretionen, korrodiert sind,

und idiomorphe Anwachssäume, welche unter reduzierenden Bedingungen entstanden. Die Spurenelement-Gehalte (Ni und Co) und $\delta^{34}S$ Verhältnisse der Säume unterscheiden sich eindeutig von denen der Kerne. Während die Kerne niedrige Co- und Ni-Gehalte und ein hohes Co/Ni-Verhältnis zeigen, enthalten die Säume bis zu 5,5 Gew.-% dieser Elemente mit niedrigem Co/Ni-Verhältnis, was auf die Verwitterung naheliegender ultramafischer Gesteine hindeutet. In-situ Schwefelisotopen- Analysen der Pyritkerne zeigt $\delta^{34}S_{VCDT}$ (Vienna Canyon Diablo troilit) Werte zwischen +5‰ und -5‰, während die Säume $\delta^{34}S_{VCDT}$ Werte zwischen -20‰ und -24.5‰ aufweisen und damit auf *biogene* Fraktionierung des Schwefels hindeuten. Die räumliche Nähe und fast zeitgleiche Entstehung pedogener Sulfate und sekundärer Pyritsäume ist deshalb plausibel mit mikrobieller Verarbeitung von Schwefel in Paläoböden, welche reduzierten und $\delta^{34}S$-verarmten Schwefel lieferten, in Verbindung zu bringen. Dies zeigt, dass bodenbildende Prozesse in küstennahen vadosen Zone des Archaikums nicht nur physikalische und chemische, sondern auch biogene Veränderungen des Lockersediments umfassten. Mikrobielles Leben war in der feuchten vadosen Zone terrestrischer Ablagerungsräume vor 3.2 Ga bereits fest verankert.

Die ~3.3-3.2 Ga alte Sheepbed-Lage der Yellowknife Bay Formation im Gale Crater auf dem Mars enthält mehrere diagenetische Ausbildungen, unter denen die Sheepbed Nodules und erhöhte Rippen als frühdiagenetisch gelten. Beide zeigen chemische Variationen sowohl zueinander als auch zum Sheepbed Tonstein. Die Nodules haben (ähnlich zu denen der etwa gleichalten Paleoböden der Moodies Gruppe) drei morphologisch unterschiedliche Ausprägungen: massiv, hohl und hohl, aber gefüllt. In beiden Orten entstanden sie zudem pedogen bis frühdiagenetisch unter ähnlichen Bedingungen. Die Moodies-Konkretionen sind deshalb ein exzellentes Erd-Analog für die Sheepbed Nodules auf dem Mars. Frühdiagenetischer Pyrit, der mit diesen Nodules, wie in der Moodies-Gruppe, assoziiert sein könnten, ist mit der instrumentellen Ausstattung von Curiosity nicht belegbar. Seine Isotopie wäre, wiederum analog zu der der Moodies-Gruppe, von hohem wissenschaftlichen Interesse.

Abstract

Paleosols are unique recorders of physical and chemical processes at the interface between rocks and the atmosphere, hydrosphere and biosphere. Their capacity to record atmospheric and hydrologic conditions allows them to serve as archives of information on past environments, which is especially relevant in the Archean that saw dramatic changes in environmental parameters such as cratonic development, atmospheric changes and the emergence of the biosphere. Archean paleosols are, due to extensive deformation, metamorphism and limited outcrop, commonly difficult to recognize and characterize, though the number of findings has increased remarkably over recent decades. Well-preserved Paleoarchean marginal marine and terrestrial strata are currently known only from in the Pilbara Block of northwestern Australia and in the Barberton Greenstone Belt (BGB) of the Kaapvaal Craton of southern Africa.

This study describes the widespread, mappable occurrence of early diagenetic to pedogenic nodules that formed in unconsolidated sandy sediments in fluvial and coastal settings of the ~3.22 Ga old Archean Moodies Group, BGB, South Africa. They appear commonly to abundantly, in places rock-forming, in several regionally traceable units and are composed of megaquartz pseudomorphs after gypsum, barite and calcite. Nodule accumulations are stratiform and commonly associated with aqueously reworked, fine-grained, tuffaceous sediment of originally rhyodacitic composition. They can grow to fist-sized agglomerates in crusts tens of m in lateral extent. Weathering of tuffaceous material and feldspar delivered alkali cations such as Ca^{2+}, Ba^{2+} and K^{+}, while carbonates were likely supplied by silicate weathering of mafic to ultramafic volcanic rocks during exposure to a CO_2–rich atmosphere. Nodule growth apparently took place under pedogenic to early diagenetic conditions within unconsolidated granular sediment in the vadose zone, dominated by seasonal fluctuations of the groundwater level under evaporitic conditions. The nodules likely represent the oldest terrestrial evaporites known to date and form part of the oldest known compound paleosols. Their formation and composition constrain the local occurrence of sulfate in the Archean atmo- and hydrosphere, their interaction with the emerging biosphere, Archean weathering regime, local climate, and vadose-zone hydrodynamics.

The pedogenic nodules are associated and interbedded with mm-thick heavy mineral laminations, mainly composed of pyrite. Pyrite grains show rounded detrital cores corroded by pore fluids related to pedogenic nodule formation and secondary idiomorphic rims which grew under reducing conditions. The trace element concentrations (Ni and Co) and $\delta^{34}S$ ratios of the rims are clearly

different from those of the cores. While cores have low Co and Ni concentrations and high Co/Ni-ratios, rims show up to 5.5 wt.-% of these elements and low Co/Ni-ratios, reflecting the weathering of nearby ultramafic rocks. In-situ sulfur isotope analyses of pyrite cores show $\delta^{34}S_{VCDT}$ values between +5‰ and -5‰ while the rims show $\delta^{34}S_{VCDT}$ values between -20‰ and -24.5‰, suggesting biogenic fractionation of sulfur. The close spatial association and nearly contemporaneous formation of pedogenic sulfate nodules and secondary pyrite rims is consistent with microbial sulfur processing in the paleosols which provided reduced and $\delta^{34}S$-depleted sulfur for the growth of authigenic pyrite. This indicates that vadose-zone soil-forming processes in the Archean involved not only physical and chemical modification of unconsolidated sediment but also included its biological modification. Microbial life was already pervasive in the moist vadose zone of terrestrial environments more than 3.2 Ga ago.

The ~3.3-3.2 Ga old Sheepbed Member of the Yellowknife Bay Formation in Gale crater on Mars contains a number of diagenetic features, amongst which nodules and raised ridges are considered to be of early diagenetic origin. Both show low chemical variety in relation to each other and to the Sheepbed mudstone. The nodules show solid, hollow and filled morphologies similar to those of the approximately contemporaneous paleosols of the lower Moodies Group described above. They formed pedogenically to early diagenetically under similar conditions. Moodies nodules are therefore an excellent Earth analog for the formation of the Sheepbed nodules on Mars. The S-isotope data, documenting the involvement of biogenic processes in the formation of the Moodies nodules, strengthens the case for the possibility of extraterrestrial life on Mars. Although Martian pyrite grains and their S-isotopic composition cannot be analyzed using the technical instrumentation of *Curiosity*, their possible existence and isotopic composition should be of high scientific interest.

Acknowledgements

This thesis was supported by many people. My two advisors Christoph Heubeck and Ralf Jaumann initiated the thesis by securing financial support from the DLR (German Aeronautics and Space Research Center) within the Helmholtz Alliance “Planetary Evolution and Life”. They helped also with advice, discussions and any support I asked for. Especially Christoph Heubeck was always available (also on weekends) when I needed his help. Tim Luber, Franziska Scheffler, Michael Wiedenbeck and Ralf Milke helped with the analytical work but also through discussions and fine-tuning the manuscripts. Many helping hands supported me during my field time in South Africa. This hands belong to Tim Luber, Martin Homann, Danielle Zentner, Paul Fugmann, Laura Stutenbecker and Henry Nordhauß, thank you all. Hospitality and help in South Africa for me and the helping hands was provided by the Nel family; thanks, Lily and Adriaan, for being more than just hosts but also friends. And because life always offers good surprises, I thank Tiro Hlanyane, forestry manager who showed me hidden paths and allowed me to stay in his house at several occasions, thank you TC.

After returning from a field seasons with loads of samples, Anna Giribaldi, FU Berlin, managed the processing; thank you for many excellently polished slabs, thin sections and mounts. Sigried Bergmann, FSU Jena, and Christine Fischer, University of Potsdam, are thanked for the preparation of additional thin sections. Stephen Mojzsis (University of Colorado at Boulder) provided Balmat pyrite reference material for S-isotope analysis; Timm John’s encouragement made these measurements possible. Harald Strauss (Universität Münster) allowed me to use his lab to conduct S-isotope measurements.

Last but not least I have to thank a large number of friends and colleagues: Sascha Zertani, Julia Neukampf, Moritz Liesegang, Tina Menneken, Lea Bayet, Jörg Giese, Alessandro Airo, Silvia Favaro, Philip Groß, Carolin Rabethge and others, mainly for being patient with me in the last months. I want also to thank all other members of the Tectonics & Sedimentology- and the Mineralogy & Petrology groups at the Freie Universttät Berlin. And, of course, many thanks to my family, my parents, my sister and the CATS for always being supportive.

Structure and objectives of the thesis

This thesis is a cumulative work mainly based on peer-reviewed publications organized as chapters. The project started in 2012 using the preliminary title "Archean Evaporites on Earth and Mars" as working hypothesis, assuming that the environmental conditions on both planets had been comparable during the Archean and the corresponding Martian eons, the late Noachian and Hesperian. However, the clear differences of the evaporitic deposits on both planets at those times and new findings from the Mars rover *Curiosity* finally led to a thesis related to pedogenic and early diagenetic processes in Archean sedimentary rocks and sedimentary rocks from Gale crater on Mars.

The capacity of paleosols to preserve information on environmental conditions that are linked to the atmo- and hydrosphere at the time of their development makes them an attractive target for the reconstruction of such environments. Evaporites can also preserve and reflect ancient environmental conditions. Therefore, the combination of paleosols and evaporites is the optimal target for the reconstruction of the Archean environment. A major objective of this thesis is to demonstrate that pedogenesis in the Archean included not just the physical and chemical but also already biological changes of the sediment. This and the morphological similarity of pedogenic to early diagenetic nodules found on Mars to those found in the Archean Moodies Group of the Barberton Greenstone Belt shows that Martian rocks that contain such features should be considered as high-priority targets to document former habitable environments.

1. Introduction

The introduction provides a brief overview on the state of the art concerning the exploration of Mars via remote sensing, probes and robotic devices. The geologic timescales of Earth and Mars are compared to show the temporal relation of Martian deposits discussed within the thesis to the Archean sedimentary rocks described here. The subchapter "Archean Evaporites on Earth" describes the current knowledge on evaporitic rocks of Archean age and is published as:

Nabhan, S., (2015). Evaporites, Archean. In: Gargaud, M., Irvine, W.M., Amils, R., Cleaves, H.J., Pinti, D.L., Quintanilla, J.C., Rouan, D., Spohn, T., Tirard, S., Viso, M., (Eds.) Encyclopedia of Astrobiology, Springer, Berlin Heidelberg, p. 765-768. http://dx.doi.org/10.1007/978-3-662-44185-5_5235.

This section is followed by an overview of Archean-equivalent Martian evaporites and a brief statement describing the framework, major questions and objectives of this thesis.

2. Methods

This chapter partially relates to methodological approaches described in chapters 3 to 5 as part of the publications. Some methods are not described there, since they do not directly relate to the results. Generally, the methods are described here in more detail than in the methodology parts of the other chapters.

3. Climatic and geochemical implications of Archean pedogenic gypsum in the Moodies Group (~3.2 Ga), Barberton Greenstone Belt, South Africa

This chapter was published as:

Nabhan, S., Luber, T., Scheffler, F., Heubeck C., (2016). Climatic and geochemical implications of Archean pedogenic gypsum of the Moodies Group (~3.2 Ga), Barberton Greenstone Belt, South Africa. Precambrian Research, v. 275, p. 119-134.
http://dx.doi.org/10.1016/j.precamres.2016.01.011.

It describes morphology, occurrence and formation mechanisms of pedogenic former sulfate (now silicified) concretions imbedded in numerous Aridisols which build part of a fluvial-braidplain sandstone of the Moodies Group in the Barberton Greenstone Belt, South Africa. The structure and stratification of the paleosol beds and the occurrence of pedogenic gypsum and calcite allowed to draw conclusions about the Archean climate, atmosphere and hydrosphere.

The first author, Sami Nabhan, performed the field work on which the study is based with the help of Christoph Heubeck and Tim Luber, who mapped the Stolzburg Syncline, which shows the most distinctive and best preserved paleosol beds. The original manuscript was written by Sami Nabhan; Christoph Heubeck reviewed and discussed its content. Franziska Scheffler helped to perform the cathodoluminescence measurements at the University of Potsdam.

4. Biogenic overgrowth on detrital pyrite in ca. 3.2 Ga old Archean paleosols

This chapter was accepted and will appear in the September 2016 issue of *Geology* as:

Nabhan, S., Wiedenbeck, M., Milke, R. and Heubeck, C., (2016). Biogenic overgrowth on detrital pyrite in ca. 3.2 Ga old Archean paleosols. Geology, v. 44; no. 9; p. 763-766.
http://dx.doi.org/10.1130/G38090.1

It documents the biogenic nature of pyrite rims overgrowing detrital pyrite grains in fluvial-braidplain-facies sandstone of the Moodies Group in the Barberton Greenstone Belt, South Africa. Their texture, trace element pattern and light $\delta^{34}S_{VCDT}$ values show that pyrite growth occurred in the unconsolidated sediment in the vadose zone due to the activity of sulfate-reducing microbes, related to the reduction of nearby pedogenic sulfate nodules (now silicified). Thus, it not only documents one of the oldest paleosols but also shows that microorganisms accelerated weathering reactions, thus contributing to weathering intensity and partially offsetting the need of elevated temperatures and a CO_2-rich atmosphere. Data indicate that life on land already existed within paleosols ~3.2 Ga ago and that the S-isotopic fractionation at this time was already comparable to that in modern environments in the presence of sufficient sulfate.

The analytical work for this chapter was performed by the first author (Sami Nabhan) who was guided and assisted by Michael Wiedenbeck to carry out the necessary measurements for the S-isotopic composition of the pyrites at the SIMS facility of the Helmholtz-Zentrum Potsdam. Michael Wiedenbeck also contributed to write the methodology section and by correcting the manuscript. Ralf Milke helped to develop the setups for the EPMA measurements and discussed the data. Christoph Heubeck advised the first author and discussed and helped to write the manuscript.

5. The Moodies nodules, a ~3.22 Ga old Earth analog for the Martian Sheepbed nodules

This chapter compares the Archean nodules found in the ~3.22 Ga old lower Moodies Group, Barberton Greenstone Belt, South Africa, to the similarly old Sheepbed nodules of the Sheepbed Member of the Yellowknife Bay Formation of Gale crater on Mars. Both resulted from early diagenetic processes and show strong morphological similarities. This match implies the suitability of the Moodies nodules as Earth analog for the Sheepbed nodules and allows a reevaluation of the formation processes that led to the emergence of the hollow Sheepbed nodules.

The chapter was written by Sami Nabhan, discussed with Christoph Heubeck and Ralf Jaumann and reviewed by both.

6. Summary and Conclusions

This chapter summarizes the findings of the thesis and provides a collective perspective on the implications of this work.

Table of content

List of figures and tables

1. Introduction

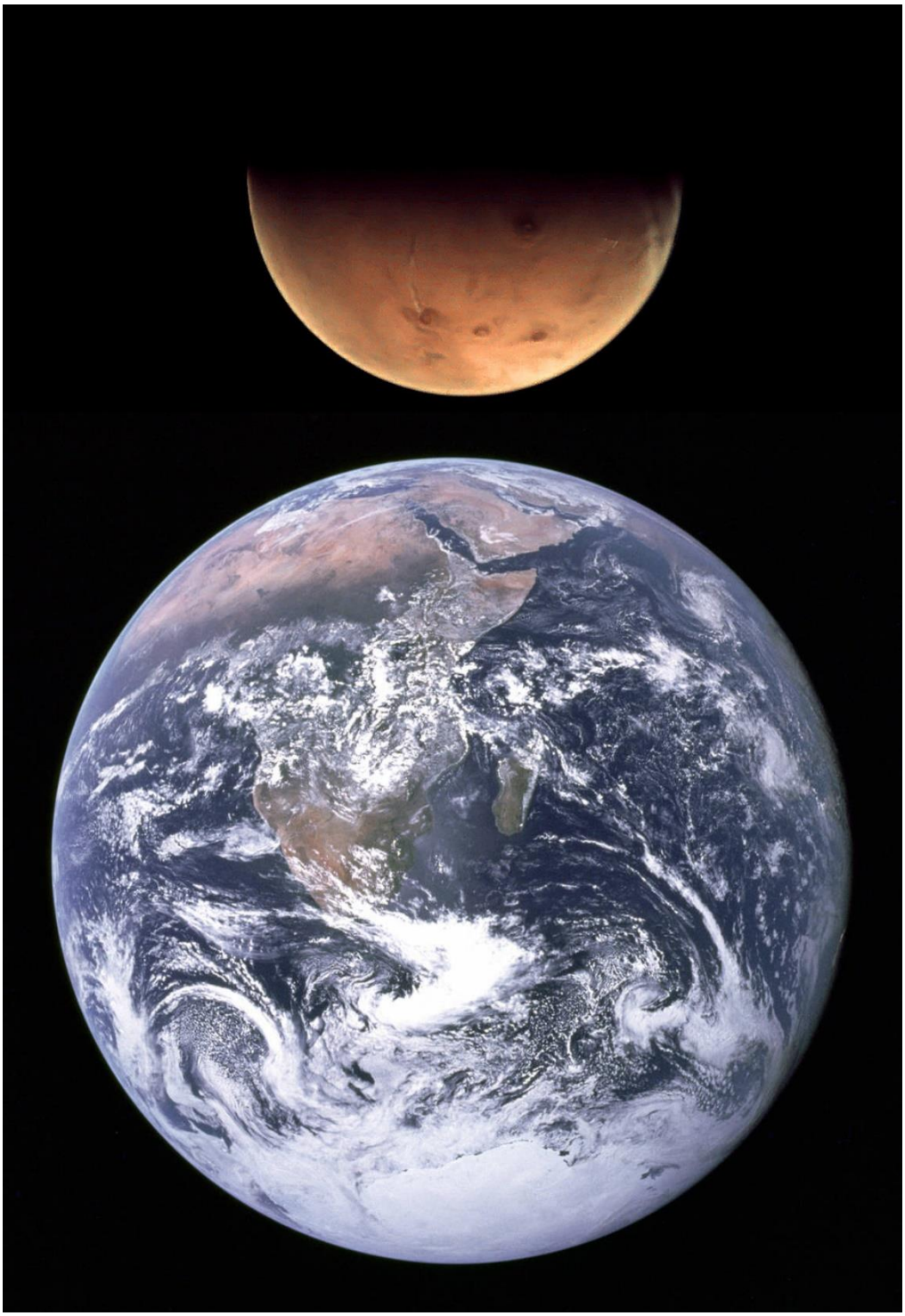

Title Figure: Mars and Earth from Space. Top: Mars as seen by Mars Express on 15. December 2012 from an altitude on 9761 km. Image: ESA, Id: 309371. Below: Earth as seen by the Apollo 17 crew on 7. December 1972. Image: NASA.

During the last decades, several orbiters and landers where able to collect data and information about the surface of Mars, thereby increasing our knowledge about the planet. In the seventies of the last century, the two combined orbiter-landing missions Viking 1 and Viking 2 successfully reached its orbit and landed on Mars (Fig. 1.1). The orbiters delivered a large set of color and stereo images that gave new insights to the understanding of Martian surface processes. The orbiters mapped 97% of the Martian surface with a higher resolution than previous images provided (150 - 300 m, and 8 m for selected areas). The landers gave insights into the Martian atmospheric and soil composition at the landing sites. Weather and climatic conditions have been observed over the duration of the mission (about 6 Earth years; Flinn, 1977). After Viking, the first successful landing mission was Mars Pathfinder in 1997 that involved a robotic rover named Sojourner (Fig. 1.1). Besides the scientific outcome of the mission like new images taken by a stereoscopic camera system and rock analyses using an alpha particle X-ray spectrometer (APXS; Golombek et al., 1997) a major mission goal was to test technical and engineers possibilities and to prove that a relatively cheap (total costs of $280 million) landing mission on Mars was possible. The next step in exploring Mars was made by the European Space Agency (ESA) by launching the Mars Express mission in 2003, a coupled orbiting and landing mission (Fig. 1.1). While the orbiter is still working and provides high resolution images of infrared and visible spectra of Mars surface, the lander failed to fully deploy after landing (Chicarro et al., 2004). The two Mars Exploration Rovers (MER) Opportunity (MER-1) and Spirit (MER-2) launched June 2003 and landed January 2004 shortly after the ESA Mars Express mission (Fig. 1.1.). Both rovers worked far longer than the initially planned 90 days of mission duration; Opportunity is still operating. They could show that aqueous weathering took place on the investigated rocks and in soils, indicated by minerals such as hematite, goethite, carbonates and sulfates. These suggest a higher former water abundance (Christensen et al., 2004; Clark et al., 2005; Grotzinger et al., 2005; McLennan et al., 2005; Squyres et al., 2008; Morris et al., 2010). Nodules formed of hematite and hydrated sulfates are imbedded in sedimentary rocks showing structures as ripples and cross-stratification that indicate water transport during their deposition in an aqueous environment (Klingelhöfer et al., 2004; McLennan et al., 2005).

The most recent Mars mission is the Mars Science Laboratory (MSL) with the Mars rover Curiosity which explores Gale crater, a Martian impact crater with ~154 km diameter and a central peak that rises up to 5.5 km above the crater ground (Fig. 1.1; Wray, 2013). Within the crater, the rover detected and documented sedimentary rocks of alluvial, fluvial and lacustrine origin and early-

diagenetic nodules within sedimentary strata (Grotzinger et al., 2014; McLennan et al., 2014; Stack et al., 2014). Both the sedimentary structures and early diagenetic features of those rocks imply the former existence of a habitable environment in the crater (Grotzinger et al., 2014).

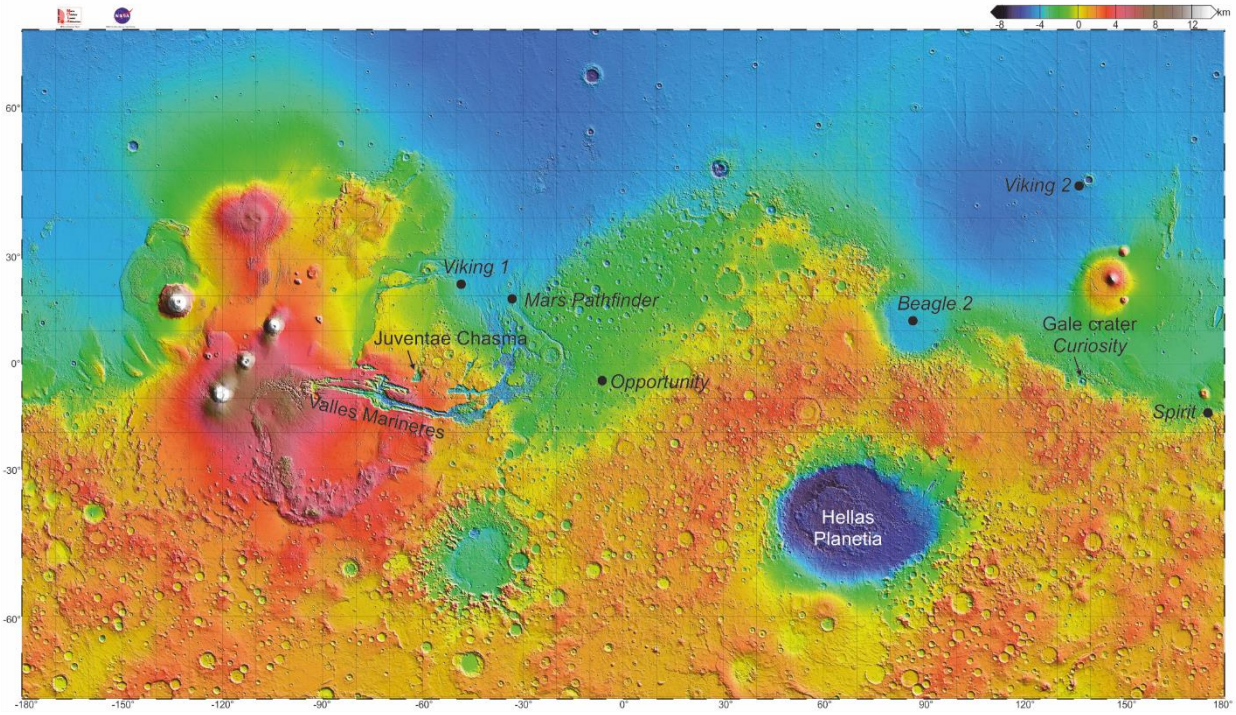

Figure 1.1: Topographic map of Mars generated by Mars Orbiter Laser Altimeter (MARS). The landing sides of selected Mars missions are labeled in italic.

A major target of all missions to Mars is to find habitable environments to demonstrate conclusively if life could have ever existed on the planet. To-date, the findings and outcomes of all previous missions could not confirm that life exists or ever existed on the planet; however, it showed step by step that Mars once indeed had habitable environments. Furthermore, mission results show that these habitable environments had been similar to Archean environments on Earth, arguably the time when life arose on our planet. Therefore, a comparison of Archean environments to those found on Mars contributes to a better understanding for the requirements of life's origin. Since evaporites are a reliable evidence for the former existence of liquid water, constitute an important base for habitable environments, and reflect the chemistry of aqueous and of atmospheric conditions at the time of their formation, investigation of such rocks and minerals of Archean age and on Mars will advance our understanding of similarities and differences of both planets in their youths.

A major question that remains to be answered is why sulfates are abundant in the Late Noachian and Hesperian rock record of Mars, apparently reflecting an environment that had many similarities to the Archean Earth that does not show such abundant sulfate deposits. Whether the lack of basin-wide sulfate deposits in the Archean rock record is caused by their low preservation potential, by the high surface dynamics of Earth compared to Mars or by the lack of sufficient dissolved sulfate in the Archean ocean water is also questionable. However, there are few well-preserved Archean sulfates which can be examined and compared to the findings on Mars to judge the degree of similarity in environmental conditions during their formation.

1.1. Geological timescales on Earth and Mars

Earth's geological timescale is subdivided into 4 eons which are, from oldest to youngest, the Hadean, the Archean, the Proterozoic and the Phanerozoic. The Archean eon starts at ~4 Ga and ends at ~2.5 Ga (Fig. 1.2) with the beginning of the Great Oxygenation Event (GOE). The Archean is characterized by the development of the first stable continental blocks and the emergence of life on the shelves, coastal regions, and possibly even near-coastal terrestrial habitats (Eriksson et al., 2004). The faint young Sun and a closer Moon affected Earth's surface, causing the surface systems to behave very different from todays. The very low atmospheric and oceanic levels of oxygen caused a reducing environment and the absence of an effective UV-shield (Eriksson et al., 2004). These, in turn, affect the formation conditions, settings and chemistry of evaporites.

Two geologic timescales exist for Mars. They are either based on crater counting or on the formation of specific minerals at specific times. Based on crater counting, the middle and late Noachian and the Hesperian (~4.0 Ga to ~3.0 Ga; Fig. 1.2) roughly equal the Earth's Archean eon (Tanaka, 1986; Hartmann and Neukum, 2001). Both eons have seen times of extensive volcanic, tectonic and fluvial activity, processes that affected the Martian surface and led to the conclusion that the surface activity on early Mars was much higher than today (Scott and Tanaka, 1986; Greeley and Guest, 1987; Head et al., 2001). Alternatively, based on mineralogical mappings of Mars, its geological history can also be subdivided into an early stage of extensive clay formation (the phyllosian) followed by a time dominated by sulfate formation (the theiikian) and finally by the siderikian, dominated by the formation of anhydrous ferric oxides (Bibring et al., 2006). Estimates on the beginning and ending of these stages are imprecise, but the late phyllosian and the theiikian occupy most of the time that correspond to the Archean on Earth (Fig. 1.2).

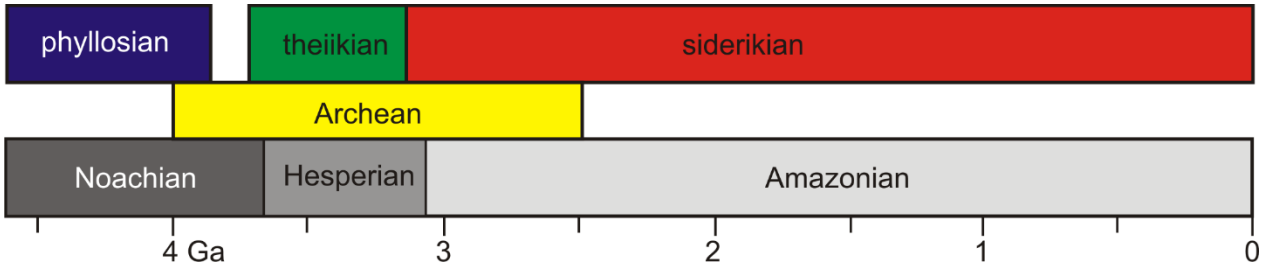

Figure 1.2: Geological timescales of Mars. The upper scale relates to mineralogical mapping of the Mars surface (Bibring et al., 2006) while the lower scale is related to crater counting (Tanaka, 1986; Hartmann and Neukum, 2001). For comparison note the yellow field in-between, showing the approximate duration of the Archean Eon.

1.2. Archean Evaporites on Earth

1.2.1. Definition

Evaporites are chemical sediments and sedimentary rocks that form as result of an increasing concentration of ions in water as precipitates either at the surface or at the base of the water body. The majority of evaporitic sediments and sedimentary rocks on Earth consist of carbonates, sulfates, or halides. Archean evaporites are, to their largest part, either of a restricted-marine facies or hydrothermally related. Open-marine evaporites are completely absent, terrestrial evaporites nearly so.

1.2.2. Overview

Evaporites compose a disproportionally small percentage of the Archean rock record because their preservation potential is generally low and because conditions for their formation may have been poor due to small and few continents, lower continental freeboard, a perceived hot and humid climate, and an unknown saturation state of the oceans. Ocean salinity and surface water temperature are major controlling factors for the precipitation of evaporites. Estimates of the Archean ocean temperature based on oxygen isotope composition of early diagenetic chert units are debated, as is the salinity of Archean ocean water. Archean ocean temperatures, as indicated by the isotope composition of Archean cherts were approx. 55-85°C (Knauth, 2005). Estimates of Archean ocean water salinity based on “adding back” the volume of halite in the geological record would result in a salinity of 1.2 – 2 times the modern value (Knauth, 2005). This number, however, is highly dependent on estimates of the size of subsurface salt deposits and of hypersaline brines in

sedimentary basins. Other factors controlling evaporation include the ionic composition of Archean ocean water and its pH value. The suggestion of an early ocean saturated in sodium carbonate (the "soda ocean") would result in a pH of ~10 (Kempe and Degens, 1985; Gargaud et al., 2005). The presence of reduced iron (Fe^{2+}) in the Archean ocean, however, indicates a pH <6 (Gargaud et al., 2005).

Archean evaporites are commonly preserved as pseudomorphs and silicified from their precursors (gypsum, nahcolite and aragonite). The majority of evaporites are preserved as dolostones and limestone that originally precipitated as carbonate cements such as aragonite and magnesian calcite (Grotzinger and Kasting, 1993) or as stromatolites, a common components of Archean carbonate platforms (Grotzinger and Knoll, 1999). Most carbonates older than ~3 Ga are of peritidal sedimentary facies and found in the greenstone belts of South Africa, Australia and India (Harnmeijer, 2010). The oldest known carbonate platform is the ~2.9 Ga old Steep Rock platform in Ontario, Canada. At about 2.6 Ga, platform-type carbonates became established (Grotzinger and Kasting, 1993; Harnmeijer, 2010), substantially composed of original aragonite (now mainly dolomitized) and exemplified by the ~2.55 Ga old Campbellrand-Malmani carbonate platform with individual beds of up to 65% encrusting carbonate. This suggests that seawater was supersaturated with respect to aragonite and calcite and that its pH was neutral to slightly alkaline (Sumner and Grotzinger, 2004). In some parts of the Archean carbonate platforms, the presence of pseudomorphs of carbonates and chert after halite crystals combined with an absence of sulfate pseudomorphs within supratidal lithofacies zones (Boulter and Glover, 1986; Sumner and Grotzinger, 2004; Eriksson et al., 2005; Gandin et al., 2005) has been interpreted to either reflect a generally low sulfate content or a low calcium content of seawater, a consequence of extensive carbonate precipitation (Boulter and Glover, 1986; Grotzinger and Kasting, 1993; Sumner and Grotzinger, 2004; Eriksson et al., 2005). On the other hand, pseudomorphs after swallowtail gypsum and enterolithic gypsum have been described by Gandin et al. (2005). Some of the crystal fans interpreted as aragonite fans resemble gypsum domes in their structure (Hardie, 2003; Gandin et al., 2005). Calcitization of the former sulfate evaporites is interpreted as result of bacterial sulfate reduction and the organic diagenesis of pyrite (Gandin et al., 2005). Such a metabolic process would constitute a second link to widespread microbial life in the Archean, aside from the abundant morphological evidence provided by stromatolites in these carbonate platforms.

Sulfate deposits formed as thinly bedded barite of early and mid-Archean age are well represented in the ~3.3-Ga-old Sargur Group, Dharwar Craton, central India (Jewell, 2000); the ~3.45-Ga-old

Onverwacht and the ~3.24-Ga-old Fig Tree Groups of the Barberton Greenstone Belt, South Africa (Lowe and Fischer-Worrell, 1999), and in the 3.45-Ga-old North Pole chert-barite unit of the Warrawoona Group, Western Australia (Jewell, 2000). All of them are of marine origin and show primary sedimentary and partly diagenetic structures (Buick and Dunlop, 1990; Jewell, 2000). For some deposits, their possible origin by volcanic-hydrothermal exhalation is discussed (Reimer, 1980). Parts of the North Pole barite have been interpreted as pseudomorphosed gypsum, based on interfacial angles of individual crystals (Buick and Dunlop, 1990; Jewell, 2000; Shen et al., 2001). Sulfur isotope variations within these sulfates in microcrystalline pyrite suggest the existence of sulfate-reducing bacteria (Shen et al., 2001; Shen and Buick, 2004).

Overall, the presence of evaporitic sulfates in the 3.5-3.2 Ga Archean rock record may indicate a global sulfate-bearing, partly oxidized, and stratified ocean (Huston and Logan, 2004). Aside from the deposits mentioned above, only two additional bedded sulfate deposits are known in the geologic record prior to the GOE at ~2.4 Ga, after which they become more abundant (Huston and Logan, 2004), possibly due to low concentrations of sulfate in the Archean ocean (Boulter and Glover, 1986; Grotzinger and Kasting, 1993; Sumner and Grotzinger, 2004; Eriksson et al., 2005; Gargaud et al., 2005). However, a partly oxidized ocean may not be required to produce low seawater sulfate from volcanic SO_2 because SO_2 reacts with H_2O to H_2S and H_2SO_4 even in the absence of oxygen (Huston and Logan, 2004; Gargaud et al., 2005).

Terrigenous evaporites are exceedingly rare in the Archean. Nabhan et al. (2016a) describe widespread silicified former sulfate concretions from the vadose zone of a fluvial to supratidal facies of the ~3.2-Ga-old Moodies Group, South Africa and interpreted them to have formed during early diagenesis by evaporating groundwater in a semiarid or arid coastal plain.

Some Archean cherts and possibly banded-iron formations (BIF) can be considered evaporites where the involvement of biologic processes is uncertain or unlikely. Some chert may form abiogenically in subtidal environments due to silica oversaturation of pore waters during evaporation (Pufahl and Hiatt, 2012). Banded-iron formations are composed of a mixture of silica with iron-bearing minerals such as hematite, magnetite, siderite and pyrite which precipitate depending on ocean water chemistry (Huston and Logan, 2004; Gargaud et al., 2005; Pufahl and Hiatt, 2012). They are interpreted either as deepwater precipitates or as precipitates developed during times of restricted clastic supply.

1.2.3. Basic Methodology and Applications

The base for evaluating, characterizing and classifying Archean evaporites are field observations such as mapping, documentation of sedimentary structures and the construction of stratigraphic columns and cross sections. Further investigation uses analytical approaches such as thin-section microscopy, electron probe micro-analysis (EPMA) and secondary electron microscopy (SEM) for major and trace element distribution, Raman spectroscopy for the examination of solid, fluid and gas inclusions and mass-spectroscopy to study the fractionation of stable isotopes of elements such as S, C, O, N and Fe.

Because evaporites reflect atmospheric and hydrospheric conditions during the time of their formation, they can be used to constrain Archean atmospheric and seawater composition. Terrestrial evaporites can also be used to provide information on Archean groundwater and to infer climatic conditions. In addition, evaporites are often related to or aided by biogenic processes and may thus preserve traces of early life; this is the case on Earth, and may also apply to Mars.

1.3. Archean-equivalent Evaporites on Mars

Layered sulfate deposits are abundant on Mars and have mainly been found in the Valles Marineris Valley network and in adjacent basins (Bibring et al., 2006; Carr and Head, 2010). One of the best explored Martian basins hosting such layered sulfate deposits is the Juventae Chasma north of the Valles Marineris system (Fig. 1.1). It contains four, up to 3 km thick, ~3.3 Ga old, internally layered mounds (A, B, C, and D; Catling et al., 2006; Neukum et al., 2009) mainly composed of mono- and polyhydrated Mg-, Fe- and Ca-rich sulfates (Gendrin, et al. 2005; Bibring et al., 2006; Bishop et al., 2009; Noel et al., 2015). Based on shape and composition of the mounds multiple formation hypotheses have been offered: (1) glacial, lacustrine or aeolian processes (Malin and Edgett, 2000), (2) sub-ice volcanism (Chapman et al., 2003), (3) evaporation (Montgomery and Gillespie, 2005) and (4) spring deposit events (Rossi et al. 2008). All of these processes require the presence of sulfur acidic water under at least slightly oxidizing conditions, for which two sources are currently in discussion: Volcanic exhalation (Johnson et al., 2008; Halevy and Head, 2014) and aqueous pyrite oxidation (Burns and Fischer, 1993; King and McSween, 2005). Based on evaporation models of sulfate solutions produced trough leaching of Mars analog ultramafic rocks, a paleolacustrine history for the Juventae basin could be developed which explains the deposition

and structure of the mounds and shows that evaporation from a large water body is the most plausible formation process for these immense mounds (Al-Samir, 2016).

Aside from the layered sulfate deposits, a number of less distinct evaporites and evaporative features have been found on Mars. In the northern polar region of Mars, sulfates, particularly gypsum, are present in the Circum-Polar Dune Field (Masse et al., 2010). Sulfate-rich sediments and soils found by Opportunity and Curiosity are interpreted to be mainly of diagenetic origin (Clark et al, 2005; Grotzinger et al., 2014; McLennan et al., 2005; McLennan et al., 2014; Nachon et al., 2014; Stack et al., 2014). In the Sheepbed Member of Yellowknife Bay in Gale crater, morphologically diverse early diagenetic nodules are present in large numbers. Late diagenetic gypsum veins interact with these nodules (Grotzinger et al., 2014; McLennan et al., 2014; Stack et al., 2014).

1.4. Scientific questions and problems

Earth is, unlike Mars, a planet with a very active and effective surface recycling system. Therefore, the Archean rock record is limited to few areas mainly in Australia, Brazil, Canada, India, and South Africa of which the majority often shows poor outcrop conditions, a high metamorphic overprint, or both. Sedimentary rocks constitute only a small part of this record. Worldwide, the best preserved Archean (meta-)sedimentary successions are located in the Australian Pilbara and in the southern African Kaapvaal Craton. Both contain a variety of chemical sediments including Banded-iron formations (BIF), sedimentary barite, chert and former (now silicified) carbonates. Biogenic processes commonly contributed in variable intensity to their formation; in part, they may outweigh the contribution by evaporation. The oldest-known basin-wide evaporitic deposits on Earth comparable to those of the Valles Marineris system or Juventae Chasma are from the ~1.6 Ga old Mesoproterozoic McArthur Group of northern Australia (Walker et al., 1977; Kendell, 1992). This comparatively young age is because the Archean was most likely a time with very low oceanic sulfate (Boulter and Glover, 1986; Grotzinger and Kasting, 1993; Sumner and Grotzinger, 2004; Eriksson et al., 2005; Ueno, 2014) and very low atmospheric oxygen levels (Eriksson et al., 2004; Canfield, 2005). Therefore, sulfate deposits are exceedingly rare in the Archean rock record. A necessary and obvious first step to compare the abundant sulfatic (but poorly accessible) Martian evaporites to the (rare but accessible) Archean evaporites on Earth is to find the latter.

Sedimentary, bedded barite form part of 3.3 - 3.5 Ga old Archean rock record in Australia, India and South Africa (Lowe and Fischer-Worrell, 1999; Jewell, 2000). Their morphological appearance (layered, bedded) and possible origin by volcanic-hydrothermal exhalation (Reimer, 1980) is comparable with the Martian layered sulfates. Why is gypsum not a main constituent of either deposit type, as it is in most post Archean evaporitic sequences? The answer depends on whether the evaporitic formation of gypsum was possible during the Archean, how such deposits would look like and in which environment they would have formed.

To answer this questions, we went to the Barberton Greenstone Belt (BGB) in South Africa. The ~3.22 Ga old Moodies Group of the BGB in South Africa and Swaziland, one of the oldest and probably the best preserved Archean siliciclastic systems, is composed of strata reflecting terrestrial to shallow-marine environments including alluvial, fluvial, deltaic and tidal settings (Anhaeusser, 1976; Eriksson, 1977, 1978, 1979, 1980; Heubeck and Lowe, 1994a, 1994b, 1999; Eriksson and Simpson, 2000; Eriksson et al. 2006; Simpson et al., 2012; Heubeck et al., 2013; Heubeck et al., 2016). In the northern part of the BGB nodules of possible sulfatic origin have been found in the Stolzburg, the Dycedale and the Eureka Synclines at several stratigraphic levels of the Moodies Group.

The origin and formation processes of the nodules is addressed in chapter 3 with a focus on the geochemical and climatic implications of this findings. The nodules will be introduced as pedogenic, now silicified former gypsum nodules which are found to be abundant to rock forming in a number of Archean paleosols that are part of fluvial to supratidal sedimentary rocks mostly but not exclusively of the lower Moodies Group (unit MdQ1; Anhaeusser, 1976).

The biogenic contribution to the pedogenic processes under which the nodules in the Moodies Group formed is addressed in chapter 4. They formed in close spatial and temporal relation to the formation of authigenic pyrite. Our results suggest the activity of sulfur-processing microbes, indicated by the S-isotopic composition of the authigenic pyrite.

Chapter 5 compares the implications of the terrestrial Archean findings described and discussed above to those made on Mars (Grotzinger et al., 2014; McLennan et al., 2014; Nachon et al., 2014; Stack et al., 2014). In particular, nodules of the Sheepbed Member of the Yellowknife Bay Formation in Gale crater are morphologically strikingly similar to the Archean Moodies nodules on Earth. They can therefore possibly be used as an analog to constrain the formation of the Sheepbed nodules.

Chapter 6 summarizes the findings in this thesis, explaining how the Archean rock record and especially the Moodies Group paleosols constrains former habitable environments on Mars.

2. Methods

Title Figure: Methods and instruments. Collecting samples and field data (upper left) for EPMA (upper right) at the mineralogy department, FU Berlin and SIMS (below) at the GFZ (GeoForschungZentrum).

Data collection began with field observations, mapping and recording of stratigraphic sections from Moodies Group strata at selected locations in of the Barberton Greenstone Belt. Collected samples from such investigated areas were shipped to Berlin, Germany and processed in laboratories of the Freie Universität Berlin, the University of Potsdam, the Westfälische Wilhelms-Universität Münster and the Helmholtz-Zentrum Potsdam. This began with the slabbing and polishing and continued with the production of thin sections to record macro- and micro-structures, respectively. Microstructures were documented using translucent light-, polarized light-, reflected light- and cathodoluminescence microscopy. Secondary electron microscopy (SEM) and electron probe micro-analysis (EPMA) were used to observe microstructures smaller than those visible with standard thin section microscopy and to evaluate the qualitative and quantitative elemental composition of minerals. Finally, bulk sulfur isotope analysis of pyrite was performed using a Stable Isotope Ratio Mass Spectrometer and in situ sulfur isotope analysis of these pyrites were obtained using a secondary ion mass spectrometer.

2.1. Field observations

During two field seasons in August 2012 and August 2013 selected locations of the Barberton Greenstone Belt in northeast South Africa were investigated. The Greenstone Belt is composed of several domains separated by the Inyoka Fault System. The investigated strata are part of the northern domains (north of the IF) and belong mainly to the Moodies Group and subordinately to the uppermost Fig Tree Group (Schoongezicht Fm.). These strata crop out in three tectonic structures: The Stolzburg, Eureka and Dycedale Synclines. Nodule-bearing units were mapped and measured through numerous stratigraphic sections. These sections cover stratigraphic intervals ranging from several tens to hundreds of meters with centimeter-scale resolution documenting lithology, sedimentary structures and facies changes. Sedimentary structures were documented at outcrop-scale to obtain an overview of medium-scale physical and chemical processes. 45 samples from fist- to boulder-size were collected. Sampling localities, the observed sedimentary structures and their alteration state are shown in Appendix A.

2.2. Thin section microscopy and petrography

Standard thin sections of ~30 µm thickness were made from the collected samples for microscopic and petrographic investigations. Two component epoxy resin Araldite 2020 were used to fixate the

samples on glass sample holder. About 80 thin sections were produced by grinding the samples with silicon carbide powder with a granulation down to 1200 what corresponds to a grain size of 3 µm. About 40 of them were polished with polishing paste of 0.5 µm particle size. Polished and grinded thin sections were studied with a Leitz Laborlux 12 polarized-light microscope using translucent-, polarized- and reflected-light microscopy to investigate micro structures, mineralogy and petrography of the sampled rocks. Reflected light microscopy has especially been used to examine opaque minerals and their structures. A combined Pixel-Fox digital camera system was used to take pictures of this features. Sandstones were classified after McBride (1963) by counting 300 points per thin section using a Swift Model F point counter, combined with the microscope.

2.3. Cathodoluminescence (CL) microscopy

CL-microscopy were performed on standard thin sections at the University of Potsdam using a Leica DMRX polarized-light microscope coupled to a Citl cold-cathode-electron source and a Leica DFC300 FX high sensitive color camera for fluorescence applications. An electron beam with a voltage of 20 kV and an amperage of 0.2 µA were used to get the samples into an existed state. While the exited material returns into its normal state it emits light that can be observed with the attached microscope. Differences in the intensity and the wavelength of the emitted light shows heterogeneities of the luminescence reactive minerals either caused by different trace elements and their content within the minerals or by disorders in the crystal lattice. Such heterogeneities can resemble growth zoning or replacement reactions. The CL microscope of the University of Potsdam does not allow spectral analyses of the emitted light but only gives an optical impression and the description of the observed colors. It is therefore highly subjective.

2.4. Secondary Electron Microscopy (SEM)

A Zeiss Supra^{TM} 40 VP Ultra Secondary electron microscope coupled with an Oxford Instruments EDX-system from the paleontology department of the Freie Universität Berlin was used to perform qualitative element analysis of elements heavier than Na. Due to its superior spatial resolution it was also used to take Backscatter electron (BSE) images. Its capability to handle samples of different sizes and shapes allowed not just to use thin sections but also polished slides, rock fragments and separated grains and minerals. All samples need to have either a gold or a carbon coating to achieve a better conductivity and thereby a better resolution for both the EDX and the

backscatter detection system. Depending on the sample characteristics, the needed resolution and the nature of the analysis two different setups have been used with a voltage of 15 or 20 kV.

2.5. Electron Probe micro-analysis (EPMA)

The JEOL JXA 8200 SuperProbe of the mineralogy-petrology department of the Freie Universität Berlin was used to perform qualitative and quantitative element composition analysis of minerals on polished thin sections. Thin sections were coated with carbon for better conductivity. Qualitative analysis of elements heavier than Sodium was performed using the included Energy-dispersive X-ray spectroscope (EDX) while quantitative elemental analysis for elements heavier than Carbon were performed using the 5 available Wavelength-dispersive X-ray spectroscopes (WDX). Two different WDX setups to measure major elemental compositions were created. One to identify and classify sulfates and carbonates, the second one was used for sulfides.

The sulfate/carbonate setup was created to measure the mayor elemental compositions of inclusions hosted in quartz cement. A voltage of 15 kV, a probe current of $2*10^{-8}$ A and a probe diameter of 10 µm was used. The used measurement conditions including a list of the measured elements, used crystals and standards and the peaks with their measured peak and background time are listed in Tab 2.1. The sulfide setup includes mayor and trace element (TE) composition and was mainly used to measure pyrite, with a voltage of 20 kV, a probe current of $1*10^{-7}$ A and a probe diameter of 1 µm. Further details are listed in Tab. 2.2.

Qualitative trace element mappings of Nickel and Cobalt were performed on pyrite, using a voltage of 20 kV and a probe current of $1*10^{-7}$ A. About 120 TE maps for each of the two elements (Ni, Co) were made to show possible zoning of the pyrite grains and the morphology of detrital cores in the zoned minerals.

Table 2.1: EPMA measurement conditions of sulfates and carbonates to determine the mayor elemental composition of inclusions hosted in quartz cement.

Element	Crystal	Peak	Peak time	Back time	Standard
Al	TAP	Ka	10	5	Sanidine
K	PETH	Ka	2	1	Sanidine
S	PETJ	Ka	10	5	Celestite
Na	TAP	Ka	5	2.5	Albite
Fe	LIFH	Ka	10	5	Ilvait
Ca	PETH	Ka	10	5	Wollastonite
Sr	PETJ	La	10	5	Celestite
Mg	TAP	Ka	10	5	Olivin
Ni	LIFH	Ka	10	5	Nickel
Ba	PETH	La	10	5	Barite
Si	PETJ	Ka	10	5	Sanidine

Table 2.2: EPMA measurement conditions for mayor and trace elemental composition of sulfides

Element	Crystal	Peak	Peak time	Back time	Standard
Cu	LIF	Ka	60	30	Chalcopyrite
Ni	LIF	Ka	60	30	Nickel
Co	LIF	Ka	60	30	Cobalt
Fe	LIF	Ka	10	5	Iron
Pb	PETJ	Ma	60	30	Galena
S	PETJ	Ka	10	5	Chalcopyrite
Mo	PETJ	La	60	30	Molybdenum

2.6. Sulfur isotope analysis

Sulfur isotopes were measured on pyrites collected from three different localities within the Moodies and Fig Tree Groups. The collected samples are from different settings and the pyrite within them shows different morphologies. To obtain a better understanding of the formation processes and the provenance of the pyrite, its S-isotope composition was measured using two different analytical methods.

2.6.1. Bulk analysis with ThermoScientific MAT 253

Pyrite grains were separated from three samples (12;003-4, 12;007-1 and 13;012-4) using standard heavy mineral separation procedures to perform bulk multiple S-isotope analysis. After removing weathered crusts with a rock saw the remaining pieces of hand samples were crushed first with a jaw crusher and afterwards with a roller mill. The produced rock powder was sieved and the two grain fractions 100 µm – 200 µm and 200 µm – 280 µm were used for further processing. Heavy mineral separation was performed using heavy liquids, first bromoform with an average density of 2.85 g/cm^3, and afterwards di-iodomethane with an average density of 3.3 g/cm^3. The remaining heavy mineral fraction containing all grains with a density higher than 3.3 g/cm^3, was further treated magnetically with an electromagnetic separator from Frantz using different current strength. The dominance of pyrite in the heavy mineral fraction, its high density and non-magnetic character led finally to a separate almost exclusively composed of pyrite. Other heavy minerals which remained in the sample (e.g. zircon or chromite) were removed by handpicking to produce a clean pyrite separate.

The separated pyrites of all three samples were used to perform bulk multiple S-isotope analysis using the ThermoScientific MAT 253 mass spectrometer of the department of Geology and Paleontology of the Westfälische Wilhelms-Universität Münster. About 15 mg of each sample were powdered and further chemically prepared under a nitrogen atmosphere. The preparation setup consists of a round glass flask and two small glass bottles connected by tubes. The flask stands in a heating mantle and is flooded with nitrogen to get a non-reactive atmosphere. The pyrite sample inside the flask was doused with 10 ml ethanol, 20 ml 25 % hydrochloric acid and 30 ml 1 molar chromium(II)chloride-solution. The generated mixture needed about 2 hours to react while it was heated up to about 85°C and constantly stirred. Any included monosulfide was dissolved by the hydrochloric acid while the disulfidic pyrite was reduced by the chromium(II)chloride solution both released H_2S. The gas runs through the tubes to the first bottle filled with distilled water to clean it. In the second bottle that is filled with zinc acetate solution the H_2S gas reacted to zinc sulfide (ZnS) that precipitated as white flakes. The created solution with the included ZnS was transferred into a beaker and 10 ml of a 0.1 molar silver nitrate solution were added. The silver nitrate reacted with the zinc sulfide to silver sulfide (Ag_2S) that was placed on a filter and dried afterwards.

About 0.2 mg Ag_2S of each sample was used for the measurements. The material was wrapped in alufoil and emplaced in about 30 cm long tubes with 2.54 cm diameter. The closed tubes were flooded with flour gas to transfer the silver sulfide into sulfur hexafluoride (SF_6). This gas finally was introduced into the mass spectrometer after a cleaning procedure using cold traps and measured against a standard gas, the IAEA-S1 standard. ^{34}S the most common S-isotope after ^{32}S was calculated against ^{32}S and the CDT standard and is presented in the δ notation ^{33}S and ^{36}S were also measured and calculated against ^{32}S and ^{34}S and are presented in the Δ notation. The results of this measurements are shown and discussed in Appendix A2.

2.6.2. In situ analysis with secondary ion mass spectrometry

We used the Cameca 1280-HR SIMS instrument at the Helmholtz-Zentrum Potsdam to determine $\delta^{34}S_{VCDT}$ (Vienna Canyon Diablo troilite) compositions at 229 spots on two sample mounts. A single analysis, involving 80s of data acquisition in FC-FC multicollection mode, had a test portion mass of ~300 picograms. The samples were prepared as a thin section made on a 1-inch round glass slide and as a rock slice ~1.5 cm in diameter, embedded in epoxy resin, respectively; each mount included an mm-size piece of the GM3-Ball reference pyrite (Mojzsis et al., 2003), embedded using epoxy into a small well made at the center of each mount. This reference material was assigned a $\delta^{34}S_{VCDT}$ value of 15.1 ‰ (Crowe and Vaughan, 1996). An absolute value of 34S/32S = 0.044163 was used as the zero-point of the $\delta^{34}S_{VCDT}$ scale (Ding et al., 2001). After correcting for small time-dependent instrumental drift, three analytical sessions yielded repeatabilities of ±0.12, ±0.10 and ±0.092 ‰ (1 sd). A careful evaluation of the complete data set indicates that the individual analyses are reliable at a total analytical uncertainty level of better than ±0.7 ‰ (1 sd) in which the dominant sources of error are the reported heterogeneity in the GM3-Ball reference material (Mojzsis et al., 2003) and the assigned uncertainty in the bulk characterization of the Balmat pyrite (Ding et al., 2001).

3. Climatic and geochemical implications of Archean pedogenic gypsum in the Moodies Group (~3.2 Ga), Barberton Greenstone Belt, South Africa

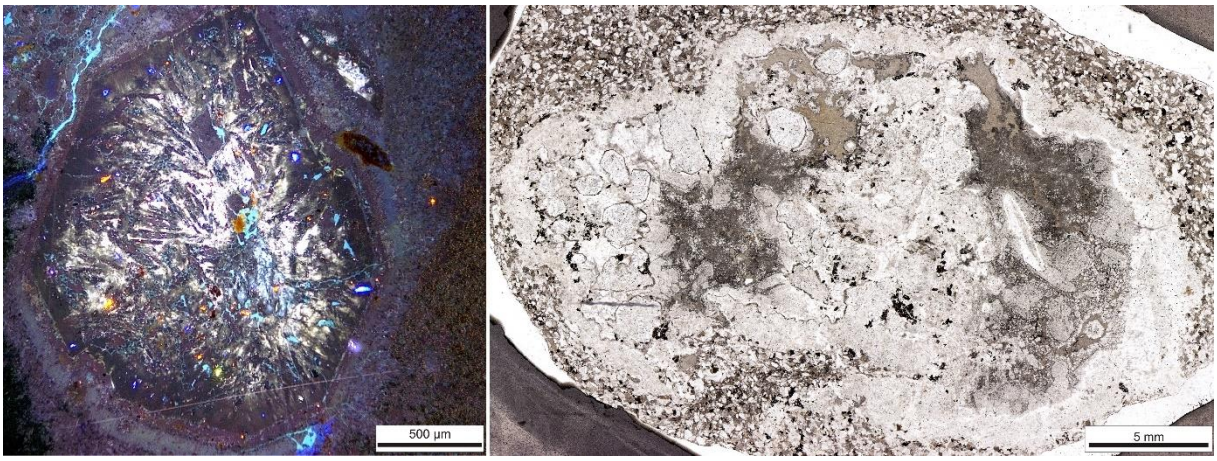

Title Figure: Thin section image of an Archean concretion (right) and detailed CL image of sulfate replacing quartz (left).

This chapter is mainly about:

- Sulfates and carbonates precipitated in Archean fluvial sediments
- Pedogenic gypsum, barite, and calcite that formed concretions in several Aridisol beds
- Rapid concretion formation and the preservation of original structures of the paleosol
- Paleosols that formed under semiarid climate and aggressive weathering conditions
- Moodies concretions that may represent the oldest terrestrial evaporites known to date

Keywords: Barberton Greenstone Belt; Archean; Moodies Group; Evaporites; Sulfate; Paleosol

Kurzfassung

Fluviatile bis supratidale, lithischen Sandsteine der Paläoarchaischen Moodies Gruppe (~3,22 Ga, Barberton Grünstein Gürtel, Südafrika) enthalten mehrere, regional verfolgbare Einheiten mit häufig, teilweise gesteinsbildend auftretenden Konkretionen, bestehend aus megaquartz Pseudomorphosen nach Gips, Baryt und Kalzit. Konkretionen akkumulieren stratiform und sind üblicherweise assoziiert mit aquatisch umgearbeitetem, feinkörnigem, tuffführendem Sediment, ursprünglich rhyodazitischer Zusammensetzung, und können bis zu faustgroße Agglomerate in Krusten Bilden, die sich mehrere zehner Meter lateral erstrecken. Die Verwitterung von Feldspat und tuffhaltigem Sediment lieferte Alkali-Kationen wie Ca, Ba, und K, während Karbonat wahrscheinlich durch silikatische Verwitterung mafischer und ultramafischer Vulkanite, die einer CO_2 reichen Atmosphäre ausgesetzt waren, geliefert wurde. Sulfat wurde teilweise durch Pyrit Lösung geliefert, welche möglicherweise mikrobielle und abiotische Disproportionierung vulkanischen S oder SO_2 beinhaltete. Das Wachstum der Konkretionen geschah offenbar unter pedogenen bis früh-diagenetischen Bedingungen im lockeren, grobsandigen Sediment der Vadosen Zone, dominiert durch saisonale Schwankungen des Grundwasserspiegels unter evaporitischen Bedingungen. Die Konkretionen repräsentieren die wahrscheinlich ältesten, bisher bekannten terrestrischen Evaporite und sind Bestandteil der ältesten, bisher bekannten compound Paläoböden. Ihre Entstehung und Zusammensetzung beschreibt das lokale Auftreten von Sulfat in der Archaischen Atmo- und Hydrosphäre, Ihr Zusammenspiel mit der sich entwickelnden Biosphäre, Archaische Verwitterung, Lokales Klima, Und die Hydrodynamik der Vadosen Zone.

Abstract

Lithic sandstones of braided-fluvial to supratidal facies in the Paleoarchean Moodies Group (~3.22 Ga, Barberton Greenstone Belt, South Africa) include several regionally traceable units with common to abundant, in places rock-forming, nodular concretions of megaquartz pseudomorphs after gypsum, barite and calcite. Concretionary accumulations are stratiform and commonly associated with aqueously reworked, fine-grained, tuffaceous sediment of originally rhyodacitic composition and can grow to fist-sized agglomerates in crusts tens of m in lateral extent. Weathering of tuffaceous material and feldspar delivered alkali cations such as Ca, Ba, and K, while carbonates were likely supplied by silicate weathering of mafic to ultramafic volcanic rocks during exposure to a CO_2–rich atmosphere. Sulfate ions were partly delivered by oxidative pyrite dissolution which may have included microbial and abiotic

disproportionation of volcanic S or SO_2. Concretionary growth apparently took place under pedogenic to early diagenetic conditions within unconsolidated granular sediment in the vadose zone, dominated by seasonal fluctuations of the groundwater level under evaporitic conditions. The concretions likely represent the oldest terrestrial evaporites known to date and form part of the oldest known compound paleosols. Their formation and composition constrain the local occurrence of sulfate in the Archean atmo- and hydrosphere, their interaction with the emerging biosphere, Archean weathering regime, local climate, and vadose-zone hydrodynamics.

3.1. Introduction

Composition and facies associations of numerous Archean units worldwide suggest deposition in terrestrial settings and thus provide a record of Earth's earliest non-marine environments (Grandstaff et al., 1986; Mueller and Dimroth, 1987; Macfarlane et al., 1994; Eriksson et al., 1998; Heubeck and Lowe, 1999; Watanabe et al., 2000; Eriksson et al., 2004; Awramik and Buchheim, 2009). However, surprisingly little is known about the interaction of these sediments with the atmosphere and the emerging biosphere, thereby constraining terrestrial weathering conditions and early diagenetic processes. This is mostly due to the poor preservation potential of such features but certainly also due to the lack of suitable fresh outcrops permitting unambiguous identification of relevant details. A high degree of post-depositional alteration, pervasive deformation and metamorphism, and perhaps also a general lack of awareness of paleo-weathering and early diagenetic features in Archean sedimentary strata complicate the identification and analysis of the relevant rock record.

Here we describe the widespread, mappable occurrence of early diagenetic nodular concretions that formed in unconsolidated sandy sediments in fluvial and coastal settings of the Archean Moodies Group, South Africa (ca. 3.22 Ga; Tegtmeyer and Kröner, 1987; Kröner et al., 1991; Heubeck and Lowe, 1994b; Kamo and Davis, 1994; Heubeck et al., 2013). Although their original composition has largely (but not entirely) been metasomatically replaced by silica, the excellent outcrop conditions and the low degree of penetrative deformation of the Moodies Group allow reconstruction of facies and paleo-hydrological parameters. The objective of this contribution thus is to provide a detailed description of these strata at regional, outcrop, and hand-sample scale as well as a petrographic characterization of the concretions to infer Archean terrestrial weathering and pedogenic processes. Isotopic constraints will be treated in a forthcoming manuscript.

3.2. Geological setting

The Barberton Greenstone Belt (BGB) is located in northeastern South Africa and forms part of the Archean Kaapvaal Craton. Its stratigraphic fill is known as the Barberton Supergroup which is subdivided (from base to top) in the Onverwacht, Fig Tree and Moodies Groups (Fig. 3.1). The lowermost, ca. 8-10 km thick, 3.57-3.30 Ga-old Onverwacht Group is mainly composed of mafic to ultramafic volcanics, such as komatiites and basalts; cherts are subordinate. Its setting is thought to represent an oceanic plateau or a hot-spot volcanic complex (Viljoen and Viljoen, 1969; Anhaeusser, 1976; Lowe, 1994; Lowe and Byerly, 2007; De Wit et al., 2011). The overlying, up to 3 km thick Fig Tree Group is 3.26-3.225 Ga old and consists mainly of epiclastic, volcaniclastic, and chemical sedimentary rocks including thick turbidites, banded-iron formation, chert, some stratiform barite, and felsic to intermediate volcanic and subvolcanic rocks (Heinrichs and Reimer, 1977; Reimer, 1980; Condie, 1997; Lowe et al., 1999; Hofmann, 2005). The uppermost unit in the BGB, the Moodies Group, reaches a thickness of up to 3.7 km and consists mainly of quartz-rich sandstones, polymict conglomerates and argillaceous siltstones deposited in terrestrial to shallow-marine environments including alluvial, fluvial, deltaic and tidal settings (Anhaeusser, 1976; Eriksson, 1977, 1978, 1979, 1980; Heubeck and Lowe, 1994a, 1994b, 1999; Eriksson and Simpson, 2000; Eriksson et al. 2006; Simpson et al., 2012; Heubeck et al., 2013). The greenstone belt is approximately divided axially by the Inyoka Fault into northern and southern domains which show differences in their stratigraphy, lithology, petrographic composition, tectonic history and age at formation level (Heinrichs and Reimer, 1977; De Wit et al., 1992; De Ronde and de Wit, 1994; Heubeck and Lowe, 1994a, 1994b, 1999). Moodies strata generally occupy large synclines separated by tightly folded and faulted anticlinal zones. Most strata dip subvertically. However, undeformed conglomerate clasts, the lack of foliation and mica reorientation on hand sample and thin-section scale as well as the near-absence of shear or strain indicators show that Moodies strata have experienced only minor strain. Strain was significantly higher near major fault zones, the sheared intrusive greenstone belt margin, or in fold hinges (Gay, 1969; Anhaeusser, 1969a; b; Lamb, 1984; Heubeck and Lowe, 1994b). The central part of the BGB has experienced lower-greenschist-facies regional metamorphism while contact metamorphism is important near its margins (Heubeck et al., 2015). Widespread early silicification of Moodies Group rocks strongly reduced mechanical compactability and allowed excellent preservation of original sedimentary textures and structures. Silicification further led to preservation of delicate details such as microbial mats, desiccation cracks, volcanic lapilli, etc.

This study focuses on Moodies strata north of the Inyoka Fault and includes strata exposed in the Stolzburg, Dycedale and the Eureka Synclines (Fig. 3.1). The age of the Moodies Group in this part of the greenstone belt is well constrained by detrital zircons, stratiform tuff beds and several cross-cutting dikes (Zeh et al., 2013; Heubeck et al., 2013). Deposition started between 3225 and 3218 Ma (Tegtmeyer and Kröner, 1987; Kröner and Todt, 1988; Kröner et al., 1991; Heubeck and Lowe, 1994b; Kamo and Davis, 1994; Byerly et al., 1996; Layer et al., 1996; Sanchez-Garrido et al., 2011; Heubeck et al., 2013) and ended prior to 3219±9 Ma, the age of a felsic dike crosscutting the uppermost Moodies Group in the Moodies Hills Block (Heubeck et al., 2013). Thus, Moodies deposition and deformation likely took place in a timespan between approximately 1 and 14 Ma. The stratigraphic record is very highly resolved, with a mean bulk sedimentation rate of about 1 mm/a (Heubeck et al., 2013).

Moodies strata north of the Inyoka Fault were subdivided by Anhaeusser (1976) into several informal lithostratigraphic units at formation level: A basal, 0-100 m thick, polymict conglomerate (MdB; this and following stratigraphic acronyms follow Anhaeusser 1976) was deposited in an alluvial environment. It is overlain by ca. 300-1100 m of slightly gravelly, quartzose and lithic sandstones (MdQ1) of braided fluvial facies. Overlying thick fine-grained sandstones and siltstones (MdS1) are commonly poorly exposed. In places, MdS1 deposits are tuffaceous and include several thin but laterally traceable tuff beds and a jaspilite unit (MdI1). This 400-1000 m thick unit was deposited in coastal and shallow-marine environments including deltaic, tidal and shoreline systems. MdS1 sandstones are overlain by a 50-100 m thick coarse-grained quartzarenite (MdQ2), deposited in a shallow-shelf environment (Eriksson, 1980; Heubeck and Lowe, 1994a). The ca. 2000 m thick section between MdB alluvial conglomerates to MdQ2 quartzarenites represents part of a larger transgressive tract with an overall fining- and thinning-upward trend and significant increase in water depth. It is separated from overlying, up to 1.5 km thick upper Moodies strata by a prominent, 5-50 m thick basaltic lava (MdL). The upper part of the Moodies Group shows complex petrographic and lithologic trends. It is mainly comprised of interbedded sandstone and tuffaceous siltstone (MdS2, MdS3) and includes several jaspilite beds (MdI2, MdI3, MdI4). Main depositional environments were shallow-marine to coastal settings. Deposits are occasionally interbedded with fluvial cross-bedded sandstone and alluvial conglomerate (MdQ3).

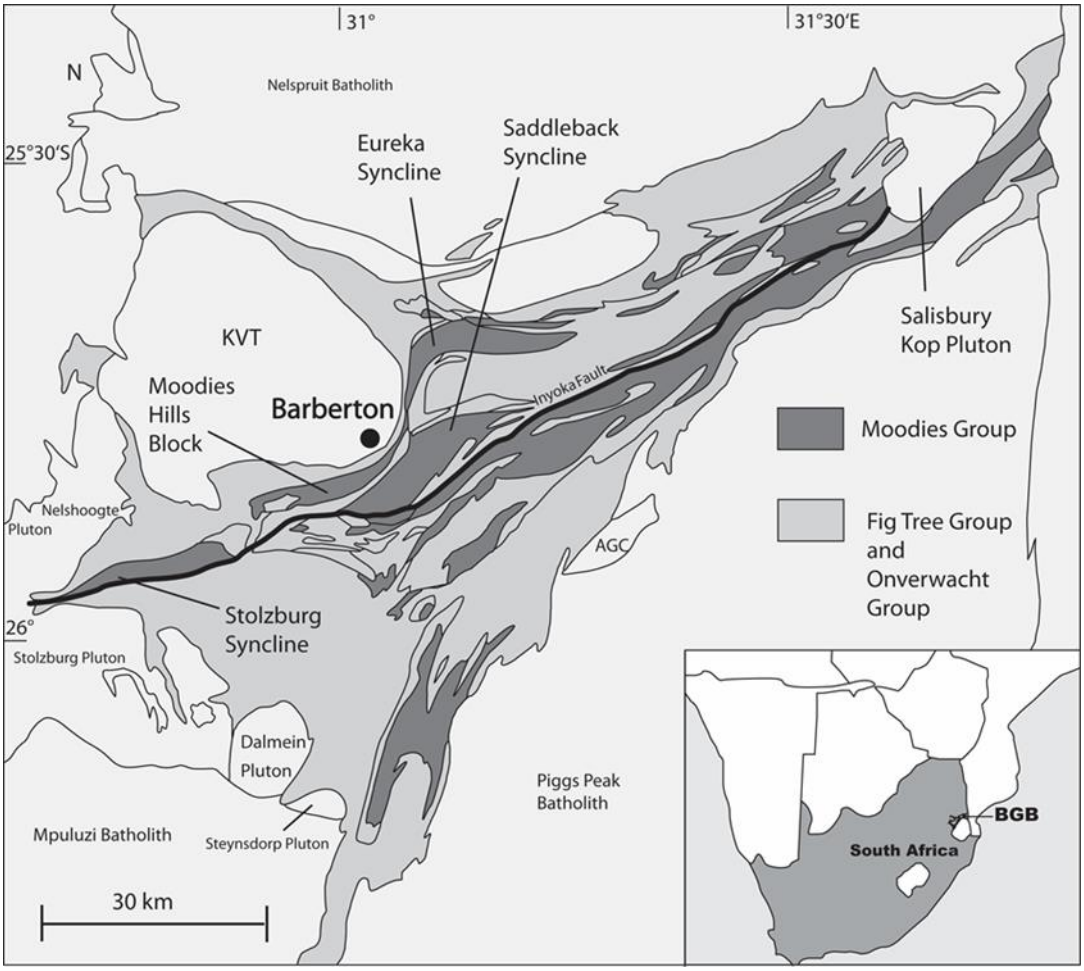

Figure 3.1: Generalized geological map of the Barberton Greenstone Belt (modified after Anhaeusser, 1969).

3.3. Methods

Stratigraphic sections of the Moodies Group were measured at numerous locations in the Stolzburg, Dycedale and Eureka Synclines. Sedimentary structures were recorded at outcrop scale and examined in detail on polished slabs. Standard thin-section and cathodoluminescence microscopy provided the base for petrographic analyses. 300 points were counted per sandstone thin section using a point counter combined with a polarized-light microscope. Sandstones were classified after McBride (1963). The electron microprobe at the Department of Geological Sciences, FU Berlin, was used to evaluate the qualitative and quantitative elemental composition of minerals. The Raman spectroscope at the Department of Geological Sciences, FU Berlin, was subsequently used to further evaluate the precise mineralogy of carbonates and sulfates. The cathodoluminescence (CL) microscope at the Institute of Earth and Environmental Science of the University of Potsdam was used to detect and observe microstructures and textures within concretions.

3.4. Stratigraphy and facies

Moodies strata north of the Inyoka Fault crop out in four large and several smaller synclines. The large synclines are the Stolzburg Syncline (SbS), the Moodies Hills Block (MHB), the Saddleback Syncline (SS) and the Eureka Syncline (ES) (Fig. 3.1). Concretion-bearing units occur throughout all large synclines but also occur in strata of similar or identical facies in the smaller Dycedale Syncline, outlining an area of about 30 km by 30 km.

Although concretion-bearing units occur at several stratigraphic levels within the Moodies Group, they are most common within the braided-fluvial facies of the lower part of MdQ1 sandstones which is best exposed in the eastern Stolzburg Syncline (Fig. 3.2; Appendix B1). There, the lower Moodies Group is composed of heterogeneous, coarse-grained, commonly gravelly and poorly-sorted, massive to cross-bedded litharenites and lithic subarkoses transitionally overlying alluvial conglomerates of the Moodies basal conglomerate (MdB). These conglomerates are poorly developed in the Stolzburg Syncline (Heubeck and Lowe, 1994a and b) so that Moodies gravelly sandstones commonly conformably overlie immature conglomerates of the Schoongezicht Formation. The Schoongezicht Fm. is the uppermost unit of the Fig Tree Group, which fines upwards into feldspathic, fine- to medium-grained litharenites and lithic arkoses. The contact of these two lithostratigraphic units is marked by a distinct increase of quartz content in sandstone. Concretions occur in overlying sandstones of unit MdQ1 which reach approximately 300 m in thickness and are in turn overlain by dominantly medium-grained, cross-bedded, well-sorted, concretion-free sandstones of a sandy shoreline facies. Sandstones of MdQ1 fine upward into turbiditic siltstones of a prodelta facies (Reimer, 1967). This transitional trend is well exposed in each of the examined regional synclines over several km strike length. In the Stolzburg Syncline, the transition from braided fluvial to shoreline facies is marked by an about 20 m thick section of variably reworked rhyodacitic ash-fall tuff interbedded with medium- to coarse-grained sandstone, possibly a lagoonal or estuarine deposit.

Lower MdQ1 sandstones are organized in shallow (up to 1.5 m thick) but wide (a few to tens of meters wide) channels with erosional bases and well-developed, normally graded gravelly to sandy fills (Fig. 3.3). Channel bases commonly consist of granule-bearing sandstone with pebble strings and outsized cobbles up to 12 cm in diameter, and rarely of up to 40 cm thick, laterally discontinuous conglomerates (Fig. 3.3 and 3.4B). Some channels are filled by coarse-grained, massive-appearing sandstone and fine up into cross-bedded, medium-grained sandstone (Fig. 3.4D). In places, tuffaceous fine-sandy to silty beds, rarely interbedded with thin (< 15 cm thick) reworked ash-fall tuffs and shales top the fining-upward sections. Fine-

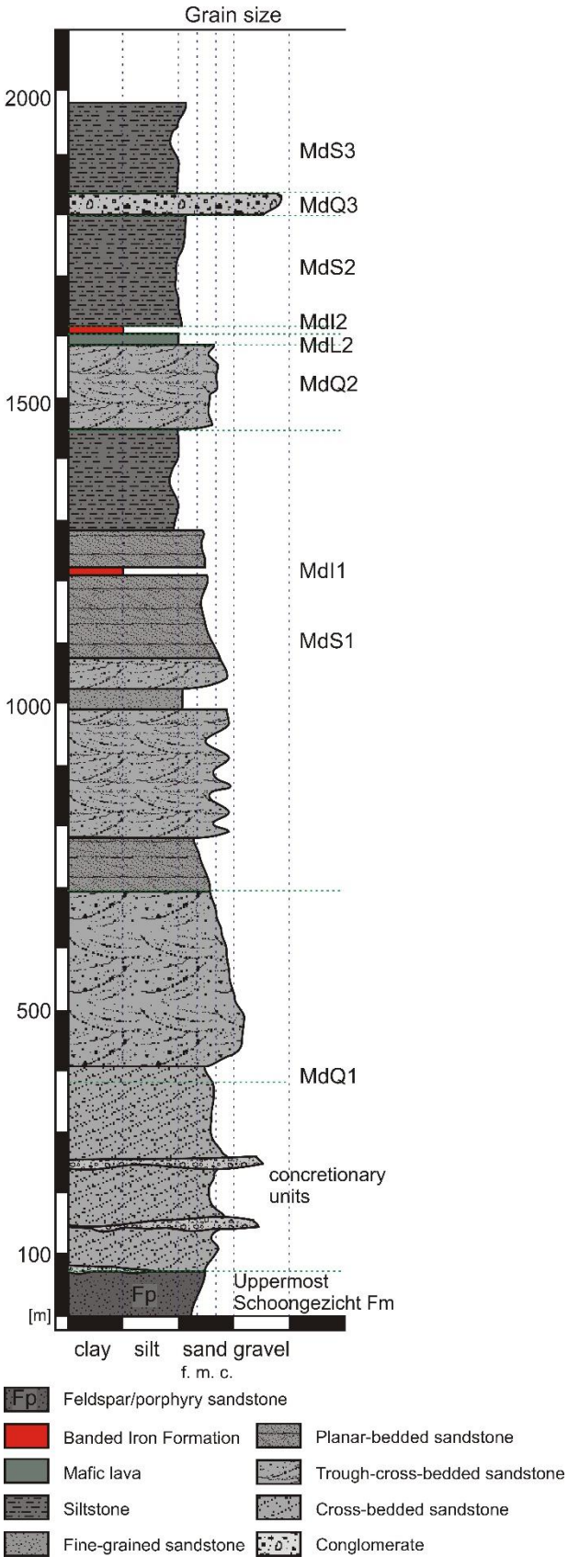

Figure 3.2: Simplified stratigraphic column of the Moodies Group in the Stolzburg Syncline. The lower, braided-fluvial part of unit MdQ1 contains regionally traceable concretion-bearing beds.

grained sandstones are commonly rippled while the rare silty shales are laminated and show desiccation cracks (Fig. 3.4C). Ripples are typically asymmetrical with straight to slightly sinuous crests. Associated tuffs are composed of fine-grained (rhyo-) dacitic volcanic and volcanoclastic material that is largely reworked and therefore shows current structures. Structures include horizontal lamination, wavy lamination or ripples, depending on grain size and paleocurrent strength. We interpret this ca. 300 m thick lower part of unit MdQ1 as a highly erosive braided fluvial system which traversed a floodplain with shallow bodies of standing water.

Concretions in this facies usually occur as common to abundant, in places rock-forming, rounded bodies about 0.5 to 3 cm in diameter which are aligned along bedding planes or foresets. Many show zoning expressed by central cavities due to recent weathering (Fig 4D). Because these concretions are mainly composed of quartz, they weather resistively compared to the surrounding quartz-mica-cemented litharenites and sublitharenites. Beds rich in concretions are therefore readily traceable within major outcrops and on map scale. Concretions cluster or coalesce towards the top of individual coarse- and medium-grained sand beds (Fig. 3.5A-D) and may form approximately 1 cm thin beds interbedded with sandstone of similar thickness in overlying fine-grained and silty

sandstone (Fig. 3.5C). Some concretions cluster in up to 20 cm thick beds, displacing nearly all clastic components (Figs. 3.4D, 3.5A and C). Laterally, these concretionary beds are commonly truncated by the bases of fluvial channels. Medium- to fine-grained concretion-bearing sandstones commonly show mm-thick heavy mineral laminations which are usually deformed around concretions (Figs. 3.5C and D). Rarely, concretions, still showing typical characteristics like zoning, are observed as reworked clasts (Fig. 3.5E). They are concentrated at the channel bases and are commonly somewhat elongated or angular; others show imbrication.

Three fluvial channel types are distinguishable in the braided fluvial MdQ1 strata of the Stolzburg Syncline. Most channels are dominated by cross-bedded or massive, medium-grained to granular sandstones with a basal conglomerate that includes clasts up to 12 cm in diameter. The fining-upward channel fill is usually topped by rippled, fine-grained sandstone but may fine to rippled siltstone or to a mud-drape, commonly with desiccation cracks (Fig. 3.3A). This channel type is devoid of concretions. A second channel type is topped by rippled, fine-grained sandstone or massive medium-grained sandstone, occasionally showing heavy mineral laminae. In this channel type, concretions are common and increase in size and number upwards (Fig. 3.3B). The third channel type, composed of granular sandstone that fine up into medium- to fine-grained sandstone, contains reworked concretions at or close to its base (Fig. 3.3C).

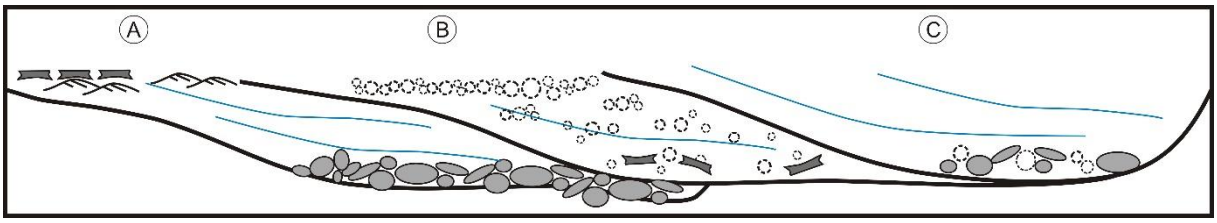

Figure 3.3: Simplified schematic sketch of the three recognized types of fluvial channel-fill facies with respect to concretions. A) Concretion-free fluvial channel with conglomerate at the base, overlain by cross-bedded granule to medium-grained sandstone, rippled fine-grained sandstone to siltstone and topping mudstone with desiccation cracks. B) Concretion-bearing fluvial channel in which concentration and size of concretions increase towards the top, in places coalescing in a concretionary bed. The cross-bedded sandstone at the channel base commonly contains rip-up mud clasts that had been eroded from the underlying channel. C) Fluvial channel transporting concretion clasts near its base.

Redeposited, angular and imbricated concretions which had apparently been transported for somewhat longer distances (Fig. 3.5E) are preserved in prominent outcrops of the Dycedale Syncline where subvertically dipping, medium-grained, cross-bedded, shale-draped sandstone of tidal facies reach about 250 m thickness (Ferrar and Heubeck, 2013). Concretions from the stratigraphically lower, supratidal part of this locality are typically part of granule-bearing sandstone and sandy conglomerate and show similar size (up to 8 mm) and angularity as

epiclasts. In stratigraphically higher, more distal-facies beds, abundant clasts of buff-colored tuffaceous siltstone containing densely packed silicified concretions indicate that nearby concretionary beds had been eroded and reworked in the intertidal zone.

In the Eureka Syncline, abundant molds of radial and clumpy clusters of concretions, replaced by carbonate cement, are concentrated in cross-bedded, occasionally granular, coarse-grained deltaic sandstone. These sandstones are best exposed in the western limb of the syncline where they cap at least two progradational deltaic cycles in unit MdS3 (Anhaeusser, 1966). There, the weathered, Fe-oxide- and -hydroxide-lined molds are somewhat flattened parallel to subvertical bedding and stretched subvertically, consistent with the orientation of the moderate strain observable throughout the Eureka Syncline.

Figure 3.4: Sedimentary structures of the braided-fluvial facies of unit MdQ1 in outcrops of the Stolzburg Syncline. A) Subvertically dipping strata in the eastern part of the syncline. B) Channelized conglomerate showing erosional contact to underlying sandstone (black arrows). Hammer handle points up. C) Rippled fine-grained sandstone showing nearly straight (foreground) and sinuous (background) ripple crests, coated by mudstone. Inset shows desiccation cracks visible in the slab in the background. D) Low-angle cross-bedded, medium- to coarse-grained sandstone overlying a densely packed concretionary bed. Note numerous concretions, hollow due to weathering, near the base.

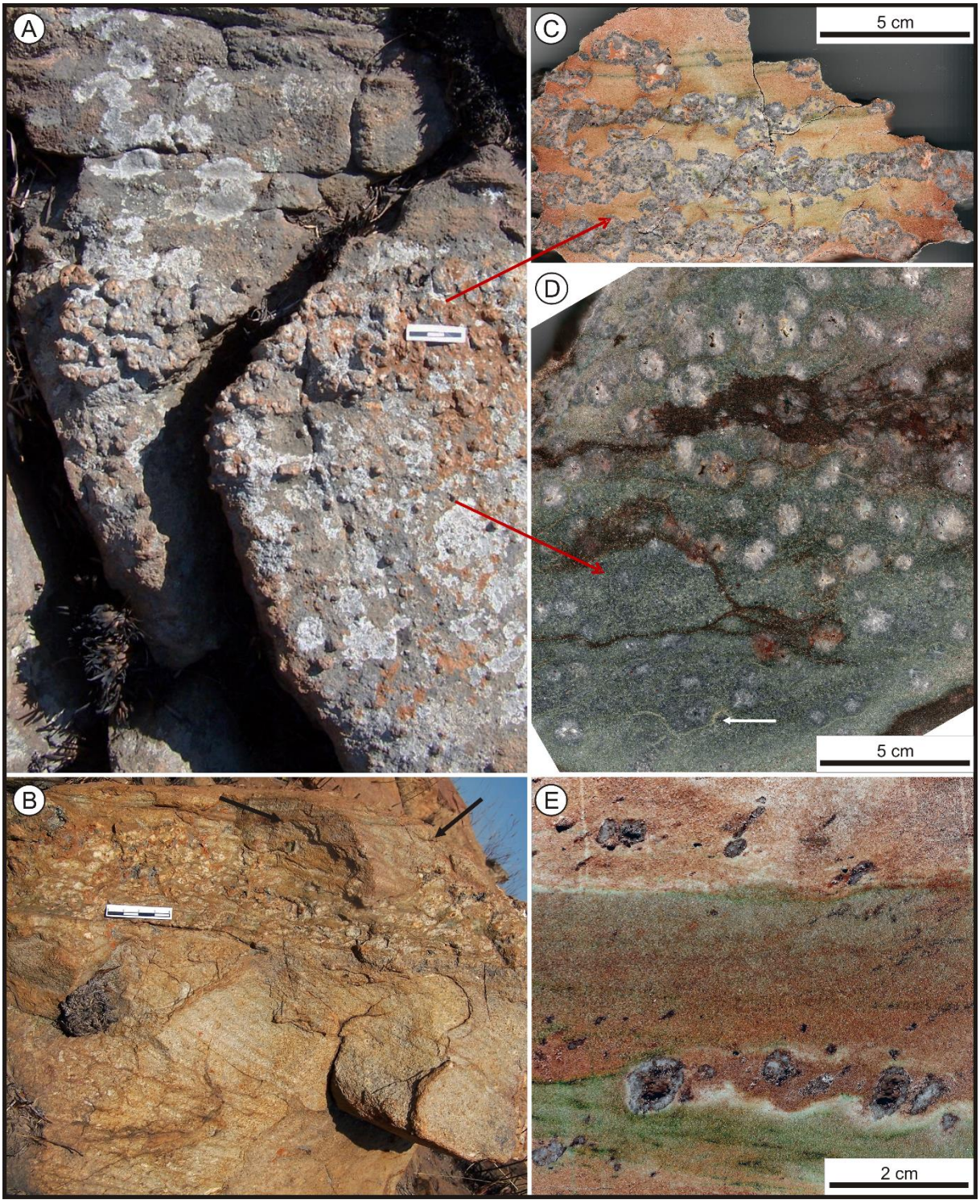

Figure 3.5: Concretion-bearing braided-fluvial sandstones of the Stolzburg and Dycedale Synclines at outcrop and hand-sample scale. A) Upward-fining, concretion-bearing, medium-grained sandstone showing upward increase in number of concretions. This bed is overlain by a concretion-free, thin-bedded, medium-grained sandstone. Scale bar is 3 cm long. B) Concretion-bearing bed (base at scale) overlying cross-bedded sandstone, in turn eroded by shallow, cross-bedded, sand-filled channel (upper right, black arrows), indicating early diagenetic growth of concretions. Scale bar is 4 cm long. C) Polished slab showing interbedding of white, coalesced stratiform concretions with brown fine-grained sandstone. Green lamina near top of the slab are enriched in heavy minerals. D) Polished slab of a medium-grained sandstone showing upward-increasing proportion and size of concretions.

Heavy mineral laminae in this sample are oxidized and weather brownish while unweathered heavy mineral laminae dominated by pyrite (lower left, white arrow) appear yellowish. E) Concretionary granule-sized clasts at the base of a fining-upward sandstone from the Dycedale Syncline erosionally overlie a green shaly sandstone.

3.5. Petrography and micromorphology of concretions

3.5.1 Sandstone petrography

Strata which contain in-situ concretions are largely immature, moderately sorted, lithic, fine- to medium-grained sandstone. Quartz is subangular while chert and lithic grains are commonly well-rounded. Within the concretions, any initial porosity is occupied by now silicified early carbonate and sulfate cement; the dominant cement in the host rock consists of metamorphically altered tuffaceous material, resulting in the formation of fine-grained white mica. Intergranular contacts are linear, rarely concave-convex. Bulk sandstone composition is dominated by volcanic and plutonic rock fragments (30-50%) and monocrystalline quartz (20-30%). Chert and polycrystalline quartz account for about 5-10% each. Feldspar, almost exclusively microcline, is very rare (< 2%). Heavy minerals (pyrite, zircon and chromite) are accessory and enriched in mm-thin laminae. The remaining space is mainly occupied by authigenic white mica and subordinate chlorite. Rock fragments are generally intensely sericitized. Some of them contain remnants of the precursor material, i.e., plagioclase and quartz, or show internal mica alignment that resembles remnant twinning or cleavage of feldspar. Heubeck and Lowe (1999) described this grain type as quartz-sericite grains (QS) and suspected an origin from hydrothermally altered metavolcanic grains of intermediate chemistry. Counting grains that resemble feldspar as feldspar, the sandstone is reclassified (McBride; 1963) as feldspathic litharenite or lithic subarkose (Fig. 3.6).

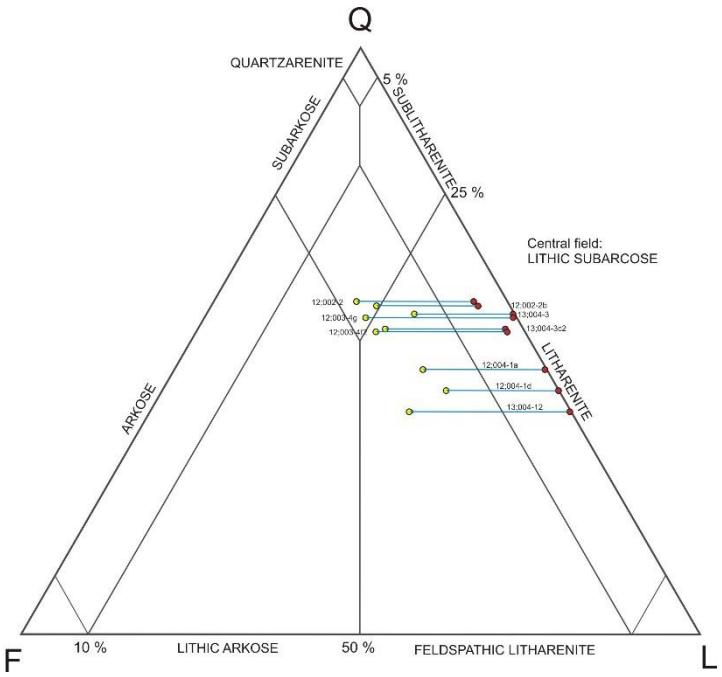

Figure 3.6: Quartz (Q) - Feldspar (F) - Lithics (L) ternary diagram (McBride, 1963) showing framework composition of nine concretion-bearing sandstone samples of unit MdQ1 in the Stolzburg Syncline. All samples plot in the litharenite field. If sericitized grains which show remnants and textures of feldspar are counted as F, overall sandstone composition would plot in the lithic subarkose and feldspathic litharenite field.

3.5.2. Morphology of concretions

Concretions are commonly made up of idiomorphic, up to 0.5 cm long and typically radially-inward pointing, aligned megaquartz crystals and poikilotopic quartz cement domains. Four concretion types can be distinguished based on morphology and internal structure; transitions between these types are common. Three types of concretions show at least one central cavity that is either filled by fine-grained muscovite or by quartz (Figs. 3.7-3.11).

Type I, Unzoned Concretions (Figs. 3.7 and 3.11A): Type-I concretions are composed of large patches containing megaquartz filling former pore space in sandstone. Patches overgrow grains which commonly show less alteration than those in the surrounding sandstone. The quartz cement shows a poikilotopic texture with several domains of undulatory extinction patterns (Fig. 3.7B). Cathodoluminescence (CL) shows that cementation started as overgrowth on detrital grains. An isopachous drusy quartz cement appears as rim of whitish CL color and euhedral shape (Fig. 3.7C) around numerous grains that show no mechanical compaction (Fig. 3.7A). Both the poikilotopic and the isopachous cements contain numerous, up to 40 µm large, bright and rounded inclusions. Microprobe analyses show that inclusions within quartz consist predominantly of anhydrite (Table 3.1) and rarely of calcite. Concretions of this type occur in the lower half of concretionary beds and appear either randomly distributed or aligned along existing sedimentary structures (Fig. 3.11E).

Interpretation: The formation of isopachous drusy and poikilotopic cements is a typical early-diagenetic process that usually precipitates calcite and gypsum in the vadose zone (Adams et al., 1984; Reijers and Hsü 1986). The occurrence of remnant anhydrite inclusions shows that the initial cementation was likely by gypsum that dehydrated to anhydrite during burial.

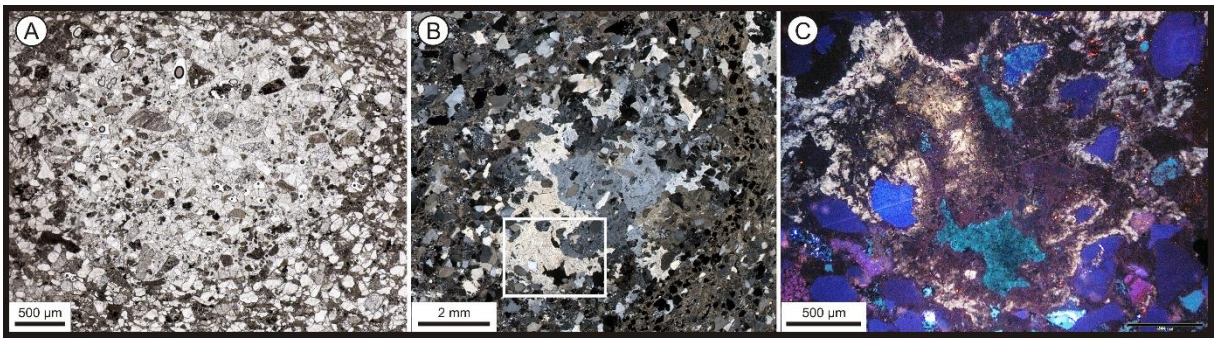

Figure 3.7: Photomicrographs and cathodoluminescence (CL) images of Type-I concretions and cementation stages therein. A) Type-I concretion enriched in detrital grains. The grains show no mechanical compaction and are held in place by early diagenetic poikilotopic cement. B) Photomicrograph of Type-I concretion under cross-polarized light. The concretion is composed of poikilotopic quartz cement. Individual domains extinguish at different angles, a typical texture of early diagenetic poikilotopic calcite and gypsum cement. The area outlined by the white rectangle is enlarged in Fig 7C. C): CL image of part of a Type-I concretion showing abundant detrital grains (bluish) and surrounding quartz cement (purple and whitish). The whitish cement resembles a former isopachous drusy gypsum cement. It contains numerous anhydrite inclusions.

Type II, Concretions with quartz and muscovite (Figs. 3.8 and 3.11B): Concretions of Type II resemble those of Type I as both are mainly composed of a thick poikilotopic quartz rim. Type II-concretions display a central cavity usually filled by yellowish fine-crystalline muscovite and rarely by detrital quartz grains (Figs. 3.8A and B). The thick quartz rim contains abundant anhydrite inclusions (Table 3.1; Appendix B2) and incorporated detrital material that shows the same overgrowth patterns of the early isopachous drusy cement with whitish CL color as Type-I concretions. Quartz in Type-II concretions also shows poikilotopic textures but combines them with idiomorphic inward-pointing crystal faces, including an exceptionally high number of anhydrite inclusions (Figs. 3.8B and C). The central matrix is mainly composed of almost pure fine-grained muscovite which incorporates few detrital quartz grains and is devoid of sulfates and carbonates. Concretions of this type occur throughout the concretionary beds (Fig. 3.11E) except at the very base (where only Type-I concretions occur) and the very top of such beds (where concretions of Type IV occur; see below). They tend to form botryoidal bodies and agglomerates in the upper parts of sandstone beds and appear as prominent hollow spheres in weathered rock faces (Figs. 3.4D, 3.5A).

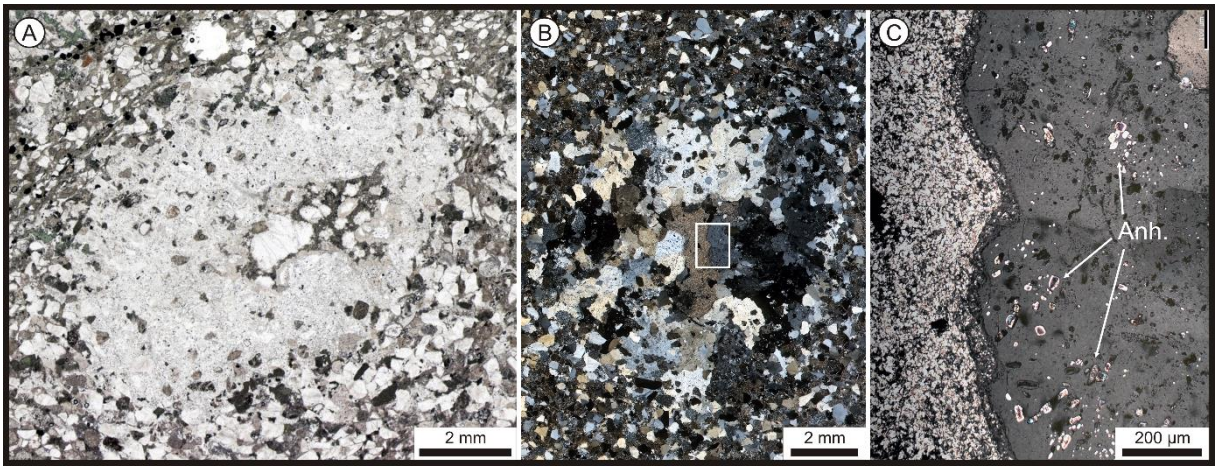

Figure 3.8: Photomicrographs of Type-II concretions. A) Type-II concretion with central cavity filled by detrital quartz B) Photomicrograph of Type-II concretion under cross-polarized light. The concretion is mainly composed of poikilotopic quartz cement. Individual domains are at different extinction positions. The central cavity is filled by fine crystalline muscovite. Adjacent quartz crystals show inward-pointing faces. The area outlined by the white rectangle is enlarged in Fig. 3.8C. C) Photomicrograph under cross-polarized light showing inward-pointing broad tips of quartz crystals (to the right) with numerous anhydrite inclusions (Anh.). The area to the left is composed of the cavity-filling muscovite matrix.

Type III, Concretions with two quartz phases (Figs. 3.9 and 3.11C): These concretions are composed of two easily distinguishable zones: An outer, rim- forming zone of idiomorphic, inward-pointing, up to 5 mm large quartz crystals and an inner zone of xenomorphic quartz crystals (Fig. 3.9A). The proportion of sulfate and carbonate inclusions in the idiomorphic crystals is comparatively high. The most abundant inclusions are anhydrite, followed by barite and a calcium carbonate with strontium contents of up to ~2% (Table 3.1), identified as calcite using Raman spectroscopy (Appendix B3). As a result, the quartz crystals appear cloudy. The pronounced faces of these crystals are surrounded by accumulations of very small (< 5 µm) fluid and gas inclusions. Some of these idiomorphic crystals show an internal zonation best visible using CL (Figs. 3.9D and E). They demonstrate small palisades of columnar and bladed quartz pseudomorphs after calcite that were not entirely silicified and in places still contain calcite remnants. The material surrounding these crystals has a whitish CL color and shows pseudomorphic crystal shapes including swallow-tail twinning, indicative of a precursor gypsum mineralogy (Figs. 3.9E-G). The predominant types of inclusion in this phase are sulfates such as anhydrite and barite.

The second and younger quartz phase is clear, free of inclusions, and completely fills the remaining space in the center of the concretions and is thus xenomorphic. It shows colors and an internal zonation under CL which are described as typical of hydrothermal quartz (Götze et al., 2001; Götze and Möckel, 2012; Götze et al., 2015). Type-III concretions rarely show

concentrations of fine-grained detrital material at the contact to the surrounding sandstone. In some concretions, crystals of the earlier quartz phase show a partly dissolved outline and are surrounded by an above-average concentration of small fluid and gas inclusions as well as by globular, mostly barite and rarely anhydrite inclusions of similar size (Figs. 3.9B and C). These inclusions are radially aligned around the partly dissolved crystals trapped in the secondary quartz that fills the center of the concretions. The outer quartz generation of Type-III concretions shows a high similarity in shape and structure to authigenic quartz crystals that have been described, e.g., from the anhydritic "hard salt" unit of the Zechstein (Götze et al., 2001; Götze and Möckel, 2012) or from anhydrite nodules from the Triassic of central Spain (Alonso-Zarza et al., 2002). Concretions of this type predominantly occur in the upper part of concretion-bearing beds in coalesced concretions and just below them. Within the crusts, they commonly build up complex agglomerates and botryoidal bodies associated with other concretion types (Fig. 3.11E).

Interpretation: The observed zonation of the idiomorphic crystals that form the outer phase suggests a two-phase growth process that started with the precipitation of the high-strontium carbonate crystals with columnar or bladed habit followed by the formation of sulfates that filled the remaining space between the carbonate crystals. The sulfates resemble the isopachous drusy cement observed in Type-I and -II concretions and in places show textures reminiscent of swallowtail and dendritic twinning, characteristic of gypsum (Figs. 3.9E-G). Metasomatic replacement of the concretions by quartz preserved the original shape and textures. The quartz shows a whitish CL color where it replaced sulfates. Even though carbonate inclusions are calcite today, their high strontium content point towards an aragonite precursor. Aragonite precipitation however, is well known from Archean carbonates such as the Campbellrand-Malmani carbonate platform (Sumner and Grotzinger, 2004).

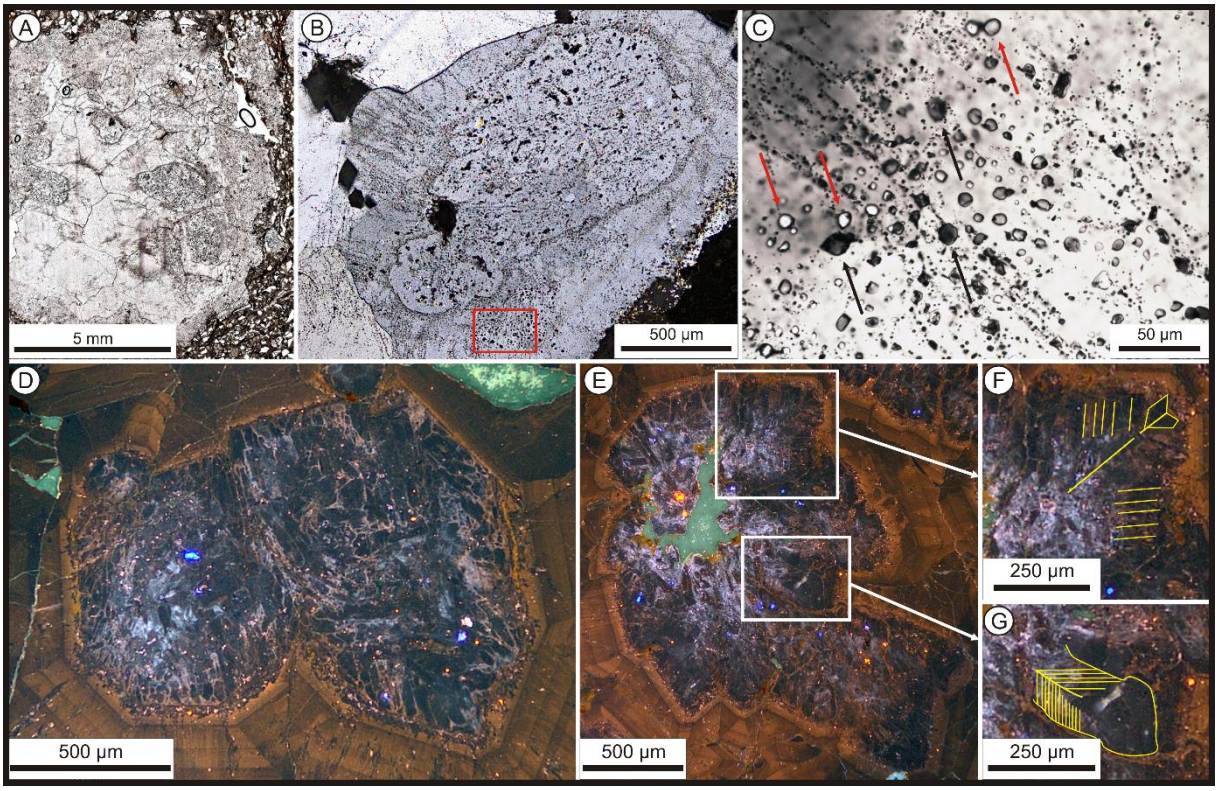

Figure 3.9: Photomicrographs and CL images of Type-III concretions. A) Concretion with a rim of idiomorphic inward-pointing quartz crystals. The crystals contain numerous sulfate and calcite inclusions which result in the cloudy pattern. Xenomorphic quartz in the center is free of inclusions and therefore appears clear. B) Photomicrograph under cross-polarized light of partly dissolved, inclusion-rich quartz crystal and surrounding, mostly globular gas, fluid and solid inclusions. The area outlined by the red rectangle is enlarged in Fig. 3.9C. C) Photomicrograph of quartz showing dark gray and greenish barite (black arrows) and bright to transparent gas and fluid (red arrows) inclusions < 10 µm in diameter. D) Idiomorphic, inward-pointing quartz crystal grown within a concretion cavity. The crystal shows internal zonation and is composed of columnar former calcite crystals (dark gray) surrounded by former sulfates (whitish CL color), both replaced by quartz. Secondary, inclusion-free zoned quartz (orange) overgrows both. E) Idiomorphic quartz crystal replacing columnar former calcite crystals (dark gray) and former sulfate (whitish). Green areas represent porosity. The crystals show areas marked by white rectangles of dendritic and swallow-tail twinning which are enlarged in F) and G).

Type IV, Complex concretions (Figs. 3.10 and 3.11D): Complex concretions form the largest concretions and reach diameters of up to 3 cm. Concretions of this type show additional growth phases. Their rim is composed of cloudy, calcite- and barite-inclusion-rich and commonly idiomorphic quartz crystals with whitish CL color (Figs. 3.10A-C; Table 3.1). These quartz crystals contain pseudomorphs after a mineral with columnar and bladed habits (Fig. 3.10C). Some of these minerals have not been completely replaced by quartz but are composed of calcite with high strontium contents (Table 3.1) indicating an aragonite precursor. The columnar and bladed minerals are surrounded by a second cement generation with the same whitish CL color as described from the other concretion types. This second-generation cement contains

predominantly barite inclusions while anhydrite inclusions are rare. Incorporated clasts are almost absent but include hyalophane and celsian, two varieties of barium feldspars. Up to three additional generations of quartz cement can be recognized in Type-IV concretions: (1) A clear xenomorphic quartz cement free of inclusions but with growth zonation visible in CL images; (2) a quartz phase with a high proportion of muscovite but composed of idiomorphic, up to 5 mm long, inward-pointing crystals; and (3) a xenomorphic, inclusion-free quartz generation which grew in the muscovite-filled central cavities. Due to the complex structure and the large size of Type-IV concretions, commonly more than one central cavity occurs. Thus, up to five zones can occasionally be distinguished in Type-IV concretions: The inclusion-bearing rim quartz, three late phases of pure quartz and the cavity-filling muscovite matrix (Figs. 3.10A, 3.11D). Complex concretions appear to be restricted to the upper quarter of concretionary beds (Fig. 3.11E). Their size and complexity indicates that they coalesced from several single bodies.

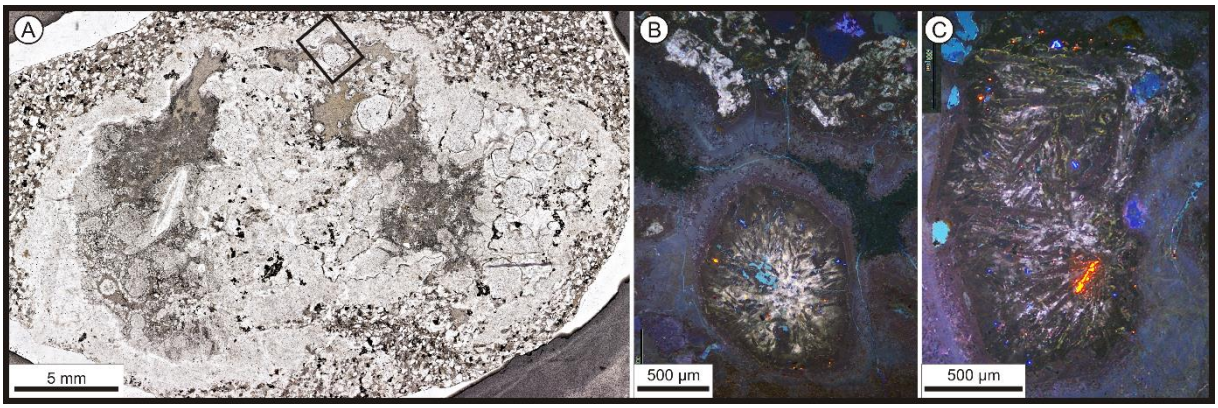

Figure 3.10: Photomicrographs and cathodoluminescence images of Type-IV concretions. A) Concretion with two muscovite-filled cavities (dark brown) surrounded by several quartz phases that partly replaced former calcite and sulfate cements. Area outlined by black rectangle is shown in B). Cathodoluminescence image of idiomorphic quartz crystal (lower part of image) and of concretion rim (top), both showing the typical white CL color of sulfates replaced by quartz. The idiomorphic quartz crystal is partly surrounded by muscovite matrix (dark) and non-replacive late diagenetic quartz (light purple). C) Cathodoluminescence image of idiomorphic quartz with columnar and bladed pseudomorphs after calcite. One of the bladed crystals is composed of calcite and has a bright orange CL color (lower right). The columnar and bladed crystals are surrounded by quartz with whitish CL color typical of quartz that replaced sulfates. Whitish areas contain numerous barite and a few anhydrite inclusions.

Despite all complexity, the four concretion types are usually similar and consistently distributed in the concretion-bearing beds. Type-I and -II concretions (dominated by anhydrite inclusions) are usually concentrated in the lower part of concretion-bearing beds where the number and density of concretions is generally low but their abundance increases towards the top of the beds. Higher up, Type-III concretions, which are in part anhydrite- and in part calcite/barite-dominated, occur in a zone where concretions start to accrue in distinct layers. Complex,

calcite- and barite-bearing concretions of Type IV dominate the upper part of concretionary beds (Fig. 3.11E).

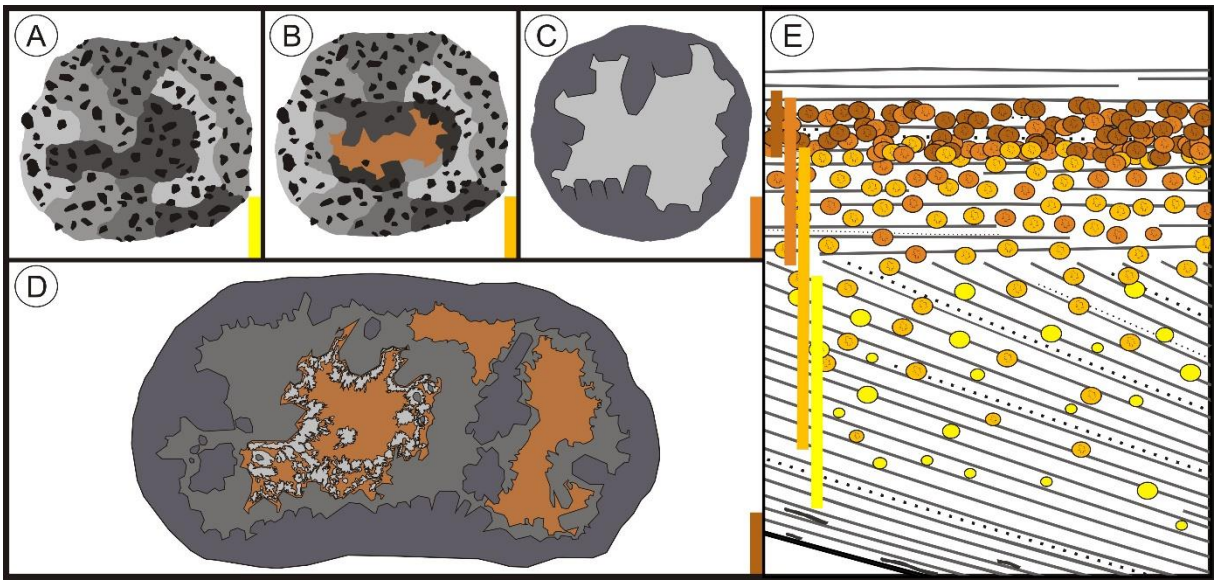

Figure 3.11: Schematic sketches illustrating the main characteristics of the four concretion types (A-D) and their relative positions within concretion-bearing beds (E). A) Type-I concretion composed of poikilotopic cement (gray) that incorporates detrital sand grains (black). B) Type-II concretion composed of an outer quartz rim of unzoned poikilotopic quartz cement with some idiomorphic, inward-growing and inclusion-rich crystals (gray). Fine-grained muscovite (orange) fills the interior. C) Type-III concretion showing two phases of quartz growth. The older, outer, rim-building quartz generation is composed of idiomorphic, inclusion-rich crystals that grew towards the center (dark gray). A younger generation is composed of clear, blocky, xenomorphic quartz that fills the space not occupied by the earlier phase (light gray). D) Type-IV complex concretion. Besides the inclusion-rich quartz rim (dark gray), up to three more phases of quartz crystal growth (medium and light gray) which compartmentalize the central muscovite filled void (orange) into several cavities can be distinguished. E) Schematic drawing showing the distribution of concretion types within a concretion-bearing bed. Color bars represent stratigraphic extent of each concretion type. Type-I and -II concretions, dominated by anhydrite inclusions, are concentrated in the lower part of the channel. Type-III and -IV concretions, which dominantly contain calcite and barite inclusions, dominate its upper part.

Table 3.1: Electron microprobe analyses of elemental composition of inclusions in pseudomorphic quartz from concretions in sandstones of unit MdQ1 of the Stolzburg Syncline. Measured elements are presented as oxides.

Mineral	Calcite						Barite			
Sample nr.	13;004-3a	Type-IV		13;004-3	Type-IV		13;004-3	Type-IV		
Analysis nr.	1	2	3	1	2	3	1	2	3	4
Al_2O_3	0.014	bdl	0.014	0.012	0.023	0.01	0.066	0.035	bdl	0.045
K_2O	0.013	bdl	bdl	bdl	bdl	bdl	0.022	0.037	bdl	bdl
SO_3	0.126	0.061	bdl	0.14	0.076	0.653	33.06	33.479	33.384	33.574
FeO	0.344	0.472	0.444	0.233	0.245	0.226	bdl	0.01	bdl	bdl
CaO	52.887	53.079	57.782	53.222	53.249	54.156	0.017	0.048	0.024	0.034
SrO	0.182	0.687	0.991	0.231	0.115	1.014	bdl	0.719	1.636	1.766
BaO	0.04	bdl	0.042	bdl	0.05	0.016	61.915	61.485	60.354	59.829
SiO_2	0.359	0.083	0.097	0.111	0.143	0.106	bdl	0.073	0.062	0.146
Na_2O	bdl	bdl	0.01	bdl	bdl	bdl	0.219	0.19	0.124	0.046
MgO	0.186	0.254	0.126	0.279	0.097	0.248	bdl	0.014	bdl	bdl
Total	54.151	54.636	59.506	54.228	53.998	56.429	95.299	96.09	95.584	95.44

Mineral	Calcite				Barite			Anhydrite		
Sample nr.	13;004-4b	Type-III			13;003-4a	Type-III		13;003-4a	Type-III	
Analysis nr.	1	2	3	4	1	2	3	1	2	3
Al_2O_3	0.002	0.012	0.033	0.036	0.078	0.056	0.064	bdl	0.006	0.007
K_2O	0.020	bdl	0.005	0.011	bdl	bdl	0.028	0.020	0.119	bdl
SO_3	0.033	0.039	0.041	0.061	32.840	33.221	32.521	52.884	53.022	53.444
FeO	1.929	1.803	0.973	0.010	0.020	bdl	bdl	0.042	0.023	bdl
CaO	55.503	54.497	55.206	55.153	0.026	0.037	0.026	42.257	41.592	41.985
SrO	bdl	0.147	1.994	bdl	2.117	0.675	1.302	bdl	bdl	bdl
BaO	bdl	0.467	0.227	bdl	60.450	62.586	61.636	bdl	bdl	bdl
SiO_2	0.317	0.425	0.703	0.600	0.169	0.079	0.056	0.700	1.058	0.812
Na_2O	0.021	0.015	bdl	bdl	0.241	0.221	0.172	0.045	0.034	0.009
MgO	0.764	0.396	0.562	0.427	0.020	0.012	0.035	bdl	bdl	bdl
Total	58.589	57.801	59.744	56.298	95.961	96.887	95.840	95.948	95.854	96.257

Mineral	Anhydrite									
Sample nr.	12;003-4a	Type-II		12;003-4f	Type-I					
Analysis nr.	1	2	3	1	2	3	4	5	6	7
Al_2O_3	0.016	bdl	bdl	bdl	bdl	0.011	bdl	bdl	bdl	bdl
K_2O	bdl	bdl	0.026	0.27	0.031	bdl	bdl	bdl	bdl	0.025
SO_3	54.767	54.612	54.249	54.867	55.189	54.776	55.156	55.323	54.57	55.446
FeO	0.029	0.025	0.025	bdl	bdl	0.025	bdl	0.016	bdl	0.027
CaO	41.532	41.207	41.165	41.399	41.945	41.756	41.877	41.87	42.053	41.999
SrO	bdl	bdl	bdl	bdl	bdl	bdl	0.013	bdl	bdl	bdl
BaO	0.016	bdl	0.023	0.041	bdl	bdl	0.033	0.03	0.029	bdl
SiO_2	0.309	0.283	0.69	0.161	0.058	0.166	0.439	0.175	0.099	0.206
Na_2O	0.041	0.039	0.004	0.041	0.106	0.062	bdl	0.038	0.046	0.02
MgO	bdl	bdl	bdl	bdl	bdl	bdl	bdl	bdl	bdl	bdl
Total	96.710	96.166	96.182	96.779	97.329	96.796	97.518	97.452	96.797	97.723

3.5.3. Other evaporitic features

In a few places, up to 6 cm thick silicified crusts topping fine-grained to silty, rippled to wavy-laminated, tuffaceous sandstone with a sharp contact occur in the concretion-bearing MdQ1 sandstone (Fig. 3.12A). These crusts consist almost exclusively of quartz crystals which show pseudomorphs resembling those in the concretions but are less well preserved, and contain inclusions of sulfates and carbonates. The upper surface of the crusts is bulbous and shows a relief few cm-high (Fig. 3.12B). These crusts may represent concretionary beds exhumed by erosion during Moodies time. Their occurrence on top of low-permeable, fine-sandy to silty tuffaceous beds implies their formation as evaporitic, perhaps efflorescent crusts (Smoot, 1994; Goodall et al., 2000; Warren, 2006).

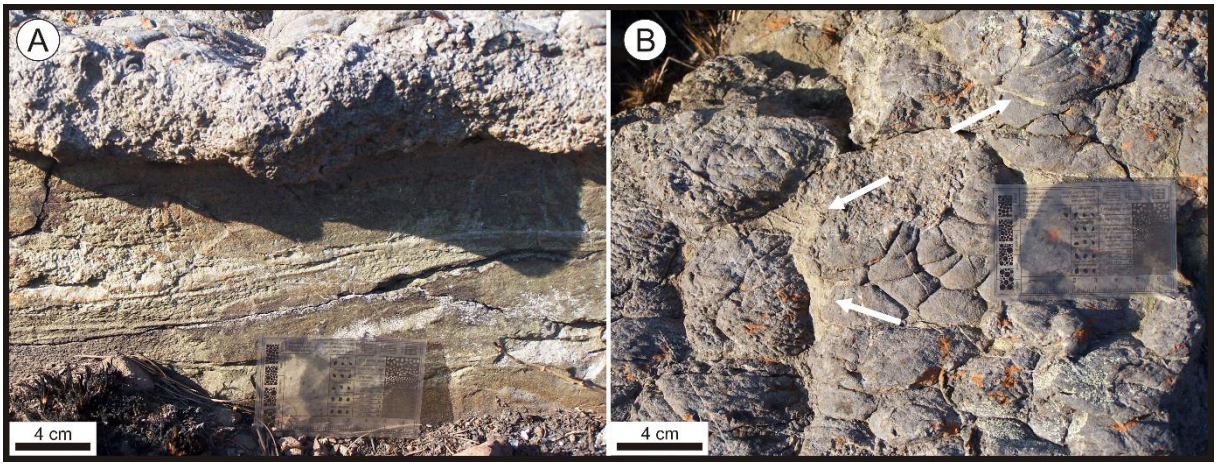

Figure 3.12: Silicified evaporitic crusts. A) Wavy-laminated, tuffaceous, silty sandstone topped by an about 6 cm thick silicified evaporitic crust. Note the sharp contact between the crust and the sandstone. B) Top view of the surface of the same crust showing bulbous relief and sediment-filled pockets (white arrows).

Aside from the concretions and the related silicified crusts, early diagenetic evaporative crusts occur in several other locations through the lower Moodies Group in the BGB, interbedded with thin- to medium-bedded, medium-grained, dominantly horizontally stratified, low-angle cross-bedded and rippled sandstones, associated with concretion-bearing beds and tidal-facies microbial mats. These crusts reach 1-5 cm thick, are planar and bedding-parallel and typically consist of chocolate-brown weathering, ferroan-dolomite-cemented sandstone. Crusts are variably modified: (1) Early and preferentially-cemented ridges form a pseudopolygonal network at the top of a sandstone bed in the coastal facies of the Dycedale Syncline (Figs. 3.13A, B). They differ from desiccation cracks because there is no topping shale. Sand ridges taper distinctly upwards. They are thus best interpreted as teepee structures in which a brittle, thin crust on surficially indurated sandstone was polygonally broken and underlying sand

preferentially cemented by drying-wetting cycles. (2) In other places, best exposed at the Clutha Creek section of Eureka Syncline, segments of brown, ferroan-dolomite-indurated crust have been reworked into several thin, nearly monomict intraclast conglomerates (Fig. 3.13C). In map view, the angular margins of the clasts can be seen to still be nearly parallel to each other, suggesting only minimal displacement of the broken crusts, perhaps aided by some aqueous winnowing of the angular shards by currents. An origin of the brown intraclasts as teepee segments is also suggested by their gradually thinning, pointy tips. (3) Interbedded coastal-facies sandstones are slumped at a scale of several m and show in cross section a disrupted internal stratification, marked by zones of brown ferroan dolomite cement in elongate rounded bodies, floating hinges, and curvilinear slivers up to several meters long, associated with fluid-escape structures (Fig. 3.13D). Indications of structural deformation are absent, and the shape and size of the cemented zones negate their interpretation as clasts. Rather, it appears that zones of weak preferential induration in the shallow subsurface were disrupted, perhaps by seismic activity or by bank margin slumping in the tidal zone.

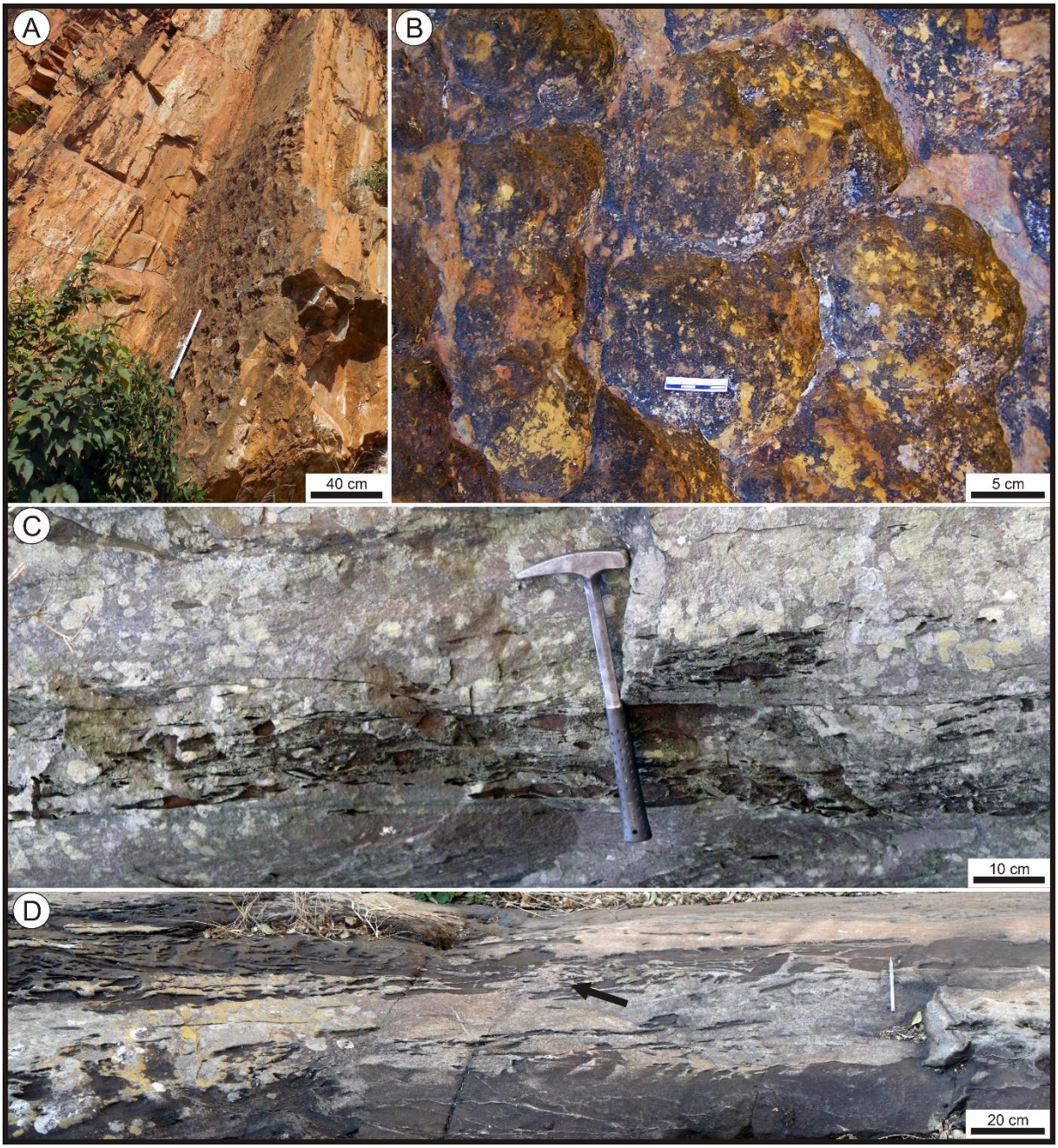

Figure 3.13: Outcrop images of early diagenetic evaporitic crusts. A and B from the Dycedale Syncline, C and D from the Eureka Syncline. A) Bedding plane showing pseudopolygonal network resembling teepee structures; scale is 40 cm long. B) Close up of polygons, up to 15 cm in diameter and about 3 cm deep. Bedding plane contains no shale but variably ferroan-dolomite cemented sandstone. C) Monomict intraclast slab conglomerate showing up to 10 cm long, elongated, brown and angular ferroan dolomite clasts. Well-preserved mudclasts and angle of foresets indicate that flat clasts represent original proportions and are not due to tectonic strain. D) View parallel to bedding of disrupted and slumped evaporative crust composed of contorted, semi-consolidated, ferroan dolomite-cemented sandstone which slumped within unconsolidated sand in a coastal or tidal setting. Black arrow marks a fluid-escape structure about 20 cm high.

3.6. Discussion

3.6.1. Timing of concretionary growth

The wide, shallow, gravelly channels, low-angle foresets, rippled bed surfaces, mud drapes with desiccation cracks and the stratigraphic position of the investigated facies between alluvial facies below and shoreline facies above are excellent indicators of braid-plain sedimentation up-dip from a shoreline. Recurring, possibly seasonal periods of reduced or interrupted sediment supply and variable precipitation in arid braidplains caused strongly fluctuating ground water tables which allowed intensive drying-wetting cycles in the vadose zone and created ideal conditions for pedogenic and early diagenetic processes, including concretionary growth during dry periods associated with rising ground water and evaporation (Retallack, 1991a). Concretionary beds were partly eroded by fluvial channels, and concretions within them were redeposited and mixed with volcanic and chert clasts. This demonstrates their early diagenetic growth and, in addition, requires their surface exposure. The occurrence of different concretion types correlating to vertical height above channel-fill base underlines the concretionary growth as a function of varying groundwater levels (Chowns and Elkins 1974; Chandler, 1988; Retallack, 1991a).

The present composition of the concretions is overwhelmingly quartz which preserved concretionary shapes and original crystal morphologies but largely replaced their original chemical composition. However, remaining, in places abundant inclusions of anhydrite, barite, and carbonate in quartz indicate sulfate and carbonate precursors. The pseudomorphic crystal shape of quartz after calcite and gypsum (Figs. 3.9D-G and 3.10B, C) and the poikilotopic and drusy habit of the initial cement (Figs. 3.7 and 3.8A, B) are additional evidence of mineral replacement. The concretions show internal structures typical of early diagenesis. These include displacive crystal growth by which clay minerals were pushed towards a central cavity while larger and more stable grains remained in position; this, as the preservation of unstable or metastable feldspars and lithic grains within the concretions, is a typical process of early pedogenic concretionary growth (Retallack, 1991a). Type-I and -II concretions are characterized by detrital grain populations with low contact numbers, indicating cementation prior to any significant compaction (Figs. 3.7A and 3.8A).

3.6.2. Chemical conditions and ion provenance

Ca^{2+}, Ba^{2+}, CO_3^{2-} and SO_4^{2-} must have been enriched in the groundwater to precipitate concretionary sulfate and carbonate. Decomposition of detrital feldspar and of porphyritic

subvolcanic and metavolcanic grains is the most plausible process to provide the Ca^{2+} and Ba^{2+} cations. Sources of plagioclase include TTG plutons surrounding the Barberton Greenstone Belt that were emplaced between ~3.5 and ~3.2 Ga (Robb et al., 1986; Tegtmeyer and Kröner, 1987; Armstrong et al., 1990; Kisters and Anhaeusser, 1995; Zeh et al., 2013). Dacites and andesites of the Schoongezicht Formation provided both K-feldspars and subordinate plagioclase (Reimer, 1967; Heubeck and Lowe, 1999; de Ronde and Kamo, 2000; Hessler and Lowe, 2006). Rare remnants of detrital celsian and hyalophane (Barium-feldspar) exclusively preserved within concretions show that these two feldspar varieties may have provided a plausible source of barium.

Anion provenance (CO_3^{2-} and SO_4^{2-}), however, needs to be explained differently. The mid-Archean atmosphere probably had been anoxic with a high CO_2-content of > 6.8 PAL (Hessler et al., 2004; Hessler and Lowe, 2006; Sheldon, 2006; Nisbet et al., 2011). Any surface or near-surface water would therefore be enriched in carbonic acid. Even though Raman spectroscopy shows calcite mineralogy (Appendix B3), the high Sr content of the carbonate points towards a possible aragonite precursor. While carbonate ions are readily provided by atmospheric supply, the near-surface availability of sulfate is problematic due to the low sulfate concentration of Archean ocean water (Boulter and Glover, 1986; Grotzinger and Kasting, 1993; Sumner and Grotzinger, 2004; Eriksson et al., 2005; Gargaud et al., 2005). Ocean water and marine sedimentary rocks are two major sources of sulfates in modern environments (Reimer, 1986; Chivas et al., 1991; Eckardt and Spiro, 1999). The low degree of isotopic fractionation of ^{34}S by microbial sulfate reduction suggests that sulfate concentration in late Archean ocean water was <1% of modern ocean water (Crowe et al., 2014; Paris et al., 2014; Ueno, 2014; Zhelezinskaia et al., 2014). This excludes Archean ocean water as potential source of sulfate. This leaves weathering of basement rocks and terrestrial water as source of sulfate, well known from modern analogs such as the Namib desert and the Australian playas (Visser, 1963; Chivas et al., 1991; Eckardt and Spiro, 1999). However, photochemical modelling shows an additional source of sulfate existed because about 15% of volcanic SO_2 and H_2S could have been converted to sulfate by photolytic disproportionation (Kasting, 1990; Grotzinger and Kasting, 1993; Habicht et al., 2002; Huston and Logan, 2004; Gargaud et al., 2005). This is also the conventional reasoning to explain the presence of sedimentary barite deposits in the 3.5 - 3.2 Ga rock record which would indicate a global, moderately sulfate-bearing, partly oxidized and stratified ocean (Buick and Dunlop, 1990; Lowe and Worrell, 1999; Jewell, 2000; Huston and Logan, 2004). Because there are few if any Archean gypsum deposits, the conventional wisdom maintains that photochemical disproportionation was apparently insufficient to produce enough

sulfate to precipitate widespread gypsum, and a number of researchers thus postulate very low oceanic sulfate levels (Boulter and Glover, 1986; Grotzinger and Kasting, 1993; Sumner and Grotzinger, 2004; Eriksson et al., 2005; Gargaud et al., 2005; Crowe et al., 2014; Paris et al., 2014; Ueno, 2014; Zhelezinskaia et al., 2014). While oceanic sulfate levels may indeed have been low, Moodies concretions are clearly not of marine but of terrigenous and not of primary but of early diagenetic, pedogenic origin. They had grown out of brines that had been concentrated in the shallow subsurface through evaporation. Their accumulation in the extensive braided-fluvial / coastal sabkha plains of the Moodies Group, in particular under climatically variable conditions, is plausible if not probable.

3.6.3. Silification and late (burial) diagenesis

Freshly deposited sands in Moodies coastal zones were probably quite susceptible to silicate weathering due to the fluctuating groundwater level, the high CO_2 content of the Archean atmosphere, and elevated temperatures. Thin section petrography documents as much as 20% sericite and 20-30% quartz-sericite grains in the sands; instable grains of ultramafic and mafic provenance are absent. Thus, Moodies sandstones likely underwent a high degree of in-situ silicate weathering and clay formation which provided a copious source of silica during early diagenesis. Weathering of mafic silicates under slightly acidic conditions resulted in the precipitation of carbonates and sulfates, causing the release of silica to the pore water and the subsequent formation of silica cement (Daval et al., 2009 and 2010; Ghosh and Bhattacherjee, 2013). Postulated Archean weathering conditions in general and particularly for the Moodies Group are thought to have been aggressive (Corcoran and Mueller, 2004; Hessler and Lowe, 2006), leading to a substantial degradation of mafic material, plagioclase and instable rock fragments.

Weathering and dissolution of feldspar produces clay minerals, resulting in a high content of sericite in Moodies sandstone. These weathering reactions take place in weakly acidic environments in which the solubility of silica is reduced (Chan, 1989; Rimstidt, 1997). Silica solubility can be significantly increased by enriching pore water in Ca and Na (Sedletskiy, 1971; Götze and Möckel, 2012) which drives pH to the alkaline. Subsequent precipitation of gypsum and Ca-carbonate removed Ca from pore water, reducing the pH and causing a decrease in silica solubility, especially near the newly precipitated minerals. Such a mechanism would trigger an early precipitation of silica cement as well as the nucleation of idiomorphic quartz crystals induced by sulfate precipitation (Grimm, 1962; Götze and Möckel, 2012). Because braidplain-facies Moodies sandstones are generally not quartz-cemented, the initial

precipitation of sulfates and carbonates may have acted as catalysts for local silica precipitation near the concretions. This likely stiffened and hardened the concretions and allowed their unique morphological preservation. The subsequent silica replacement of gypsum trapped within such a stabilizing silica shell occurred from the outside towards the center and created inward-growing quartz crystals. The excellent preservation of characteristics typical of sulfates and carbonates, such as early isopachous drusy and poikilotopic cements, swallowtail twinning and the preservation of inclusions of these early cements in quartz crystals strongly suggest the early, near-surface replacement of the evaporitic minerals by quartz and the near-absence of subsequent alteration. The medial quartz cement with partly idiomorphic shape in some concretions, especially those of Type III and IV and rarely of Type II, indicates that the silica availability in the pore solution was at least locally sufficient for the additional precipitation of non-replacive quartz. A late source of silica could have been provided by the smectite-illite transformation (Bethke and Altaner, 1986; Weaver, 1989; Retallack, 1991a), followed still later by low-grade-metamorphic upgrading of illite to sericite and muscovite (Retallack, 1986; Holland et al., 1989; Retallack, 1991a) during one of the numerous late Archaean and possibly Paleoproterozoic tectono-thermal overprints.

3.6.4. Concretion stratigraphy

Concretion-bearing sandstone beds contain anhydrite-rich concretions in their lower parts and calcite- and barite-rich concretions in their upper parts. This distribution is likely related to the spatial and temporal availability of ions in the pore water of a fluctuating ground water table. Several diagenetic sequences could be reconstructed, among which the following sequence of events appears to us most likely: (1) Carbonate-dominated crystal precipitation first near the surface, triggered by high Archean atmospheric CO_2 dissolved in meteoric surface water, concentrated by evaporation. (2) Sulfate present in this solution precipitated as barite. (3) When groundwater level fell, concretions formed in the lower parts of concretionary beds. Because CO_2 dissolved in ground water had already been largely consumed by carbonate precipitation, gypsum precipitated preferentially in the underlying strata as Type-I and Type-II concretions. Between these two zones, a mixing level with Type-III concretions formed which contained both calcite and gypsum and shared morphological similarities with the overlying and the underlying concretions. (4) Capillary rise of pore fluids caused by evaporation maintained the growth of concretions in the upper level where barite and gypsum could overgrow the carbonates and form Type-IV concretions and coalescent crusts. Thus, the internal stratigraphy of concretionary beds suggests a complex, drawn-out history of groundwater fluctuation in

sandy sediment and implies that these beds underwent pedogenesis resulting in the formation of an Archean paleosol.

3.6.5. Pedogenic processes

The common occurrence of sand-filled mud-cracks in topping shales adjacent to concretionary sandstones, the erosional truncation of many coalesced concretionary crusts by fluvial channels, and the reworking of concretions as gravel clearly demonstrate that concretionary crusts had been exposed to surface processes. Concretionary growth thus occurred very early and prior to compaction. The systematic and gradual stratigraphic-upward increase of concretion abundance, size and concentration within each single concretionary sandstone bed indicates that concretionary growth followed physico-chemical equilibrium processes between the sediment surface and the groundwater table. Thus, Moodies concretions formed by pedogenic processes in the vadose zone as a result of interactions between variable sediment compositions, the distribution of porosity and permeability, the fluctuating groundwater table and possibly similarly fluctuating atmospheric factors (Francis, 1986; Retallack, 1991). They may also have been affected by biological processes.

The occurrence and stratification of calcareous and gypsiferous concretions and the comparatively high proportions of unstable, easily weathered clasts including feldspar and lithic fragments characterizes the Moodies concretionary sandstones as Aridisols (Mack et al., 1993; Retallack, 1993; Retallack, 1997; Retallack and Huang, 2010) or, alternatively, Entisols or Andisols (US classification). Despite the high degree of sedimentary recycling in the Moodies coastal-fluvial braid-plain, there are several localities within the MdQ1 sandstones, in particular of the Stolzburg Syncline, in which complete paleosol profiles are preserved. At the top, the Ack horizon commonly displays coalesced, broadly stratiform, multiple-growth silicified carbonate concretions. This horizon, usually 5 to 20 cm thick (Figs. 3.4D, 3.5A and C), largely lacks well-preserved relict sedimentary structures but contains a high proportion of shale and reworked volcanic ash. Underlying gypsiferous (Acy) horizons are generally sandier; in them, concretions are spottier and their distribution commonly follows permeability fairways along the preserved sedimentary structures (Figs. 3.5A and C).

Aridisols, which acquire their characteristics less by chemical weathering than by mineral precipitation from oversaturated pore waters, can form quickly. The laterally poorly confined, aggradational, extensive coastal and braidplains of early Moodies time are likely to have allowed for sufficient time periods of exposure, mineral weathering, and Aridisol formation (Bridge and Leeder, 1979; Kraus and Aslan, 1993; Kraus and Gwinn, 1997; Kraus, 1999).

Episodic rapid siliciclastic sedimentation formed weakly developed, stacked Aridisol crusts separated by somewhat weathered sediments, so-called compound paleosols (Kraus, 1999). The time required to form the concretionary crusts can only be estimated because vadose-zone geochemistry is strongly dependent on the ion concentration. Ion concentration itself is a function of numerous variables, such as the sediment fabric, the alteration rate of volcanic ash and unstable lithic and metastable feldspar grains, the degree of incursion of a subsurface marine groundwater tongue and its salinity, and the tidal regime. Judging from recent analogs in arid to semiarid coastal environments, concretionary growth may occur within weeks to months; for example, beach rock is known to form seasonally. A semiarid or fully arid climate is not necessary if alteration of the highly reactive felsic volcanic ash, thinly interspersed with the braidplain sands, occurred rapidly and as long as vadose-zone pore water movement was occasionally upward-directed, facilitating oversaturation of dissolved ionic species and concretionary growth. High ambient temperatures postulated for the Archean (Knauth and Lowe, 2003; Knauth, 2005) and a high proportion of greenhouse gases such as CO_2 and CH_4 created an efficient, possibly even aggressive weathering environment during Moodies time (Corcoran and Mueller, 2004; Hessler and Lowe, 2006) with high alteration rates and an elevated reactivity of minerals.

Even though extensive microbial mats from shoreline and tidal environments are well documented from laterally adjacent and stratigraphically overlying units of the Moodies Group (Noffke et al., 2006; Heubeck, 2009; Gamper et al., 2012; Homann et al., 2015), they have not been observed in the concretion-bearing fluvial-to-sabkha setting described here. However, microbial-mat-bearing sandstones and conglomerates in the Dycedale Syncline immediately underlie concretionary sandstones and can therefore be inferred to have occurred virtually contemporaneously in settings which were adjacent or at most a few km apart. The concretionary sulfates, growing in a moist vadose zone updip from a habitat densely populated by microbial mats, may have been an attractive source of reactants for anaerobic bacterial sulfate reduction. The observed early diagenetic pyrite growth and carbonate precipitation within the concretion-bearing paleosols may also point towards microbial activity in these beds.

3.7. Conclusions

Sulfate and carbonate concretions in the lower Moodies Group (ca. 3.22 Ga) of the Barberton Greenstone Belt formed widely in a braided-fluvial setting which interfingered with a sabkha-type coastal plain. Intensive chemical weathering, the reactive Archean atmosphere, and readily

available metastable minerals, volcanic lithic fragments, and thin rhyodacitic tuffs, together with fluctuating ground water levels contributed to the rapid alteration of sandy sediment and provided ample cations in solution. Crust and concretionary growth in the sandy and gravelly sediment occurred repeatedly from concentrated brines enriched in sulfate and carbonate and was possibly supported by variable sedimentation and precipitation rates and a fluctuating groundwater level, characteristic for recent semiarid climates. The four recognized types of concretions occur at specific levels within thick sand beds and appear to reflect paleohydrological conditions. Locally abundant and rock-forming calcite and barite concretions preferentially precipitated in the upper part; less abundant gypsum-dominated concretions precipitated in the lower part of the vadose zone. The concretionary beds can therefore be viewed as primitive aridisols that show upper calcareous (Ack) and a lower gypsiferous (Acy) horizons. The excellent preservation of their sedimentary structures may have occurred quickly, possibly even within a single drying cycle, judged from the internal textures of the concretions. The excellent preservation of the concretions, however, is related to the early diagenetic pseudomorphic replacement of carbonate and sulfate crystals by silica which predated burial and prevented the concretions from compaction and subsequent metamorphic alteration. The occurrence of Moodies concretionary beds likely represents the oldest terrestrial evaporites known to date; they form the oldest known compound paleosols.

Acknowledgements

This research was funded by the DLR (German Aeronautics and Space Research Center) and the Helmholtz Alliance “Planetary Evolution and Life” under grant X/957/67147527 to CH. The Authors thank Martin Homann, Danielle Zentner, Paul Fugmann and Henry Nordhauß for assistance in the field and the Nel family for hospitality and help. We thank Ralf Milke for providing access and assistance with the electron microprobe of the mineralogy group of the Freie Universität Berlin. Mrs. Anna Giribaldi, FU Berlin, and Sigried Bergmann, FSU Jena, are thanked for thin section preparation. The authors are grateful to Sappi Limited and their forestry managers, especially to Tiro Hlanyane, for permission to access private forest roads and for advice on local conditions. Wlady Altermann and an anonymous reviewer are acknowledged for their detailed and helpful comments that helped to improve the paper.

4. Biogenic overgrowth on detrital pyrite in ca. 3.2 Ga old Archean paleosols

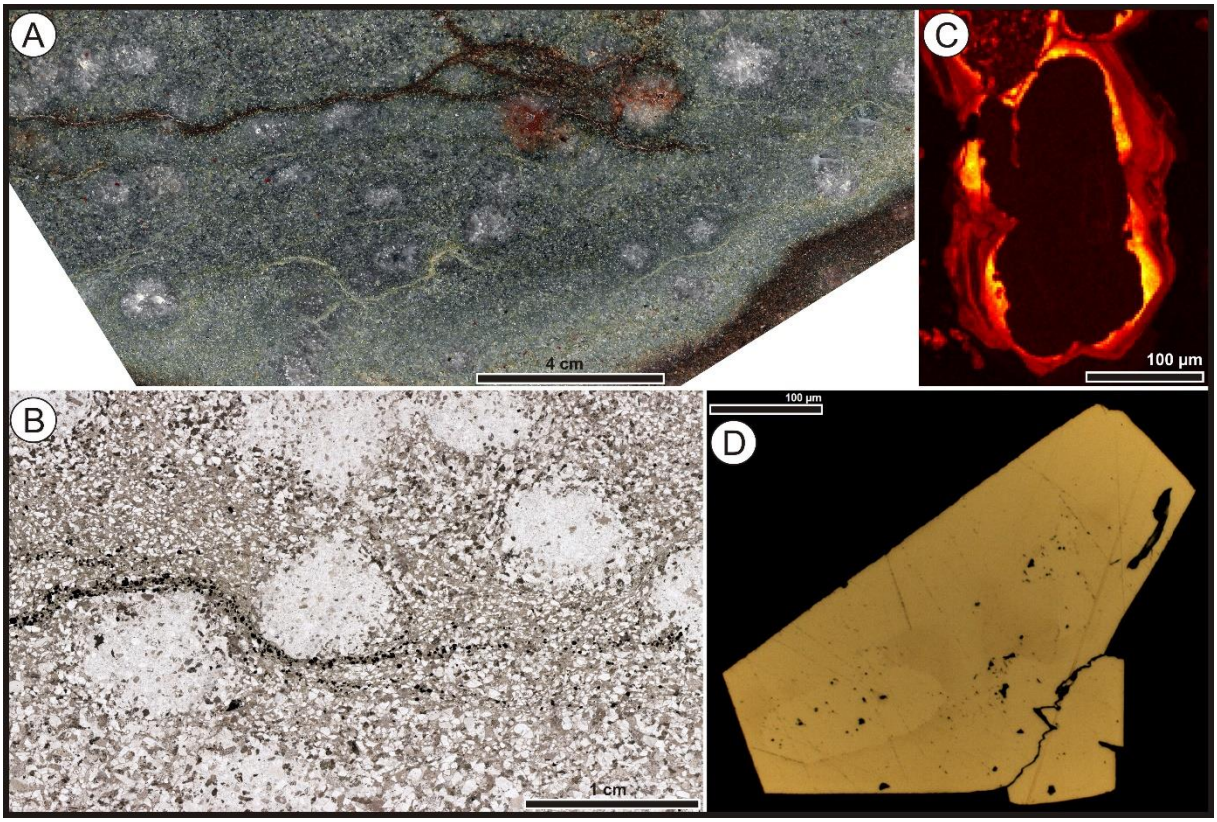

Title Figure: Detrital and secondary pyrite of sample 12;003-4 on different scales. A: Polished slab with heavy mineral lamination. B: Thin section with heavy mineral lamination C: Ni map of a pyrite and D: RL image of detrital pyrite overgrown by secondary pyrite.

This chapter is mainly about:

- Pyrite in paleosols of the Archean Moodies Group
- Trace elemental and S-isotopic composition of detrital and authigenic pyrite
- Microbial sulfate reduction (MSR) related to pyrite formation
- Microbial life in ~3.22 Ga old terrestrial environments

Keywords: Archean, Pyrite, Microbial-Sulfate-Reduction, Paleosol

This chapter is published as:

Nabhan, S., Wiedenbeck, M., Milke, R. and Heubeck, C., (2016). Biogenic overgrowth on detrital pyrite in ca. 3.2 Ga old Archean paleosols. Geology, v. 44; no. 9; p. 763-766.
http://dx.doi.org/10.1130/G38090.1

5. The Moodies nodules, a ~3.22 Ga old Earth analog for the Martian Sheepbed nodules

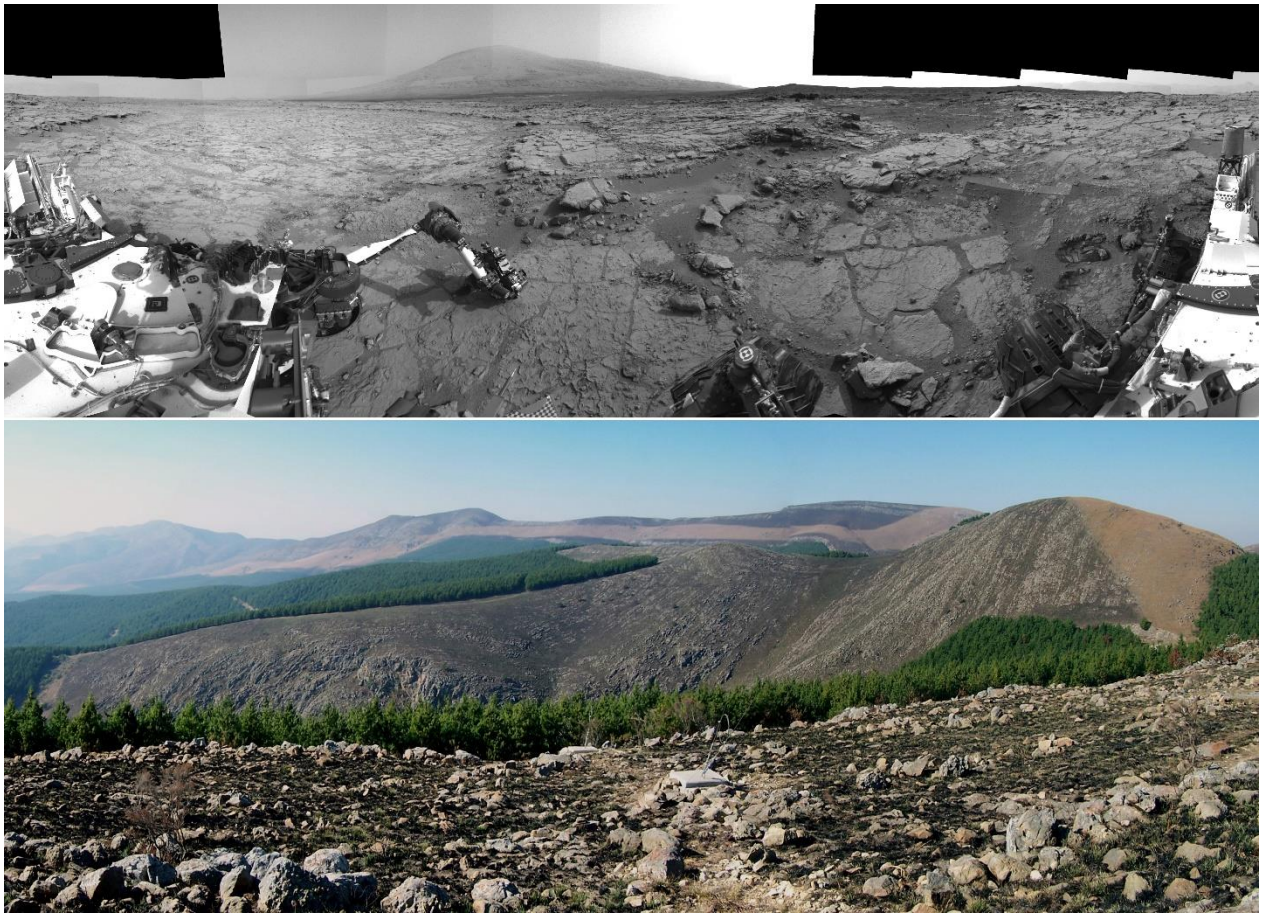

Title Figure: Outcrops of nodule-bearing strata on Mars and Earth. Top: The Sheepbed Member at Yellowknife Bay recorded by Navcam on Sol 169 as a mosaic of 40 images. Note Mount Sharp in the background. Image: NASA/JPL-Caltech. Below: Strata of the lower Moodies Group in the eastern Stolzburg Syncline of the Barberton Greenstone Belt, South Africa, mainly composed of subvertically dipping sandstone beds. The view is toward the South.

Keywords: Martian habitability, Martian nodules, Archean nodules, Earth analog

Kurzfassung

Die Sheepbed Lage der Yellowknife Bay Formation im Gale-Krater auf dem Mars enthält mehrere diagenetische Ausbildungen, von denen die Sheepbed Nodules und erhöhte Rippen als frühdiagenetisch gelten. Beide unterscheiden sich chemisch nur gering und sind auch chemisch ähnlich zum Sheepbed Tonstein. Die Nodules haben drei morphologisch unterschiedliche Ausprägungen: massiv, hohl und hohl aber gefüllt. Ähnliche Nodules sind aus den ~3,2 Ga alten Paleoböden der Moodies Gruppe des Barberton Grünstein Gürtels in Südafrika bekannt. Sie zeigen die gleichen morphologischen Details und entstanden pedogen bis frühdiagenetisch unter ähnlichen Bedingungen und zu einer ähnlichen Zeit (~3.3-3.2 Ga). Die hohlen Nodules beider Lokalitäten entstanden als zonierte Körper mit einem schwächer zementierten inneren Bereich und erscheinen im Aufschluss aufgrund präferenzieller Verwitterung des weicheren Inneren hohl.
An der pedogenen Entwicklung der Nodule haltigen Lagen waren auch biogene Prozesse beteiligt. Die Nodules der Moodies Gruppe sind deshalb ein hervorragendes Erdanalog zu den Sheepbed Nodules und verweisen auf Umgebungsbedingungen welche die Möglichkeit für außerirdisches, mikrobielles Leben auf dem Mars eröffnen.

Abstract

The Sheepbed member of the Yellowknife Bay formation in Gale crater on Mars contains a number of diagenetic features, amongst which nodules and raised ridges are considered to be of early diagenetic origin. Nodules and ridges show low chemical variety in relation to each other and to the Sheepbed mudstone. The nodules are either solid, hollow or filled, their origin is debated. Similar nodules formed approximately coevally in paleosols of the lower Moodies Group, Barberton Greenstone Belt, South Africa. They show the same morphologic details and formed pedogenic to early diagenetic under similar conditions. The hollow nodules of both locations formed as zoned bodies with a less cemented internal zone and appear hollow in outcrop due to preferential weathering of the softer material.
The pedogenic development of the nodule bearing beds involves biogenic processes. Moodies nodules are therefore an excellent Earth analog for the Sheepbed nodules on Mars and substantiate the possibility of the former existence of microbial life on Mars.

5.1. Introduction

Concretions and nodules have been described from several locations on Mars, including the hematite concretions of the Burns Formation (Grotzinger et al., 2005; Wray, 2013) and the Sheepbed nodules of the Yellowknife Bay Formation (Grotzinger et al., 2014; Stack et al., 2014). Nodules and concretions can illustrate early diagenetic, possibly even pedogenic processes. However, the involvement of life in these processes on Mars is debated. The purpose of this contribution is to illustrate the similarity of the ~3.3-3.2 Ga old Sheepbed nodules of the Sheepbed member of the Yellowknife Bay formation in Gale crater on Mars (Grant et al., 2014; Grotzinger et al., 2014; Stack et al., 2014) to the ~3.22 Ga old Moodies nodules of the Moodies Group of the Barberton Greenstone Belt in northeast South Africa and Swaziland (Lowe and Byerly, 2007; Heubeck et al., 2013; Nabhan et al., 2016a), for which a pedogenic origin involving microbial processes has been demonstrated (Nabhan et al, 2016a and b).

The Archean age of the Moodies nodules and the Hesperian age of the Sheepbed nodules places the formation of both into a time period during which Earth and Mars were more similar. At that time, Mars had a more effective surface recycling system including volcanism, aqueous environments and active valley networks (Scott and Tanaka, 1986; Greeley and Guest, 1987; Head et al., 2001; Ehlmann et al., 2011), as did Earth. Earth's Archean atmosphere had low oxygen levels and a CO_2 concentration of > 6.8 PAL (Hessler et al., 2004; Canfield, 2005; Hessler and Lowe, 2006; Sheldon, 2006; Nisbet et al., 2011) similar to proposed conditions on Mars at that time (Kieffer et al., 1992; Carr, 2006; Johnson, 2008).

5.2. Geological setting

The Mars Science Laboratory (MSL) Curiosity rover landed in August 2012 at Bradbury Landing in Gale crater (Fig. 5.1). It since investigated the sedimentary crater filling including the Yellowknife Bay Formation (Fig. 5.1) that is interpreted to be of fluvio-lacustrine origin and of Late Hesperian age (~3.3-3.2Ga; Grant et al., 2014; Grotzinger et al., 2014). The lowermost member of the Yellowknife Bay Formation, the at least 1.5 m thick Sheepbed Member, is a mudstone that contains about 30 % amorphous components, ~22 % plagioclase, ~20 % smectites and a variety of mafic minerals such as pigeonite and augite, each about 5 % or less (Vaniman et al., 2014). A number of diagenetic features within the Sheepbed member have also been identified and described (Grotzinger et al., 2014; McLennan et al., 2014; Nachon et al., 2014; Stack et al.,

2014). Besides late diagenetic calcium sulfate veins (Nachon et al., 2014), elevated ridges and nodules of solid, hollow and filled morphologies were interpreted to be of early diagenetic origin, having possibly grown prior to compaction as concretions in a fine-grained sediment (Grotzinger et al., 2014; Leveille et al., 2014; McLennan et al., 2014; Stack et al., 2014). All three types resemble nodules found within ~300 to 1000 m thick fluvial-facies sandstones of the Moodies Group in the Barberton Greenstone Belt (BGB).

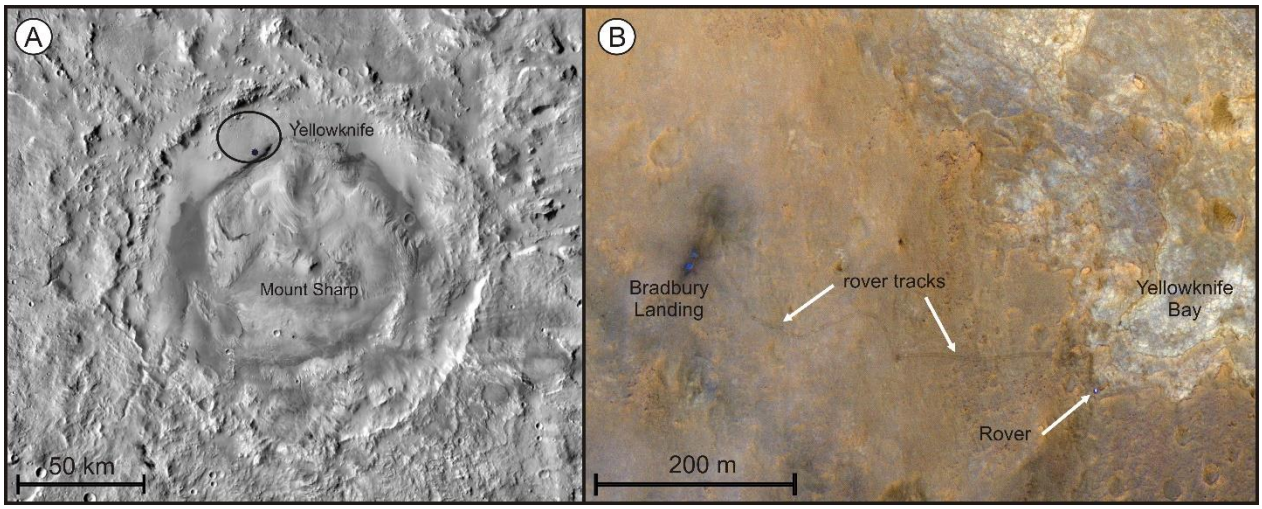

Figure 5.1: Gale crater and Yellowknife Bay on Mars. A): HiRISE mosaic of Gale crater including the landing ellipse of the Mars Science Laboratory (MSL) Curiosity rover and the location of Yellowknife Bay (black star). Image: NASA/JPL-Caltech/Arizona State University/MSSS. B): HiRISE image of the landing side (right) and Yellowknife Bay (left) Note the rover tracks from the landing side to its position on the image at the western edge of Yellowknife Bay. Image: NASA/JPL/University of Arizona (ESP_032436_1755).

The Barberton Greenstone Belt, located in northeastern South Africa and Swaziland, forms part of the Archean Kaapvaal Craton. The BGB's stratigraphic fill, the Barberton Supergroup, is subdivided from base to top into the Onverwacht (ca. 3530 – 3280 Ma; 8-10 km thick), the Fig Tree (ca. 3260 – 3225 Ma; 2-3 km thick) and the Moodies Groups (ca. 3225-3214 Ma; up to 3.7 km thick; Lowe, 1994; Lowe et al., 1999; Lowe and Byerly, 2007). The central part of the BGB experienced lower-greenschist-facies regional metamorphism while contact metamorphism is important near its margins (Diener et al., 2005; Dziggel et al., 2005).

The Moodies Group consists mainly of terrestrial to shallow-marine deposits, namely, quartz-rich sandstones, argillaceous siltstones and subordinate polymict conglomerates (Anhaeusser, 1976; Eriksson, 1979; Heubeck and Lowe, 1999; Heubeck et al., 2013). Pervasive early silicification allowed an excellent preservation of primary sedimentary and early diagenetic textures and

structures including now silicified, formerly sulfatic and calcareous nodules, evident from abundant microscopic inclusions of calcite, anhydrite and barite, and by macroscopic quartz pseudomorphs after calcite and gypsum (Nabhan et al. 2016a).

The concretions are imbedded in 300 to 1100 m thick fluvial-facies sandstones within the lower Moodies Group, which are underlain by up to 100 m thick alluvial-facies conglomerates and overlain by 400 to 1000 m thick fine-grained prodelta-facies sandy siltstones (Heubeck and Lowe, 1999; Heubeck et al., 2013; Nabhan et al., 2016a). They appear in several tectonic units of the northern BGB but are best preserved in the eastern part of the Stolzburg Syncline, where stacked, channelized, crossbedded and partly gravelly, tuffaceous sandstones include several regionally traceable beds with locally abundant to rock-forming, silicified nodules. Their facies context, texture and the chemical composition of the initial nodule forming cements support an environment in which early diagenetic, pedogenic nodules could form; their pedogenic origin in the vadose zone allows to classify these occurrences as Aridisols (Nabhan et al., 2016a).

5.3. Moodies nodules

Morphology and composition of nodules in the Moodies Group depend on their stratigraphic position within the paleosols, each approximately 30 – 60 cm thick. Nodules increase in number, size and complexity towards the top of the paleosol beds each of which consists of coarse grained, tuffaceous sandstone at the base and fines up into tuffaceous, silty, fine-grained sandstone near the top. There, nodules coalesce and build up to 20 cm thick horizons of ~2 cm thick stratiform bands intercalated with silty sandstone bands of similar thickness. Nodules have a granular surface texture, a mean size of 8 mm and are recognizable in outcrop to be either solid or hollow (Fig. 5.2).

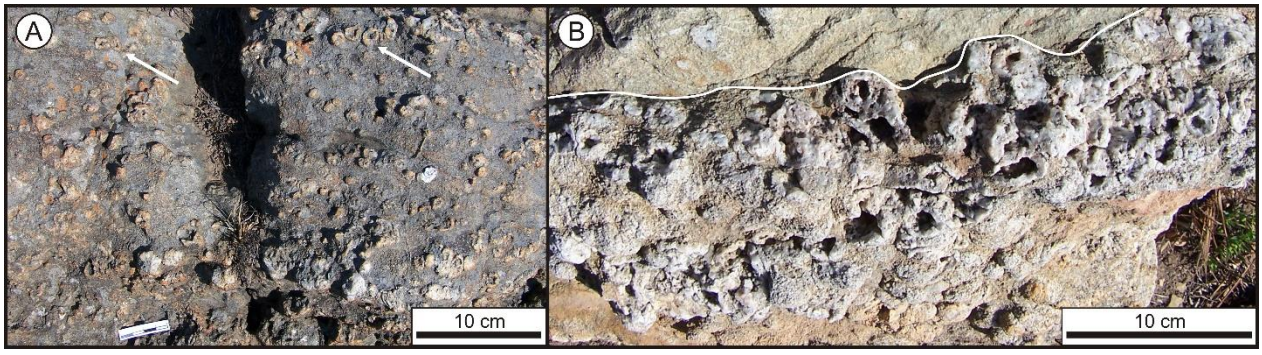

Figure 5.2: Outcrop images of silicified Moodies nodules. (A): Nodule-bearing paleosol sandstone showing numerous solid and some hollow (white arrows) nodules. (B): Upper, fine-sandy part of a nodule rich paleosol bed with coalesced nodules. The white line marks the boundary to the overlaying nodule free sandstone bed.

Thin-section and Cathodoluminescence (CL) microscopy allowed distinguishing four types of nodules (Nabhan et al., 2016a). Type I nodules are not zoned and composed of patches of poikilotopic quartz cement which overgrow and incorporate detrital grains (Fig. 5.3C). Type II nodules are composed of a quartz rim showing the same characteristics as Type I nodules, but developed inward-pointing crystals. The internal cavity is filled by fine-crystalline muscovite matrix or detrital material of the same composition as the host rock (Fig. 5.3). Type III nodules are composed of an outer quartz rim that is thinner and contains less detrital material as Type II. The inward-pointing quartz crystals are more pronounced while the internal cavity is filled by a xenomorphic late-diagenetic quartz cement. Type IV nodules are compound nodules and developed from coalescing nodules of the other types. They are large and have commonly more than one cavity, which is mostly filled by a mixture of the fine-grained muscovite, detrital grains and late-diagenetic quartz cement. Although all nodule types are mainly composed of quartz, they have been originally composed of sulfate and carbonate minerals, evident by the pseudomorphic shape of quartz crystals after gypsum and calcite and by numerous µm sized inclusions of calcite, anhydrite and barite mostly within the pseudomorphic crystals (Nabhan et al., 2016a).

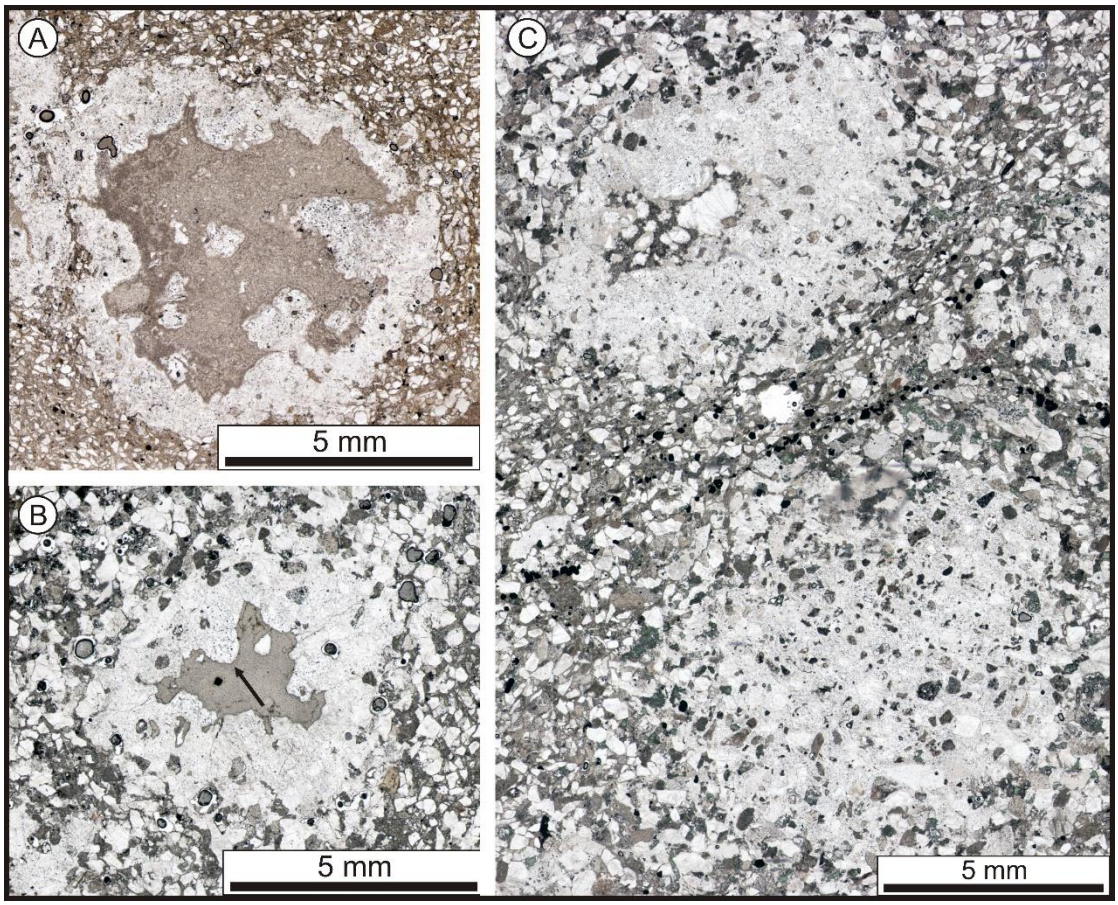

Figure 5.3: Thin section images of silicified Moodies nodules. A): Hollow nodule with a 1-2 mm thin cemented rim in surrounding an inner zone mainly composed of fine grained muscovite that roughly equals the sandstones matrix in the host rock. B): Hollow nodule composed of poikilotopic, silicified cement incorporating detrital grains. The central space is filled by a fine crystalline muscovite matrix. Note the inward growing cement (black arrow). C): The hollow nodule in the upper part of the image is also composed of poikilotopic cement but the central space is filled by the same detrital material that surrounds the nodules. The solid nodule below is composed of poikilotopic now silicified former gypsum cement and contains a high proportion of detrital grains.

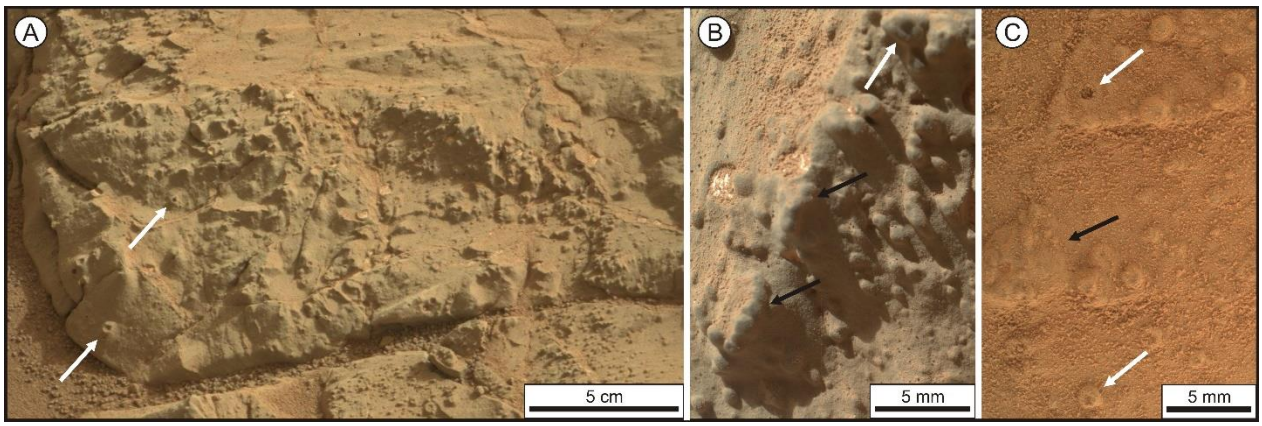

Figure 5.4: Outcrop images of the Sheepbed nodules. (A) Mastcam image 0158MR0859000000E1_DXXX taken on sol 158. The mudstone contains numerous nodules, including solid, hollow (white arrows) and filled types. Note that the filled nodules are connected to sulfate veins. (B) MAHLI image 0154MH0001740010101499C00_DXXX on sol 154. The nodules shown here coalesced and formed a distinct layer (black arrows). Note the hollow nodule to the upper right (white arrow). (C) MAHLI image 0169MH0001760020102195C01_DXXX taken on day 169. Nodules are spottier than in B but tend also to coalesce and formed an about 5 mm large body (black arrow). Note the hollow nodules (white arrows). Courtesy: NASA/JPL-Caltech.

5.4. Diagenetic features of the Sheepbed Member

The Sheepbed member contains at least three different morphological types of nodules: solid, hollow and hollow but filled (Grotzinger et al., 2014; Stack et al., 2014). They appear mostly as individual bodies but can also amalgamate to larger bodies (Fig. 5.4). Nodules are generally of spherical shape, with the hollow nodules heaving a central cavity and the hollow but filled nodules having this cavity filled by Ca-sulfate. This cavity filling sulfate also occupies fractures that run through the Sheepbed member and of which "the snake" is the largest and crosscuts the Sheepbed- and the overlaying Gillespie Lake Members (Grotzinger et al., 2014; Stack et al., 2014).

A third diagenetic feature observed in the Sheepbed Member are "raised ridges" that are interpreted as fracture filling isopachous cements and show submillimeter zoning (Grotzinger et al., 2014; Léveillé et al., 2014). The ridges are restricted to the Sheepbed Member. In areas with many ridges nodules are rare or even absent (Léveillé et al., 2014; Stack et al., 2014).

Cross cutting relations, their morphology and the chemical composition shows that the nodules and the raised ridges most likely formed contemporaneous. The fractures with their Ca-sulfate fill that also fills some of the hollow nodules formed later, after the deposition of the Gillespie Lake Member and after lithification (Grotzinger et al., 2014).

5.5. Comparison of Moodies and Sheepbed nodules

5.5.1. Host rocks composition and provenance

Both the Martian Sheepbed nodules and the Archean Moodies nodules formed about 3.2 Ga ago. The Sheepbed nodules occur within a mudstone that contains ~20 % smectite and the approximately same proportion of mafic minerals, mainly pyroxene, suggesting a basaltic provenance and deposition in a distal alluvial or proximal lacustrine setting (Grotzinger et al., 2014; Vaniman et al., 2014). The chemical composition and structure of the smectite matches that of

saponite, a byproduct of the weathering of mafic rocks (Leveille et al., 2014; Treiman et al., 2014; Vaniman et al., 2014).

The host rock of the Moodies nodules is a fine-to coarse-grained, quartz-rich (30-45 %) lithic (30-50 %) sandstone deposited in a fluvial setting (Nabhan et al., 2016a) and of mixed provenance, composed of mainly tonalitic and granitic plutons and subordinate of felsic and ultramafic volcanic material (Heubeck and Lowe, 1999; Hessler and Lowe 2006; Nabhan et al., 2016a). Moodies Group rocks experienced greenschist-grade metamorphism and contain therefore up to 30 % authigenic white mica that originate partly from metamorphic alteration of former matrix-forming clay minerals (Nabhan et al., 2016a). Clearly, the host sediment of the Moodies nodules originally contained a significant proportion of silt and clay.

5.5.2. Nodule composition

The chemical composition of the Sheepbed nodules is not fully known. The APXS and ChemCam instruments have shown a similar chemical composition for nodule-rich (Cumberland) and nodule-poor (John Klein) targets (Grotzinger et al., 2014; Stack et al., 2014; Vaniman et al., 2014); however, FeO is enriched in the presence of nodules. Magnetite (Fe_3O_4) or akaganeite ($Fe^{3+}O(OH,Cl)$) were detected by the CheMin XRD instrument in nodule-bearing targets with up to 4.4 % and 1.7 %, respectively, suggesting their role as possible nodule-forming cements (Stack et al., 2014; Vaniman et al., 2014). Akaganeite is absent in a nearby nodule-free target (Rocknest) and magnetite is a minor component with 1.5 % there (Vaniman et al., 2014).

The composition of the Moodies nodules, in contrast, is well defined; it overwhelmingly consists of quartz (Nabhan et al., 2016a). This quartz cement overgrows detrital sand grains made of quartz, lithic fragments or rarely feldspar. Detrital grains can make up to 50 vol.-% of mainly Type I-nodules (Fig. 5.3A). The cores of zoned, nodules contain additionally detrital material or a fine crystalline muscovite matrix (Fig. 5.3).

5.5.3. Nodules morphologies

Sheepbed and Moodies both contain solid and hollow nodules with a macroscopically granular surface texture (Fig. 5.2 and 5.4). Solid nodules are simple round bodies that appear to lack zoning. Hollow nodules appear in outcrops of both locations as spherical cemented bodies with a central void.

Sheepbed and Moodies nodules differ significantly in mean size. Solid and hollow Sheepbed nodules have mean diameters of 0.8 mm and 1.35 mm, respectively (Stack et al., 2014). Moodies

nodules are about 10 times larger, so that the largest Sheepbed nodules (solid: 4.11 mm; hollow: 5.4 mm, Stack et al., 2014; and 8.2 mm, Grotzinger et al., 2014) roughly equal the smallest Moodies nodules; those can reach up to 3 cm in diameter. The size of Sheepbed Member nodules decreases stratigraphically upward with smaller but more nodules in the upper part and slightly larger and fewer nodules in its lower part of the Member. Moodies nodules increase in size and number towards the top of each nodule containing paleosol bed.

5.5.4. Models of formation

Lacking microscopic data, the formation of the Sheepbed nodules is debatable, (Grotzinger et al., 2014; Stack et al., 2014). Solid nodules could either have formed as result of concentric or of pervasive cementation (Stack et al., 2014). The growth of the solid Moodies nodules resulted from precipitation of poikilotopic gypsum cement that mainly occupied pore space, thereby overgrowing sand-grains but displacing silt- and clay-sized material. This cement grew pervasive and the nodules show no concentric zoning.

Three mechanisms have been discussed for the origin of hollow Sheepbed nodules: (1) The central voids resulted from the preferential weathering of an un- or poorly cemented core (Stack et al., 2014); (2) voids represent secondary porosity from the preferential dissolution of an internal cement which differed from the exterior cement; and (3). cement formed around gas bubbles (Grotzinger et al., 2014; Stack et al., 2014).

The rims of the hollow Moodies nodules formed similar to the solid nodules as domains of poikilotopic cements incorporating detrital grains. While growing this cement displaced silt and clay that accumulated uncemented in the nodules centers. Pore waters trapped together with this fine material have been concentrated triggering the growth of inward pointing idiomorphic gypsum (Fig. 5.3B). Fine-grained muscovite formed due to greenschist metamorphic overprint of this accumulated fine material. Hollow Moodies nodules therefore originated not hollow but as zoned nodules. Their hollow expression in outcrop is due to preferential weathering of their un- or poorly cemented core.

5.5.5. Nodules formation timing

The Sheepbed nodules have been interpreted as early diagenetic (Grotzinger et al., 2014; Stack et al., 2014). Their exact time of formation depends on which formation model applies. Hollow nodules may have formed pre-compaction shortly after, almost contemporaneous to the deposition of the Sheepbed mudstone around primary gas bubbles (Grotzinger et al., 2014; Stack et al., 2014).

The interpretation of the raised ridges as subaqueous shrinkage cracks that formed contemporaneous to the nodules supports the early diagenetic origin of the nodules (Siebach et al., 2014; Stack et al., 2014). If internal cement dissolved preferentially, nodules would still be the earliest diagenetic feature but without the need of a pre-lithification formation. Preferential weathering of the internal zone, however, would hinder a precise estimate on the nodules formation time but an early diagenetic formation would still be favored based on the relations to other diagenetic features as the sulfate fractures found in the Sheepbed member (Grotzinger et al., 2014; Stack et al., 2014).

Nabhan et al. (2016) interpreted the Moodies nodules as pedogenic, based on macro- and microscopic observations (Nabhan et al., 2016a and b). Solid and hollow nodules grew contemporaneously, evident by coalesced nodules of both types. The pedogenic origin of the nodules is evident by different nodule types correlating with vertical height above channel-fill base, a function of varying groundwater levels (Chowns and Elkins 1974; Chandler, 1988; Retallack, 1991), and by reworking of (apparently resistant, possibly already silicified) nodules with chert clasts in fluvial conglomerates.

5.6. Discussion

The morphological similarity of the Martian Sheepbed nodules and the Moodies nodules on Earth is conspicuous. Both show a grainy surface and similar morphologies and arose in aqueous environments. The Sheepbed mudstone was deposited in a proximal lacustrine setting while the sandstone of the lower Moodies Group is of braided-fluvial to supratidal facies. A similarity of both environments are the recurring drying cycles presumed for the Sheepbed member (Grotzinger et al., 2014) and the Moodies sandstone, illustrated by desiccation cracks and evaporative nodule growth (Nabhan et al., 2016a). These cycles would result in fluctuating groundwater tables allowing favorable conditions for pedogenic and early diagenetic evaporative nodule growth (Retallack, 1991). Dissimilarities in grain size and host rock composition between the Sheepbed mudstone and Moodies sandstone result from differences in the depositional settings and the provenance which affected the chemical composition and morphology of the nodules. The original composition by calcite and gypsum of Moodies nodules has been replacively silicified in an early stage of diagenesis evident by fluvial reworking of nodules because the original gypsum clasts would not have withstood fluvial reworking. Silicification was restricted to the nodules only while

the surrounding sandstone contains very limited quartz cement. The high content of detrital quartz within the host rock and the additional quartz content of the felsic, magmatic, lithic fragments equilibrates the bulk mineralogical and element-chemical composition of nodule free, poor and rich areas. This equilibration is amplified by the detrital material and the muscovite matrix of the hollow nodules that equals the composition of the host rocks composition. Therefore, nodule-rich areas in the lower Moodies sandstone would differ insignificantly from nodule-poor or -free areas. Why are Moodies nodules 10 times larger? Perhaps high permeability in Moodies sandstone allowed for longer growth. The grain size difference between the Sheepbed mudstone and the Moodies sandstone caused a significantly higher porosity and permeability in the Moodies sandstones than in the Sheepbed mudstone. The chemical difference of the pore fluids and therefore the cementing minerals can also affect nodules size (Chan et al., 2000 and 2004). The upward increase in number and size of the Moodies nodules and their associated stratification is controlled by ground water variations and the upward-fining nodule-bearing horizons with the finer-grained sediment on top maybe blocking rising groundwater leading to longer lasting precipitation at this position (Francis, 1986; Retallack, 1991; Nabhan et al., 2016a). Such a mechanism could also apply to the Sheepbed member that contains smaller but more nodules in its upper part (Stack et al., 2014). The amalgamation of the Moodies nodules within the upper part of the paleosols (Fig. 4.2B) can also be seen in the Sheepbed member where nodules coalesced along a line probably following porosity fairways although the MAHLI images showing this features are not large enough to verify if this is a common feature in the Sheepbed mudstone (Fig. 5.4B and C).

Stack et al. (2014) stated that there was no straightforward analog for the formation of the hollow nodules on Earth that could be used to verify the right process. The case of a vanished precursor mineral has been found to be highly unlikely because no nodule with remains of such a mineral has been found (Grotzinger et al., 2014; Stack et al., 2014). The favored hypothesis by Grotzinger et al., (2014) and Stack et al., (2014) is the formation of gas bubbles within the mudstone around which the nodule forming cement would subsequently precipitate, and the formation of such bubbles has been described from an ephemeral pond in Ubehebe Crater in Death Valley as a result of low temperature biological activity (Bonaccorsi et al., 2015a and b). However, the observed structures appear to form only at or close to the sediments surface with the bubbles deforming the mud laminae to form the observed nodular shapes, but no structure preserving cementation around the bubbles has been described. Also, there are no findings of solid nodules as described from the Sheepbed member. The lack of nodule forming and gas bubble stabilizing cements might be

reasoned in the very early development stage of the sediment in the Ubehebe crater. Also, the need of microbial activity to initially form the bubbles in Ubehebe crater and the compression of the bubbles surrounding sediment complicates the circumstances leading to the formation of nodules as observed in the Sheepbed member. However, the formation of gas in moist, loos sediment can also occur abiogenic (Kim et al., 2013; Grotzinger et al., 2014; Vaniman et al., 2014).

The Moodies nodules formed due to pedogenic precipitation of poikilotopic sulfate cement in free pore space thereby enclosing sand sized detrital grains but displacing silt and clay. Clay mineral formation resulted from weathering of feldspar and unstable lithic fragments. Where the sediment contained a higher proportion of clay and silt this material could function as permeability barrier and triggered thereby cementation around this barrier, causing the accumulation of clay minerals in the nodules center. Already existing clay rich pockets in the sediment also triggered preferential cementation around them. The inward pointing crystals could then grow until the remaining space in the nodules center was completely filled by them and the pushed together clay minerals (Fig. 5.3). This fine material lacks not just the initial sulfate cementation but also the later silicification and is therefore less weathering resistant. Its preferential erosion causes the hollow appearance of this nodule type in outcrops (Fig. 5.2).

Clay mineral formation is also a relevant process in the Sheepbed member that contains around 20 % of saponitic smectite (Leveille et al., 2014; Treiman et al., 2014; Vaniman et al., 2014). However, it is not finally clarified if the smectites or the simultaneously developed magnetite and akaganeite is the cementing phase that forms the Sheepbed nodules (Grotzinger et al., 2014; Stack et al., 2014; Vaniman et al., 2014). The low amount of the magnetite and akaganeite in the Sheepbed mudstone might be enough to form the observed number of nodules in this low porosity rock. The early diagenetic raised ridges probably developed simultaneously with the nodules and are mainly composed of authigenic, saponitic smectites. Iron oxides could have served as nucleation sites for this clay mineral formation (Leveille et al., 2014; Vaniman et al., 2014). Therefore, iron oxides could also serve as nucleation sides for the Sheepbed nodules and similar as the clay pockets in the Moodies sandstones trigger the growth of the hollow nodules in the Sheepbed member. The formation of the Moodies nodules in a pedogenic setting (Nabhan et al., 2016a) and the necessity for such a formation process to happen in the pre-lithification stage would both favor an early diagenetic formation of the Sheepbed nodules.

The Archean, nodule-bearing Moodies paleosols contain also early diagenetic pyrite with strongly negative $\delta^{34}S_{VCDT}$ values between -20 and -25 ‰. Their close spatial relation and nearly

contemporaneous formation with the nodules shows the involvement of biogenic processes in the pedogenic development of the nodule bearing beds (Nabhan et al., 2016b). The Sheepbed nodules are imbedded in fluvio-lacustrine sediments of a similar age (~3.3 - 3.2 Ga; Grant et al., 2014) as the Moodies Group (~3.22 Ga; Heubeck et al., 2013), a time in which Earth had a CO_2-rich atmosphere. The environment in Gale crater on Mars at this time is based on findings such as the Sheepbed nodules interpreted as habitable (Grotzinger et al., 2014). Its similarity to the environment under which the Moodies paleosols formed supports the possibility that the Sheepbed member and similar deposits formed in habitable environments and are ideal targets for the search for markers of extraterrestrial microbial life.

5.7. Conclusions

Moodies nodules are a good analog for the nodules of the Sheepbed member of the Yellowknife Bay formation in Gale crater on Mars. Their solid and hollow nodules resemble those of the Sheepbed member. Their formation processes may also be similar and Moodies nodules formation processes offers an explanation why Sheepbed nodules differ little in their chemical composition from the hosting mudstone. Hollow cores result from preferential weathering of un- or poorly cemented material in the nodules core.

Sheepbed and Moodies nodules both formed at a similar time (~3.3-3.2 Ga) under similar conditions on planets that then resembled each other more than they do today. The involvement of microbial activity in the development of the Moodies nodule-bearing paleosols strengthen the case for an ancient habitable environment during the deposition of the Sheepbed mudstone and the subsequent formation of the Sheepbed nodules.

Acknowledgments

This research was funded by the German Aeronautics and Space Research Center (DLR) and the Helmholtz Alliance “Planetary Evolution and Life” under grant X/957/67147527 to C.H. The authors thank Anna Giribaldi for sample preparation and Tim Luber for assistance in the field. The MSL Science team and NASA are thanked for providing an enormous amount of data from the Curiosity Rover mission for public use.

6. Summary and conclusions

Bad outcrop conditions and metamorphic overprint left few well preserved Archean sedimentary successions to study the environmental conditions of this time. The best preserved Paleoarchean sedimentary sequences are located in the australian Pilbara- and in the Kaapvaal Craton of southern Africa. Of all sedimentary rocks evaporites and paleosols are outstanding records of physical, chemical and biological processes at the interface between rocks and the atmosphere, hydrosphere and biosphere. A well preserved combination of both is therefore the optimal target to study Archean environmental conditions.

Sulfate and carbonate nodules in the lower Moodies Group (ca. 3.22 Ga) of the Barberton Greenstone Belt formed widely in a braided-fluvial setting which interfingered with a sabkha-type coastal plain. Intensive chemical weathering, the reactive Archean atmosphere, and readily available metastable minerals, volcanic lithic fragments, and thin rhyodacitic tuffs, together with fluctuating ground water levels contributed to the rapid alteration of sandy sediment and provided ample cations in solution. Crust and concretionary growth in the sandy and gravelly sediment occurred repeatedly from concentrated brines enriched in sulfate and carbonate and was possibly supported by variable sedimentation and precipitation rates and a fluctuating groundwater level, characteristic for recent semiarid climates. Four recognized types of nodules occur at specific levels within thick sand beds and appear to reflect paleohydrological conditions. Locally abundant and rock-forming calcite and barite nodules preferentially precipitated in the upper part; less abundant gypsum-dominated nodules precipitated in the lower part of the vadose zone. The nodule bearing beds can therefore be seen as primitive Aridisols that show upper calcareous (Ack) and lower gypsiferous (Acy) horizons. The excellent preservation of their sedimentary structures may have occurred quickly, possibly even within a single drying cycle, judged from the internal textures of the nodules. The excellent preservation of the nodules, is related to the early diagenetic pseudomorphic replacement of carbonate and sulfate crystals by silica which predated burial and prevented the nodules from compaction and subsequent metamorphic alteration. The occurrence of Moodies nodule bearing beds likely represents the oldest terrestrial evaporites known to date; they form the oldest known compound paleosols.

Detrital pyrite in Moodies Group fluvial sands was partially dissolved by slightly oxidizing pore fluids during the growth of nearby pedogenic sulfates. Multi-phase authigenic growth of secondary pyrite rims occurred shortly afterwards, accompanied by early diagenetic silicification of nodules, causing sulfate release to the pore water and its subsequent microbial processing. The growth of trace-element rich, strongly 34S depleted pyrite occurred from pore fluids enriched in isotopically light HS^- and in Ni and Co derived from weathering of ultramafic rocks. Burial diagenesis and metamorphic alteration was limited mainly to the formation of a thin outer Co-rich pyrite zone.

The close spatial association and nearly simultaneous formation of pedogenic sulfate nodules and early diagenetic, isotopically light pyrite rims are consistent with microbial processing of sulfate in the moist vadose zone of Moodies Group paleosols. In such restricted Archean terrestrial environments where sulfate minerals could precipitate, microbial communities had sufficient supplies for similarly efficient fractionation as in modern environments. The S-isotope values are the lowest and oldest reported for an Archean terrestrial setting to-date, documenting that life on land dates back to at least ~3.2 Ga.

Moodies nodules also serve as an analog for the nodules of the Sheepbed Member of the Yellowknife Bay formation in Gale crater on Mars. They resemble not only the solid but also the hollow nodules of the Sheepbed Member. They are not just a morphological analog for the Sheepbed nodules, but also for their formation process. They explain why there is little chemical difference between the Sheepbed nodules and the hosting mudstone. They show that today's occurrence of hollow nodules on the surface, with a central void is a result of preferential weathering of uncemented material in contrast to their more weathering resistant, cemented rims.

The Sheepbed and the Moodies nodules both formed at a similar time (~3.3-3.2Ga) under similar conditions on planets that have had more similarities at that time than today. The S-isotopic composition of authigenic pyrite within the Moodies paleosols shows the involvement of microbial activity in its development and strengthen the case for an ancient habitable environment during the deposition of the Sheepbed mudstone and the subsequent formation of the Sheepbed nodules.

Sedimentary Archean rocks deposited in semiarid to arid, sabkha related environments, and especially paleosols developed in such somewhat evaporitic environments allowed to form gypsum in the Archean. However, even in the well preserved Archean rocks from the Pilbara and Kaapvaal Cratons it is difficult to find evidence for Archean gypsum precipitation and such evidence is mostly based on pseudomorphs and inclusions. Also the findings of this work showed, that the formed gypsum did not lasted long in the system but was early diagenetically replaced by silica

and subsequently reduced to partly form authigenic pyrite. This implies that gypsum even if it could form in places, could not survive in the Archean environment. Since both planets Earth and Mars had similar atmospheric compositions at this time the different volumes of sulfate deposits are most reasonably related to different sulfate contents in the waterbodies they evaporated from. However, the morphological similarity of the pedogenic and early diagenetic, Archean Moodies- and Martian Sheepbed nodules suggests that in places soil forming processes have been similar. The active participation of microbial communities in this processes is evident for the Moodies paleosols and opens the possibility for future speculations on microbial contributions in soil forming processes on Mars. Therefore, Martian paleosols should be a major target to search for ancient habitable environments and traces of possible former live on Mars.

References

Adams, A.E., MacKenzie, W.S. and Guilford, C., 1984. Atlas of sedimentary rocks under the microscope. Longman Group Limited, London, 103 pp.

Agangi, A., Hofmann, A. and Przybyłowicz, W., 2014. Trace element zoning of sulfides and quartz at Sheba and Fairview gold mines: Clues to Mesoarchean mineralisation in the Barberton Greenstone Belt, South Africa. Ore Geology Reviews, 56, 94-114.

Agangi, A., Hofmann, A., Rollion-Bard, C., Marin-Carbonne, J., Cavalazzi, B., Large, R. and Meffre S., 2015. Gold accumulation in the Archaean Witwatersrand Basin, South Africa — Evidence from concentrically laminated pyrite. Earth-Science Reviews, 140, 27-53.

Alonso-Zarza, A. M., Sánchez-Moya, Y., Bustillo, M. A., Sopeña, A. and Delgado, A., 2002. Silicification and dolomitization of anhydrite nodules in argillaceous terrestrial deposits: an example of meteoric-dominated diagenesis from the Triassic of central Spain. Sedimentology, 49, 303-317.

Al-Samir, M., 2015. Evaporites in Juventae Chasma – Mars, Leaching experiments and geochemical modeling. PhD. Thesis, Freie Universität Berlin, Berlin, Germany, 202 p. (unpublished).

Anhaeusser, C.R., 1966, Ulundi Syncline mapped by Van Vuuren, C.J.J., 1962. Geological map of the Eureka and Ulundi Synclines between the Havelock road and Fig Tree creek Barberton Mountain Land. Geological survey of South Africa, Pretoria.

Anhaeusser, C.R., 1969a. A comparison of pebble and fold deformation in the Nelspruit granite contact aureole Barberton Mountain Land. Transaction of the Geological Society of South Africa, 72, 49-60.

Anhaeusser, C.R., 1969b. The Stratigraphy, Structure, and Gold Mineralization of the Jamestown and Sheba Hills Areas of the Barberton Mountain Land. Ph.D. Thesis, University of the Witwatersrand, Johannesburg, South Africa, 332 p. (unpublished).

Anhaeusser, C.R., 1976. The geology of the Sheba Hills area of the Barberton Mountain Land, South Africa, with particular reference to the Eureka Syncline. Transactions of the Geological Society of South Africa, 79, 253-280.

Armstrong, R.A., Compston, W., de Wit, M.J. and Williams, I.S., 1990. The stratigraphy of the 3.5-3.2 Ga Barberton Greenstone Belt revisited: A single zircon ion microprobe study. Earth and Planetary Science Letters, 101, 90-106.

Awramik, S.M. and Buchheim, H.P., 2009. A giant, Late Archean lake system: the Meentheena Member (Tumbiana Formation; Fortescue Group), Western Australia. Precambrian Research, 174, 215-240.

Bethke, C.M. and AItaner, S.P., 1986. Layer-by-layer mechanism of smectite illitization and application to a new rate law. Clays and Clay Minerals 34, 136-145.

Bibring, J.P., Langevin, Y., Mustard, J.F., Poulet, F., Arvidson, R., Gendrin, A., Gondet, B., Mangold, N., Pinet, P. and Forget, F., 2006. Global Mineralogical and Aqueous Mars History Derived from OMEGA/Mars Express Data. Science, 312, 400-404.

Bishop, J.L., Parente, M., Weitz, C.M., Noe Dobrea, E. Z., Roach, L. H., Murchie, S.L., McGuire, P.C., McKeown, N.K., Rossi, C.M., Brown, A.J., Calvin, W.M., Milliken, R. and Mustard, J.F., 2009.

Mineralogy of Juventae Chasma: Sulfates in the light-toned mounds, mafic minerals in the bedrock, and hydrated silica and hydroxylated ferric sulfate on the plateau. Journal of Geophysical Research, Planets, 114.

Bonaccorsi, R., McKay, C. P., Baker, L., Willson, D. and Zent, A. P., 2015. Hollow nodules biosignatures in lacustrine deposits on Earth and Mars: pizza or pancakes? Astrobiology Science Conference.

Bonaccorsi, R., 2015. Hollow Nodules Gas Escape Sedimentary Structures in Lacustrine Deposits on Earth and Gale Crater. AGU Fall Meeting.

Boulter C.A. and Glover J.E., 1986. Chert with relict hopper moulds from Rocklea Dome, Pilbara Craton, Western Australia: An Archean halite-bearing evaporite. Geology, 14, 128-131.

Bridge, J.S. and Leeder, M.R., 1979. A simulation model of alluvial stratigraphy. Sedimentology, 26, 599-623.

Buick, R. and Dunlop, J.S.R., 1990. Evaporitic sediments of Early Archaean age from the Warrawoona Group, North Pole, Western Australia. Sedimentology, 37, 247-277.

Buick, R., Thronett, J.R., McNaughton, N.J., Smith, J.B., Barley, M.E. and Savage, M., 1995. Record of emergent continental crust ~3.5 billion years ago in the Pilbara craton of Australia. Nature, 375, 574-577.

Burns, R. and Fisher, D.S., 1993. Rates of oxidative weathering on the surface of Mars. Journal of Geophysical Research, Planets, 98, 3365-3372.

Byerly, G.R., Kröner, A., Lowe, D.R., Todt, W. and Walsh, M.M., 1996. Prolonged magmatism and time constraints for sediment deposition in the early Archean Barberton greenstone belt: Evidence from the Upper Onverwacht and Fig Tree groups. Precambrian Research, 78, 125-138.

Canfield, D.E., Thamdrup, B. and Fleischer, S., 1998. Isotope fractionation and sulfur metabolism by pure and enrichment cultures of elemental sulfur-disproportionating bacteria. Limnology and Oceanography, 43, 253-264.

Canfield, D.E., 2005. The early history of atmospheric oxygen: Homage to Robert M. Garrels. Annual Review of Earth and Planetary Sciences, 33, 1-36.

Carr, M.H., 2006. The Surface of Mars. Cambridge University Press, Cambridge, New York, Melbourne, Madrid, Capetown, Singapore, Sao Paulo.

Carr, M.H. and Head, J.W. III, 2010. Geological history of Mars. Earth and Planetary Science Letters, 294, 185-203.

Catling, D.C., Wood, S.E., Leovy, C., Montgomery, D.R., Greenberg, H.M., Glein, C.R. and Moore, J.M., 2006. Lighttoned layered deposits in Juventae Chasma, Mars. Icarus, 181, 26-51.

Chan, S.H., 1989. A review on solubility and polymerization of Silica. Geothermics, 18, 49-56.

Chan, M.A., Beitler, B., Parry, W.T., Ormö, J. and Komatsu, G., 2004. A possible terrestrial analogue for hematite concretions on Mars, Nature, 429, 731-734.

Chan, M.A., Parry, W.T. and Bowman, J.R., 2000. Diagenetic hematite and manganese oxides and fault related fluid flow in Jurassic sandstones, southeastern Utah. The American Association of Petroleum Geologists Bulletin, 84, 1281-1310.

Chandler, F.W., 1988. Diagenesis of sabkha-related, sulphate nodules in the Early Proterozoic Gordon Lake Formation, Ontario, Canada, Carbonates and Evaporites, 3, 75-94.

Chapman, M.G., Gudmundsson, M.T., Russell, A.J. and Hare, T.M., 2003. Possible Juventae Chasma subice volcanic eruptions and Maja Valles ice outburst floods on Mars: Implications of Mars Global Surveyor crater densities, geomorphology, and topography. Journal of Geophysical Research, 108, E10, 2-1.

Chicarro, A., Martin, P. and Trautner, R., 2004. The Mars Express Mission: An Overview. ESA Special Publication, 1240, 3-13.

Chivas, A.R., Andrew, A.S., Lyons, W.B., Bird, M.I. and Donnelly, T.H., 1991. Isotopic constraints on the origin of salts in Australian plays, 1. Sulphur. Palaeogeography, Palaeoclimatology, Palaeoecology, 84, 309-332.

Chowns, T.M. and Elkins, J.E., 1974. The origin of quartz geodes and cauliflower chert through silicification of anhydrite nodules: Journal of Sedimentology Petrology, 44, 885-903.

Christensen, P.R. and Ruff, S.W., 2004. Formation of the hematite-bearing unit in Meridiani Planum: Evidence for deposition in standing water. Journal of Geophysical Research, 109, E8, E08003.

Claire, M.W., Kasting, J.F., Domagal-Goldman, S.D., Stücken, E.E., Buick, R. and Meadows, V.S., 2014. Modeling the signature of sulfur mass-independent fractionation produced in the Archean atmosphere. Geochimica et Cosmochimica Acta, 141, 365-380.

Clark, B.C., Morris, R.V., McLennan, S.M., Gellert, R., Jolliff, B., Knoll, A.H. Squyres, S.W., Lowenstein, T.K., Ming, D.W., Tosca, N.J., Yen, A., Christensen, P.R., Gorevan, S., Brückner, J., Calvin, W., Dreibus, G., Farrand, W., Klingelhoefer, G., Waenke, H., Zipfel, J., Bell III, J.F., Grotzinger, J., McSween, H.Y. and Rieder, R., 2005. Chemistry and mineralogy of outcrops at Meridiani Planum. Earth and Planetary Science Letters, 240, 73-94.

Condie, K.C., 1997. Plate Tectonics and Crustal Evolution. Butterworth-Heinemann, Oxford.

Corcoran, P.L. and Mueller, W.U., 2004. Aggressive Archean weathering. In: Eriksson, P.G., Altermann, W., Nelson, D.R., Mueller, W.U., and Catuneanu, O. (Eds.), The Precambrian earth Tempos and Events. Developments in Precambrian Geology, 12, Elsevier, 494-504.

Crowe, S.A., Paris, G., Katsev, S., Jones, C., Kim, S.T., Zerkle, A.L., Nomosatryo, S., Fowle, D.A., Adkins, J.F., Sessions, A.L., Farquhar, J. and Canfield, D.E., 2014. Sulfate was a trace constituent of Archean seawater. Science, 346, 735-739.

Crowe, D. E. and Vaughan, R. G., 1996. Characterization and use of isotopically homogenous standards for in situ laser microprobe analysis of 34S/32S ratios. American Mineralogist, 81, 187-193.

Daval, D., Martinez, I., Corvisier, J., Findling, N., Goffé, B. and Guyot F., 2009. Carbonation of Ca-bearing silicates, the case of wollastonite: Experimental investigations and kinetic modeling. Chemical Geology, 262, 262-277.

Daval, D., Sissmann, O., Corvisier, J., Garcia, B., Martinez, I., Guyot, F. and Hellmann, R., 2010. The effect of silica coatings on the weathering rates of wollastonite (CaSiO3) and forsterite (Mg2SiO4): an apparent paradox? In: Birkle, P., Torres-Alvarado, I.S., (Eds.), Water Rock Interaction, Taylor & Francis Group, London, 713-716.

de Ronde, C.E.J. and de Wit, M.J., 1994. Tectonic history of the Barberton Greenstone Belt, South Africa: 490 million years of Archaean evolution. Tectonics, 13, 983-1005.

de Ronde, C.E.J. and Kamo, S.L., 2000. An Archean arc-arc collision event: A short-lived (ca. 3 Myr) episode, Weltevreden area, Barberton greenstone belt, South Africa. Journal of African earth Sciences, 30, 219-248.

de Ronde, C.E.J., Kamo, S., Davis, D.W., de Wit, M.J., and Spooner, E.T.C., 1991. Field, geochemical and U–Pb isotopic constraints from hypabyssal felsic intrusions within the Barberton greenstone belt, South Africa: implications for tectonics and the timing of gold mineralization. Precambrian Research, 49, 261-280.

de Wit, M.J., Furnes, H. and Robins, B., 2011. Geology and tectonostratigraphy of the Onverwacht Suite, Barberton Greenstone Belt, South Africa. Precambrian Research, 186, 28-50.

de Wit, M.J., Roering, C., Hart, R.J., Armstrong, R.A., De Ronde, C.E.J., Green, R.W.E., Tredoux, M., Peberdy, E. and Hart, R.A., 1992. Formation of an Archaean continent. Nature, 357, 553-562.

Diener, J.F.A., Stevens, G., Kisters, A.F.M. and Poujol, M., 2005. Metamorphism and exhumation of the basal parts of the Barberton greenstone belt, South Africa: constraining the rates of Mesoarchaean tectonism. Precambrian Research, 143, 87-112.

Ding, T., Valkiers, S., Kipphardt, H., De Bièvre, P., Taylor, P.D.P., Gonfiantini, R. and Krouse, R., 2001. Calibrated sulfur isotope abundance ratios of three IAEA sulfur isotope reference materials and V-CDT with a reassessment of the atomic weight of sulphur. Geochimica et Cosmochimica Acta, 65, 2433-2437.

Dziggel, A., Armstrong, R.A., Stevens, G. and Nasdala, L., 2005. Growth of zircon and titanite during metamorphism in the granitoid-gneiss terrane south of the Barberton greenstone belt, South Africa. Mineralogical Magazine, 69, 1019-1036.

Eckardt, F.D. and Spiro, B., 1999. The origin of sulphur in gypsum and dissolved sulphate in the Central Namib Desert, Namibia. Sedimentary Geology, 123, 255-273.

Ehlmann, B.L., Mustard, J.F., Murchie, S.L., Bibring, J.-P., Meunier, A. and Fraeman, A.A., 2011. Subsurface water and clay mineral formation during the early history of Mars. Nature, 479, 53-60.

England, G.L., Rasmussen, B., Krapez, B. and Groves, D.I., 2002. Palaeoenvironmental significance of rounded pyrite in siliciclastic sequences of the Late Archaean Witwatersrand Basin: oxygen-deficient atmosphere or hydrothermal alteration? Sedimentology, 49, 1133-1156.

Eriksson, K.A., 1977. Tidal deposits from the Archaean Moodies Group, Barberton Mountain Land, South Africa. Sedimentary Geology, 18, 257-281.

Eriksson, K.A., 1978. Alluvial and destructive beach facies from the Archaean Moodies Group, Barberton Mountain Land, South Africa and Swaziland. In: Miall, A.D. (Ed.), Fluvial Sedimentology, 5. Canadian Society of Petroleum Geologists Memoir, Calgary, 287-311.

Eriksson, K.A., 1979. Marginal marine depositional processes from the Archaean Moodies Group, Barberton Mountain Land, South Africa: evidence and significance. Precambrian Research, 8, 153-182.

Eriksson, K.A., 1980. Transitional sedimentation styles in the Fig Tree and Moodies Group, Barberton Mountain Land, South Africa: evidence favoring an Atlantic or Japan sea-type Archaean continental margin. Precambrian Research, 12, 141-160.

Eriksson, K.A. and Simpson, E.L., 2000. Quantifying the oldest tidal record: The 3.2 Ga Moodies Group, Barberton Greenstone Belt, South Africa. Geology, 28, 831-834.

Eriksson K.A., Simpson E.L., Master S. and Henry G., 2005. Neoarchean (c. 2.58 Ga) halite casts: implications for palaeoceanic chemistry. Journal of the Geological Society, 162, 789-799.

Eriksson, K.A., Simpson, E.L. and Mueller, W., 2006. An unusual fluvial to tidal transition in the meso-Archaean Moodies Group, South Africa: a response to high tidal range and active tectonics. Sedimentary Geology, 190, 13-24.

Eriksson, P.G., Condie, K.C., Tirsgaard, H., Mueller, W.U., Altermann, W., Miall, A.D., Aspler, L.B., Catuneanu, O. and Chiarenzelli, J.R., 1998. Precambrian clastic sedimentation systems. Sedimentary Geology, 120, 5-53.

Eriksson, P.G., Altermann, W., Nelson, D.R., Mueller, W.U. and Catuneanu, O., (Eds.), 2004. The Precambrian Earth: Tempos and Events. Developments in Precambrian Geology, 12. Elsevier, xxiv + 941 p.

Farquhar, J., Bao, H. and Thiemans, M., 2000. Atmospheric influence of Earth's earliest sulfur cycle. Science, 289, 756-758.

Farquhar, J., Savarino, J., Airieau, S. and Thiemens, M.H., 2001. Observation of wavelength-sensitive mass-independent sulfur isotope effects during SO_2 photolysis: Implications for the early atmosphere. Journal of Geophysical Research, 106, 32829-32839.

Ferrar, T. and Heubeck, C., 2013. Barberton Makhonjwa Geotrail, geosites and view points. Hamilton-Fynch, Batobic, xii + 41 p.

Flinn, E.A., Reid, G.C. and Csanady, G., 1977. Scientific results of the Viking Project, American Geophysical Union, Washington, DC, USA, 82, 735 p.

Francis, J.E. 1986. The calcareous paleosols of the basal Purbeck Formation (Upper Jurassic). Southern England. In: Wright, V.P. (Eds.), Paleosols: Their Recognition and Interpretation, Blackwells, Oxford, 315 p.

Gamper, A., Heubeck, C., Demske, D. and Hoehse, M., 2012. Composition and microfacies of Archean microbial mats (Moodies Group, Ca. 3.22 Ga, South Africa). In: Noffke, N., and Chafetz, H. (Eds.), Microbial Mats in Siliciclastic Depositional Systems through Time: SEPM (Society for Sedimentary Geology), Tulsa, OK. Special Publications, 101, 65-74.

Gandin A., Wright D.T. and Melezhik V., 2005. Vanished evaporites and carbonate formation in the Neoarchaean Kogelbeen and Gamohaan formations of the Campbellrand Subgroup, South Africa. Journal of African Earth Sciences, 41, 1-23.

Gargaud, M., Barbier, B., Martin, H. and Reisse, J. (Eds.), 2005. Lectures in Astrobiology. Advances in Astrobiology and Biogeophysics, 1, XXVI, 793 p.

Gay, N.C., 1969. The analysis of strain in the Barberton Mountain Land, eastern Transvaal, using deformed pebbles. Geology, 77, 377-396.

Gendrin, A., Mangold, N., Bibring, J.P., Langevin, Y., Gondet, B., Poulet, F., Bonello, G., Quantin, C., Mustard, J., Arvidson, R. and LeMouélic, S., 2005. Sulfates in Martian Layered Terrains: The OMEGA/Mars Express View. Science, 307, 1587-1591.

Ghosh, R. and Bhattacherjee, S., 2013. A Review Study on Precipitated Silica and Activated Carbon from Rice Husk. Chemical Engineering and Process Technology, 4, 1-7.

Golombek, M.P., Cook, R.A., Economou, T., Folkner, W.M., Haldemann, A.F.C., Kallemeyn, P.H., Knudsen, J.M., Manning, R.M., Moore, H.J., Parker, T.J., Rieder, R., Schofield, J.T., Smith, P.H. and Vaughan, R.M., 1997. Overview of the Mars Pathfinder Mission and Assessment of Landing Site Predictions, Science, 278, 1743-1748.

Goodall, T. M., North, C.P. and Glennie, W., 2000. Surface and subsurface sedimentary structures produced by salt crusts. Sedimentology, 47, 99-118.

Grandstaff, D.E., Edelman, M.J., Foster, R.W., Zbinden, E. and Kimberley, M.M., 1986. Chemistry and mineralogy of Precambrian paleosols at the base of the Dominion and Pongola Groups. Precambrian Research, 32, 97-131.

Grant, J. A., Wilson, S. A., Mangold, N. and Calef III, F., and Grotzinger, J. P., 2014. The timing of alluvial activity in Gale crater, Mars. Geophysical Research Letters, 41, 1142-1148.

Grassineau, N.V., Nisbet, E.G., Bickle, M.J., Fowler, C.M.R., Lowry, D., Mattey, D.P., Abell, P. and Martin, A., 2001. Antiquity of the biological sulphur cycle: evidence from sulphur and carbon isotopes in 2700 million year old rocks of the Belingwe belt, Zimbabwe. Proc. R. Soc. London, 268, 113-119.

Greeley, R. and Guest, J.E., 1987. Geological Map of the eastern equatorial region of Mars I-1802-B. U.S. Geological Survey, Flagstaff, AZ, USA.

Grimm, W.D., 1962. Idiomorphe Quarze als Leitminerale für salinare Fazies. Erdöl und Kohle, 15, 880-887.

Grosch, E.G. and McLoughlin, N., 2013. Paleoarchean sulfur cycle and biogeochemical surface conditions on the early Earth, Barberton, South Africa. Earth and Planetary Science Letters, 377-378, 142-154.

Grotzinger J.P. and Kasting J.F., 1993. New Constrains on Precambrian Ocean Composition. Geology, 101, 235-243.

Grotzinger, J.P., Arvidson, R.E., Bell III, J.F., Calvin, W., Clark, B.C., Fike, D.A., Golombek, M., Greeley, R., Haldemann, A., Herkenhoff, K.E., Jolliff, B.L., Knoll, A.H., Malin, M., McLennan, S.M., Parker, T., Soderblom, L., Sohl-Dickstein, J.N., Squyres, S.W., Tosca, N.J. and Watters, W.A., 2005. Stratigraphy and sedimentology of a dry to wet eolian depositional system, Burns formation, Meridiani Planum, Mars. Earth and Planetary Science Letters, 240, 11-72.

Grotzinger, J.P., Sumner, D.Y., Kah, L.C., Stack, K., Gupta, S., Edgar, L., Rubin, D., Lewis, K., Schieber, J., Mangold, N., Milliken, R., Conrad, P.G., DesMarais, D., Farmer, J., Siebach, K., Calef III, F., Hurowitz, J., McLennan, S.M., Ming, D., Vaniman, D., Crisp, J., Vasavada, A., Edgett, K.S., Malin, M., Blake, D., Gellert, R., Mahaffy, P., Wiens, R.C., Maurice, S. Grant, J.A., Wilson, S., Anderson, R.C., Beegle, L., Arvidson, R., Hallet, B., Sletten, R.S., Rice, M., Bell III, J., Griffes, J., Ehlmann, B., Anderson, R.B., Bristow, T.F., Dietrich, W.E., Dromart, G., Eigenbrode, J., Fraeman, A., Hardgrove, C., Herkenhoff, K., Jandura, L., Kocurek, G., Lee, S., Leshin, L.A., Leveille, R., Limonadi, D., Maki, J., McCloskey, S., Meyer, M., Minitti, M., Newsom, H., Oehler, D., Okon, A.,

Palucis, M., Parker, T., Rowland, S., Schmidt, M., Squyres, S., Steele, A., Stolper, E., Summons, R., Treiman, A., Williams, R., Yingst, A. and MSL Science Team, 2014. A habitable fluvio-lacustrine environment at Yellowknife Bay, Gale crater, Mars. Science, 343, 1242777.

Grotzinger J.P. and Kasting J.F., 1993. New Constrains on Precambrian Ocean Composition. Geology, 101, 235-243.

Götze, J. and Möckel, R., (Eds.), 2012. Quartz: Deposits, Mineralogy and Analytics. Springer Geology, Berlin Heidelberg, 360 p.

Götze, J., Pan, Y., Stevens-Kalceff, M., Kempe, U. and Müller, A., 2015. Origin and significance of the yellow cathodoluminescence (CL) of quartz. American Mineralogist, 100, 1469-1482.

Götze, J., Plötze, M. and Habermann, D., 2001. Origin, spectral characteristics and practical applications of the cathodoluminescence (CL) of quartz – a review. Mineralogy and Petrology, 71, 225-250.

Habicht, K.S., Gade, M., Thamdrup, B., Berg, P. and Canfield, D.E., 2002. Calibration of Sulfate Levels in the Archean Ocean. Science, 298, 2372-2374.

Halevy, I. and Head, J.W., 2014. Episodic warming of early Mars by punctuated volcanism. Nature Geoscience, 7, 865-868.

Hardie, L.A., 2003. Secular variations in Precambrian seawater chemistry and the timing of Precambrian aragonite seas and calcite sea. Geology, 31, 785-788.

Harnmeijer J.P., 2010. Squeezing Blood from a Stone: Inference into the Life and Depositional Environments. Ph.D. Thesis, University of Washington, Washington.

Hartmann, W.K. and Neukum, G., 2001. Cratering chronology and the evolution of Mars. Space Science Reviews, 96, 165-194.

Head, J.W., Greeley, R., Golombek, M.P., Hartmann, W.K., Hauber, E., Jaumann, R., Masson, P., Neukum, G., Nyquist, L.E. and Carr, M.H., 2001. Geological Processes and Evolution. Space Science Reviews, 96, 263-292.

Heinrichs, T.K. and Reimer, T.O., 1977. A sedimentary baryte deposit from the Archean Fig Tree Group of the Barberton Mountain Land (South Africa). Economic Geology, 72, 1426-1441.

Hessler, A.M., Lowe, D.R., Jones, R.L., and Bird, D.K., 2004. A lower limit for atmospheric carbon dioxide levels 3.2 billion years ago. Nature 428, 736-738.

Hessler, A.M. and Lowe, D.R., 2006. Weathering and sediment generation in the Archean: An integrated study of the evolution of siliciclastic sedimentary rocks of the 3.2 Ga Moodies Group, Barberton Greenstone Belt, South Africa. Precambrian Research, 151, 185-210.

Heubeck, C., 2009. An early ecosystem of Archean tidal microbial mats (Moodies Group, South Africa, ca. 3.2 Ga). Geology, 37, 931-934.

Heubeck, C., Bläsing, S., Drabon, N., Grund. M., Homann, M. and Nabhan, S., 2016. Geological constrains on Archean (3.22 Ga) costal-zone processes from the Dycedale Syncline, Barberton Greenstone Belt. South African Journal of Geology (submitted after revision).

Heubeck, C., Engelhardt, J., Byerly, G.R., Zeh, A., Selld, B., Luber, T. and Lowe, D.R., 2013. Timing of deposition and deformation of the Moodies Group (Barberton Greenstone Belt, South Africa): Very-high-resolution of Archaean surface processes. Precambrian Research, 231, 236-262.

Heubeck, C., Köhler, I., Homann, M. and Drabon, N., 2015, Raman Spectroscopy of biomats from the Moodies Group (Barberton Greenstone Belt, South Africa, 3.22 Ga): Habitability in the Universe: From the Early Earth to Exoplanets, 22-27 March 2015, Porto, Portugal (conference abstract).

Heubeck, C. and Lowe, D.R., 1994a. Depositional and tectonic setting of the Archaean Moodies Group, Barberton Greenstone Belt, South Africa. Precambrian Research, 68, 257-290.

Heubeck, C. and Lowe, D.R., 1994b. Late syndepositional deformation and detachment tectonics in the Barberton Greenstone Belt, South Africa. Tectonics, 13, 1514-1536.

Heubeck, C. and Lowe, D.R., 1999. Sedimentary petrology and provenance of the Archean Moodies Group, Barberton Greenstone Belt, South Africa. In: Lowe, D.R., Byerly, G.R. (Eds.), Geologic Evolution of the Barberton Greenstone Belt, South Africa. Geological Society of America Special Paper. Boulder, Colorado, 329, 259-286.

Hofmann, A., 2005. The geochemistry of sedimentary rocks from the Fig Tree Group, Barberton greenstone belt: Implications for tectonic, hydrothermal and surface processes during mid-Archaean times. Precambrian Research, 143, 23-49.

Holland, H.D., Feakes, C.R. and Zbinden, E.A., 1989. The Flin Flon paleosol and the composition of the atmosphere 1.83 By.B.P. American Journal of Science, 289, 362-389.

Homann, M., Heubeck, C., Airo, A. and Tice, M., 2015. Morphological adaptations of 3.22 Ga-old tufted microbial mats to Archean coastal habitats (Moodies Group, Barberton Greenstone Belt, South Africa). Precambrian Research, 266, 47-64.

Howarth, R.W., 1979. Pyrite: Its Rapid Formation in a Salt Marsh and Its Importance in Ecosystem Metabolism: Science, 203, 49-51.

Huston, D.L. and Logan, G.A., 2004. Barite, BIFs and bugs: evidence for the evolution of the Earth's early hydrosphere. Earth and Planetary Science Letters, 220, 41-55.

Jewell, P.W., 2000. Bedded Barite in the geologic record. SEPM Special Publication, 66, 147-161.

Johnson, S.S., Mischna, M.A., Grove, T.L. and Zuber, M.T., 2008. Sulfur-induced greenhouse warming on early Mars. Journal of Geophysical Research, Planets, 113, 1-15.

Kamo, S.L. and Davis, D.W., 1994. Reassessment of Archaean crustal development in the Barberton Mountain Land, South Africa. Tectonics, 13, 167-192.

Kasting, J.F., 1990. Bolide impacts and the oxidation state of carbon in the earth's early atmosphere: Origins of Life, 20, 199-231.

Kempe S. and Degens E.T., 1985. An early soda ocean? Chemical Geology, 53, 95-108.

Kendall, A.C., 1992. Evaporites, Facies Models: Responses to sealevel change. Geological Association of Canada, 375-409.

Kieffer, H.H., Jakosky, B.M. and Snyder, C.W., 1992. The Planet Mars: From Antiquity to the Present. In: Kieffer, H.H., Jakosky B.M., Snyder, C.W., and Matthews, M. (Eds.), Mars. The University of Arizona Press, Tucson, 1-33.

King, P.L. and McSween, H.Y., 2005. Effects of H_2O, pH, and oxidation state on the stability of Fe minerals on Mars. Journal of Geophysical Research, 110, 1-15.

Kisters, A.F.M. and Anhaeusser, C.R., 1995. Emplacement features of Archaean TTG plutons along the southern margin of the Barberton greenstone belt, South Africa. Precambrian Research, 75, 1-15.

Kim, J.D., Yee, N., Nanda, V., Falkowski, P.G., 2013. Anoxic photochemical oxidation of siderite generates molecular hydrogen and iron oxides. Proc. Natl. Acad. Sci. U.S.A., 110, 10073-10077.

Klingelhöfer, G., Morris, R.V., Bernhardt, B., Schröder, C., Rodionov, D.S., de Souza, P.A., Yen, A., Gellert, R., Evlanov, E.N., Zubkov, B., Foh, J., Bonnes, U., Kankeleit, E., Gütlich, P., Ming, D.W., Renz, F., Wdowiak, T., Squyres, S.W. and Arvidson, R.E., 2004. Jarosite and Hematite at Meridiani Planum from Opportunity's Mössbauer Spectrometer. Science, 306, 1740-1745.

Knauth, L.P., 2005. Temperature and salinity history of the Precambrian ocean: implications for the course of microbial evolution. Palaeogeography, Palaeoclimatology, Palaeoecology, 219, 53-69.

Knauth, L.P. and Lowe, D.R., 2003. High Archean climatic temperature inferred from oxygen isotope geochemistry of cherts in the 3.5 Ga Swaziland Supergroup, South Africa. Geological Society of America Bulletin, 115, 566-580.

Kraus, M.J., 1999. Paleosols in clastic sedimentary rocks: their geologic applications. Earth-Science Reviews, 47, 41-70.

Kraus, M.J. and Aslan, A., 1993. Eocene hydromorphic paleosols: significance for interpreting ancient floodplain processes. Journal of Sedimentary Petrology, 63, 453-463.

Kraus, M.J. and Gwinn, B., 1997. Facies and facies architecture of Paleogene floodplain deposits, Willwood Formation, Bighorn Basin, Wyoming, USA. Sedimentary Geology, 114, 33-54.

Kröner, A., Byerly, G.R. and Lowe, D.R., 1991. Chronology of early Archaean granite-greenstone evolution in the Barberton Mountain Land, South Africa, based on precise dating by single zircon evaporation. Earth and Planetary Science Letters, 103, 41-54.

Kröner, A. and Todt, W., 1988. Single zircon dating constraining the maximum age of the Barberton greenstone belt, southern Africa. Journal of Geophysical Research, 93, 15329-15337.

Lamb, S.H., 1984. Structures and Sedimentology on the Eastern Margin of the Archaean Barberton Greenstone Belt, Northwest Swaziland. PhD Thesis, University of Cambridge, 178 p. (unpublished).

Layer, P.W., Kröner, A. and McWilliams, M., 1996. An Archaean Geomagnetic Reversal in the Kaap Valley Pluton, South Africa. Science, 273, 943-946.

Léveillé, R.J., Bridges, J., Wiens, R.C., Mangold, N., Cousin, A., Lanza, N., Forni, O., Ollila, A., Grotzinger, J., Clegg, S., Siebach, K., Berger, G., Clark, B., Fabre, C., Anderson, R., Gasnault, O., Blaney, D., Deflores, L., Leshin, L., Maurice, S., and Newsom H., 2014. Chemistry of fracture-filling raised ridges in Yellowknife Bay, Gale Crater: Window into past aqueous activity and habitability on Mars, Journal of Geophysical Research, Planets, 119, 2398-2415.

Lowe, D.R., 1994. Accretionary history of the Archaean Barberton greenstone belt (3.55–3.22 Ga), Southern Africa. Geology, 22, 1099-1102.

Lowe, D.R., Byerly, G.R. and Heubeck, C., 1999. Structural divisions and development of the west-central part of the Barberton Greenstone Belt. In: Lowe, D.R., Byerly, G.R. (Eds.), Geologic Evolution of the Barberton Greenstone Belt, South Africa. Geological Society of America Special Paper, Boulder, Colorado, 329, 37-82.

Lowe, D.R. and Byerly, G.R., 2007. An overview of the geology of the Barberton Greenstone Belt and vicinity: implications for early crustal development. In: van Kranendonk, M.J., Smithies, R.H., Bennett, V.H. (Eds.), Earth's Oldest Rocks. Elsevier (Developments in Precambrian Geology), Amsterdam, 15, 481-526.

Lowe, D.R. and Worrell, G.F., 1999. Sedimentology, mineralogy, and implications of silicified evaporates in the Kromberg Formation, Barberton Greenstone Belt, South Africa. In: Lowe D.R. and G.R. Byerly (Eds.), Geologic evolution of the Barberton Greenstone Belt, South Africa. Boulder, Colorado, Geological Society of America Special Paper, 329, 167-187.

Macfarlane, A.W., Danielson, A. and Holland, H.D., 1994. Geology and major and trace element chemistry of the late Archean weathering profiles in the Fortescue Group, Western Australia: implications for atmospheric pO2. Precambrian Research, 65, 297-317.

Mack, G.H., James, W.C. and Monger, H.C., 1993. Classification of paleosols. Geological Society of America Bulletin, 105, 129-136.

Malin, M.C. and Edgett, K.S., 2000. Sedimentary rocks of early Mars. Science, 290, 1927-1937.

McBride, E.F., 1963. A classification of common sandstones. Journal of Sedimentary Petrology, 33, 664-669.

McLennan, S.M., Bell III, J.F., Calvin, W.M., Christensen, P.R., Clark, B.C., de Souza, P.A., Farmer, J., Farrand, W.H., Fike, D.A., Gellert, R., Ghosh, A., Glotch, T.D., Grotzinger, J.P., Hahn, B., Herkenhoff, K.E., Hurowitz, J.A., Johnson, J.R., Johnson, S.S., Jolliff, B., Klingelhöfer, G., Knoll, A.H., Learner, Z., Malin, M.C., McSween Jr, H.Y., Pocock, J., Ruff, S.W., Soderblom, L.A., Squyres, S.W., Tosca, N.J., Watters, W.A., Wyatt, M.B. and Yen, A., 2005. Provenance and diagenesis of the evaporite-bearing Burns formation, Meridiani Planum, Mars. Earth and Planetary Science Letters, 240, 95-121.

McLennan, S. M., Anderson, R.B., Bell III, J.F., Bridges, J.C., Calef III, F., Campbell, J.L., Clark, B.C., Clegg, S., Conrad, P., Cousin, A., Des Marais, D.J., Dromart, G., Dyar, M.D., Edgar, L.A., Ehlmann, B.L., Fabre, C., Forni, O., Gasnault, O., Gellert, R., Gordon, S., Grant, J.A., Grotzinger, J.P., Gupta, S., Herkenhoff, K.E., Hurowitz, J.A., King, P.L., Le Mouélic, S., Leshin, L.A., Léveillé, R., Lewis, K.W., Mangold, N., Maurice, S., Ming, D.W., Morris, R.V., Nachon, M., Newsom, H.E., Ollila, A.M., Perrett, G.M., Rice, M.S., Schmidt, M.E., Schwenzer, S.P., Stack, K., Stolper, E.M., Sumner, D.Y., Treiman, A.H., VanBommel, S., Vaniman, D.T., Vasavada, A., Wiens, R.C., Yingst, R.A., and MSL Science Team, 2014. Elemental geochemistry of sedimentary rocks at Yellowknife Bay, Gale crater, Mars. Science, 343, 1244734.

Merinero, R., Lunar, R., Martinez-Frias, J., Somoza, L., and Diaz-del-Rio, V., 2008. Iron oxyhydroxide and sulphide mineralization in hydrocarbon seep-related carbonate submarine chimneys, Gulf of Cadiz (SW Iberian Peninsula): Marine and Petroleum Geology, 25, 706-713.

Meyer, F.M., Robb, L.J., Oberthür, T., Saager, R. and Stupp, H.D., 1990. Cobalt, nickel, and gold in pyrite from primary gold deposits and Witwatersrand reefs. South African Journal of Geology, 93, 70-82.

Mojzsis, S.J., Coath, C.D., Greenwood, J.P., McKeegan, K.D. and Harrison, T.M., 2003. Mass-independent isotope effects in Archean (2.5 to 3.8 Ga) sedimentary sulfides determined by ion microprobe analysis. Geochimica et Cosmochimica Acta, 67, 1635-1658.

Montgomery, D.R., and A. Gillespie 2005. Formation of Martian outflow channels by catastrophic dewatering of evaporite deposits. Geology, 33, 625-628.

Morris, R.V., Ruff, S.W., Gellert, R., Ming, D.W., Arvidson, R.E., Clark, B.C., Golden, D.C., Siebach, K., Klingelhöfer, G., Schröder, C., Fleischer, I., Yen, A.S. and Squyres, S.W., 2010. Identification of Carbonate-Rich Outcrops on Mars by the Spirit Rover. Science, 329, 421-424.

Mueller, W. and Dimroth, E., 1987. A terrestrial-shallow marine transition in the Archean opemisca group east of Chapais, Quebec. Precambrian Research, 37, 29-55.

Nabhan, S., Luber, T., Scheffler, F. and Heubeck, C., 2016a. Climatic and geochemical implications of Archean pedogenic gypsum of the Moodies Group (~3.2 Ga), Barberton Greenstone Belt, South Africa. Precambrian Research, 275, 119-134.

Nabhan, S., Wiedenbeck, M., Milke, R. and Heubeck, C., 2016b. Biogenic overgrowth on detrital pyrite in ~3.2 Ga old Archean paleosols. Geology, (accepted).

Nachon, M., Clegg, S.M., Mangold, N., Schröder, S., Kah, L.C., Dromart, G., Ollila, A., Johnson, J.R., Oehler, D.Z., Bridges, J.C., Le Mouélic, S., Forni, O., Wiens, RC., Anderson, R.B., Blaney, D.L., Bell III, J.F., Clark, B., Cousin, A., Dyar, M.D., Ehlmann, B., Fabre, C., Gasnault, O., Grotzinger, J., Lasue, J., Lewin, E., Léveillé, R., McLennan, S., Maurice, S., Meslin, P.-Y., Rapin, W., Rice, M., Squyres, S.W., Stack, K., Sumner, D.Y., Vaniman, D. and Wellington, D., 2014. Calcium sulfate veins characterized by ChemCam/Curiosity at Gale crater, Mars. Journal of Geophysical Research, Planets, 119, 1991-2016.

Neukum, G., Jaumann, R., Basilevsky, A.T. Dumke, A., Van Gasselt, S., Giese, B., Hauber, E., Head III, J.W., Heipke, C., Hoekzema, N., Hoffmann, H., Greeley, R., Gwinner, K., Kirk, R., Markiewicz, W., McCord, T.B., Michael, G., Muller, J.-P., Murray, J.B., Oberst, J., Pinet, P., Pischel, R., Roatsch, T., Scholten, F. and Willner, K., the HRSC Co-Investigator Team and HRSC Associates, 2009. HRSC: High resolution stereo camera. In: Mars Express: The scientific investigations. ESA, SP-1291, 15-73.

Nisbet, E. and Fowler, C.M.R., 2011. The evolution of the atmosphere in the Archaean and early Proterozoic. Chinese Science Bulletin, 56, 4-13.

Noel, A., Bishop, J., Al-Samir, M., Gross, C., Flahaut, J., McGuire, P.C., Weitz, C.M., Seelos, F. and Murchie, S., 2015. Mineralogy, morphology and stratigraphy of the light-toned interior layered deposits at Juventae Chasma. Icarus, 251, 315-331.

Noffke, N., Eriksson, K.A., Hazen, R.M. and Simpson, E.L., 2006. A new window into Early Archean life: microbial mats in Earth's oldest siliciclastic tidal deposits (3.2 Ga Moodies Group, South Africa). Geology, 34, 253-256.

Ohmoto, H., Kakegawa, T., and Lowe, D.R., 1993. 3.4-billion-year old biogenic pyrites from Barberton, South Africa: sulfur isotope evidence: Science, 262, 555-557.

Ostwald, J., and England, B.M., 1979. The relationship between euhedral and framboidal pyrite in base-metal sulfide ores: Mineralogical Magazine, 43, 297-300.

Otto, A., Dziggel, A., Kisters, A. and Meyer, F., 2007. The New Consort Gold Mine, Barberton greenstone belt, South Africa: orogenic goldmineralization in a condensed metamorphic profile. Miner. Deposita, 42, 715-735.

Paris, G., Adkins, J.F., Sessions, A.L., Webb, S.M. and Fischer, W.W., 2014. Neoarchean carbonate-associated sulfate records positive Δ33S anomalies. Science, 346, 739-741.

Pavlov, A.A. and Kasting, J.F., 2002. Mass-independent fractionation of sulfur isotopes in Archean sediments: Strong evidence for an anoxic Archean atmosphere. Astrobiology 2, 27-41.

Philippot, P., van Zuilen, M. and Rollion-Bard, C., 2012. Variations in atmospheric sulphur chemistry on early Earth linked to volcanic activity. Nature Geoscience, 5, 668-674.

Pufahl P.K. and Hiatt E.E., 2012. Oxygenation of the Earth's atmosphere-ocean system: A review of physical and chemical sedimentologic responses. Marine and Petroleum Geology, 32, 1-20.

Reijers, T. J. A. and Hsü, K. J. (Eds), 1986. Manual of Carbonate Sedimentology. A Lexicographical Approach. London, Orlando, San Diego, New York, Austin, Montreal, Sydney, Tokyo, Toronto: Academic Press. xix + 301 p.

Reimer, T.O., 1967. Die Stolzburg Synklinale, Beitrag zur Geologie des Barberton-Berglandes (Transvaal - Südafrika): Diplomarbeit, unpublished, Univ. Frankfurt.

Reimer, T.O., 1980. Archean sedimentary barite deposits of the Swaziland Supergroup (Barberton Mountain Land, South Africa). Precambrian Research, 12, 393-410.

Reimer, T.O., 1986. Isotopic constraints on the derivation of sulphate in gypsum in inland salt pans of southern Africa. Abstr. Geocongress '86, Geological Society of South Africa, Johannesburg, 1049-1052.

Retallack, G.J., 1986. Reappraisal of a 2200-Ma-old paleosol from near Waterval Onder, South Africa. Precambrian Research, 32, 195-252.

Retallack, G.J., 1991a. Untangling the effects of burial alteration and ancient soil formation. Annual Review of Earth and Planetary Sciences, 19, 183-206.

Retallack, G.J., 1991b. Miocene paleosols and ape habitats in Pakistan and Kenya. London, U.K., Oxford University Press, 346 p.

Retallack, G.J., 1993. Classification of paleosols: Discussion and reply. Geological Society of America Bulletin, 105, 1635-1637.

Retallack, G.J., 1997. A Color Guide to Paleosols. Wiley, Chichester, 175 p.

Retallack, G.J., 2007. Soils and global change in the carbon cycle over geological time. In: Holland H.D. and Turekian, K.K., eds., Treatise on geochemistry, Pergamon Press, Oxford, 5, 581-605.

Retallack, G.J. and Huang, C., 2010. Depth to gypsic horizon as a proxy for paleoprecipitation in paleosols of sedimentary environments. Geology, 38, 403-406.

Rimstidt, J.D., 1997. Quartz solubility at low temperatures. Geochimica et Cosmochimica Acta, 61, 2553-2558.

Roerdink, D.L., Mason, P.R.D., Farquhar, J., Reimer, T., 2012. Multiple sulfur isotopes in Paleoarchean barite identify an important role for microbial sulfate reduction in the early marine environment. Earth and Planetary Science Letters, 331-332, 177-186.

Robb, L.J., Barton, J.M., Kable, E.J.D. and Wallace, R.C., 1986. Geology, geochemistry and isotopic characteristics of the Archaean Kaap Valley Pluton, Barberton Mountain Land, South Africa. Precambrian Research, 31, 1-36.

Rossi, A.P., Neukum, G., Pondrelli, M., van Gasselt, S., Zegers, T., Hauber, E., Chicarro, A. and Foing, B., 2008. Large-scale spring deposits on Mars? Journal of Geophysical Research, Planets, 113, E8.

Sanchez-Garrido, C., Stevens, G., Armstrong, R.A., Moyen, J.-F., Martin, H. and Doucelance, R., 2011. Diversity in Earth's early felsic crust: Paleoarchean peraluminous granites of the Barberton Greenstone Belt. Geology, 39, 963-966.

Sawlowicz, Z., 1993. Pyrite framboids and their development: A new conceptual mechanism: Geologische Rundschau, 82, 148-156.

Schoonen, M.A.A., 2004. Mechanisms of Sedimentary Pyrite Formation. In: Geological Society of America Special Papers, Amend J.P., Edwards K.J., Lyons T.W., eds., Sulfur Biogeochemistry, Past and Present. The Geological Society of America, Boulder, CO, 379, 117-134.

Scott, D.H. and Tanaka, K.L., 1986. Geologic Map of the Western Equatorial Region of Mars I-1802-A. U.S. Geological Survey, Flagstaff, AZ, USA.

Sedletsky, V.I., 1971. Some features of authigenic quartz formation in evaporate basins (in Russian). Geologika Geofizika, 5, 72-77.

Shen, Y. and Buick, R., 2004. The antiquity of microbial sulfate reduction. Earth-Science Reviews, 64, 243-272.

Shen, Y., Buick, R. and Canfield, D.E., 2001, Isotopic evidence for microbial sulphate reduction in the early Archaean era. Nature, 410, 77- 81.

Sheldon, N.D., 2006. Precambrian paleosols and atmospheric CO2 levels. Precambrian Research, 147, 124-155.

Siebach, K.L., Grotzinger, J.P., Kah, L.C., Stack, K.M., Malin, M., Léveillé, R. and Sumner, D.Y., 2014. Subaqueous shrinkage cracks in the Sheepbed mudstone: Implications for early fluid diagenesis, Gale crater, Mars, Journal of Geophysical Research, Planets, 119, 1597–1613.

Smoot, J.P. and Castens-Seidell, B. 1994. Sedimentary features produced by efflorescent crusts, Saline Valley and Death Valley, California. In: Renaut R.W., Last W.M., (Eds.), Sedimentology and Geochemistry of Modern Ancient Saline Lakes, SEPM Special Publication, Tulsa, 50, 73-90.

Simpson, E.L., Eriksson, K.A. and Mueller, W., 2012. 3.2 Ga eolian deposits from the Moodies Group, Barberton Greenstone Belt, South Africa: Implications for the origin of first-cycle quartz sandstones. Precambrian Research, 214/215, 185-191.

Squyres, S.W., Arvidson, R.E., Ruff, S., Gellert, R., Morris, R.V., Ming, D.W., Crumpler, L., Farmer, J.D., Des Marais, D.J., Yen, A., McLennan, S.M., Calvin, W., Bell, J.F., Clark, B.C., Wang, A., McCoy, T.J., Schmidt, M.E. and de Souza, P.A., 2008. Detection of Silica-Rich Deposits on Mars. Science, 320, 1063-1067.

Stack, K.M., Grotzinger, J.P. Kah, L.C., Schmidt, M.E., Mangold, N., Edgett, K.S., Sumner, D.Y., Siebach, K.L., Nachon, M., Lee, R., Blaney, D.L., Deflores, L.P., Edgar, L.A., Fairén, A.G., Leshin, L.A., Maurice, S., Oehler, D.Z., Rice, M.S., and Wiens, R.C., 2014. Diagenetic origin of nodules in the

Sheepbed member, Yellowknife Bay formation, Gale crater, Mars. Journal of Geophysical Research, Planets, 119, 1637-1664.

Sumner D.Y. and Grotzinger J.P., 2004. Implications for Neoarchaean ocean chemistry from primary carbonate mineralogy of the Campbellrand-Malmani Platform, South Africa. Sedimentology, 51, 1-27.

Tanaka, K.L., 1986. The Stratigraphy of Mars. Journal of Geophysical Research, 91, 139-158.

Tegtmeyer, A. and Kröner, A., 1987. U-Pb zircon ages bearing on the nature of early Archaean greenstone belt evolution, Barberton Mountainland, southern Africa. Precambrian Research, 36, 1-20.

Thode, H.G., 1991. Sulphur Isotopes in Nature and the Environment: An Overview, in Krouse, H.R. and Grinenko, V.A., eds., Stable Isotopes in the Assessment of Natural and Anthropogenic Sulphur in the Environment: John Wiley & Sons Ltd., SCOPE, 43, 1-26.

Thomazo, C., Pinti, D., Busigny, V., Ader, M., Hashizume K., Philippot, P., 2009. Biological activity and the Earth's surface evolution: insights from carbon, sulfur, nitrogen and iron stable isotopes in the rock record. Palevol, C.R., ed., 8, 665-678.

Treiman, A. H., Morris, R.V., Agresti, D.G., Graff, T.G., Achilles, C.N., Rampe, E.B., Bristow, T.F., Ming, D.W., Blake, D.F., Vaniman, D.T., Bish, D.L., Chipera, S.J., Morrison, S.M. and Downs, R.T., 2014. Ferrian saponite from the Santa Monica mountains (California, U.S.A., Earth): Characterization as an analog for clay minerals on Mars with application to Yellowknife Bay in Gale Crater, American Mineralogist, 99, 2014-4763.

Ueno, Y., 2014. Coping with low ocean sulfate. Science, 346, 703-704.

Ueno, Y., Ono, S., Rumble, D. and Maruyamas, S., 2008. Quadruple sulfur isotope analysis of c. 3.5 Ga Dresser Formation: new evidence for microbial sulfate reduction in the early Archean. Geochimica et Cosmochimica Acta, 72, 5675-5691.

Vaniman, D.T., Bish, D.L., Ming, D.W., Bristow, T.F., Morris, R.V., Blake, D.F., Chipera, S.J., Morrison, S.M., Treiman, A.H., Rampe, E.B., Rice, M., Achilles, C.N., Grotzinger, J.P., McLennan, S.M., Williams, J., Bell III, J.F., Newsom, H.E., Downs, R.T., Maurice, S., Sarrazin, P., Yen, A.S., Morookian, J.M., Farmer, J.D., Stack, K., Milliken, R.E., Ehlmann, B.L., Sumner, D.Y., Berger, G., Crisp, J.A., Hurowitz, J.A., Anderson, R., Des Marais, D.J., Stolper, E.M., Edgett, K.S., Gupta, S., Spanovich, N., and MSL Science Team, 2014. Mineralogy of a mudstone at Yellowknife Bay, Gale crater, Mars. Science, 343, 1243480.

Viljoen, M.J. and Viljoen, R.P., 1969. The geology and geochemistry of the lower ultra-mafic unit of the Onverwacht Group and a proposed new class of igneous rocks. Geological Society of South Africa Special Publication, 2, 55-86.

Visser, S., 1963. Gips in Die Republiek van Südafrika. Geological Survey, Department of Mines, Pretoria, Handbook 4.

Walker, R.N., Muir, M.D., Diver, W.L., Williams, N. and Wilkins, N., 1977. Evidence of major sulphate evaporite deposits in the Proterozoic McArthur Group, Northern Territory, Australia. Nature, 265, 526-529.

Warren, J. K., 2006. Evaporites: sediments, resources and hydrocarbons. Springer, Berlin, Heidelberg, New York, NY, United State, 1035 p.

Watanabe, Y., Martini, J.E.J. and Ohmoto, H. 2000. Geochemical evidence for terrestrial ecosystems 2.6 billion years ago. Nature, 408, 574-578.

Weaver, C.E., 1989. Clays, Muds and Shales. Elsevier, Amsterdam, Oxford, New York, Tokyo, 819 p.

Wilkin, R.T., Barnes, H.L., and Brantley, S.L., 1996. The size distribution of framboidal pyrite in modern sediments: an indicator of redox conditions: Geochimica et Cosmochimica Acta, 60, 3897-3912.

Wray, J.J., 2013. Gale crater: the Mars Science Laboratory/Curiosity Rover Landing Site. International Journal of Astrobiology, 12, 25-38.

Zeh, A., Gerdes, A. and Heubeck, C., 2013. U-Pb and Hf isotope data of detrital zircons from the Barberton Greenstone Belt: constraints on provenance and Archaean crustal evolution. Journal of the Geological Society London, 170, 215-223.

Zhelezinskaia, I. Kaufmann, A.J., Farquhar, J. and Cliff, J., 2014. Large sulfur isotope fractionations associated with Neoarchean microbial sulfate reduction. Science, 346, 742-744.

Appendix

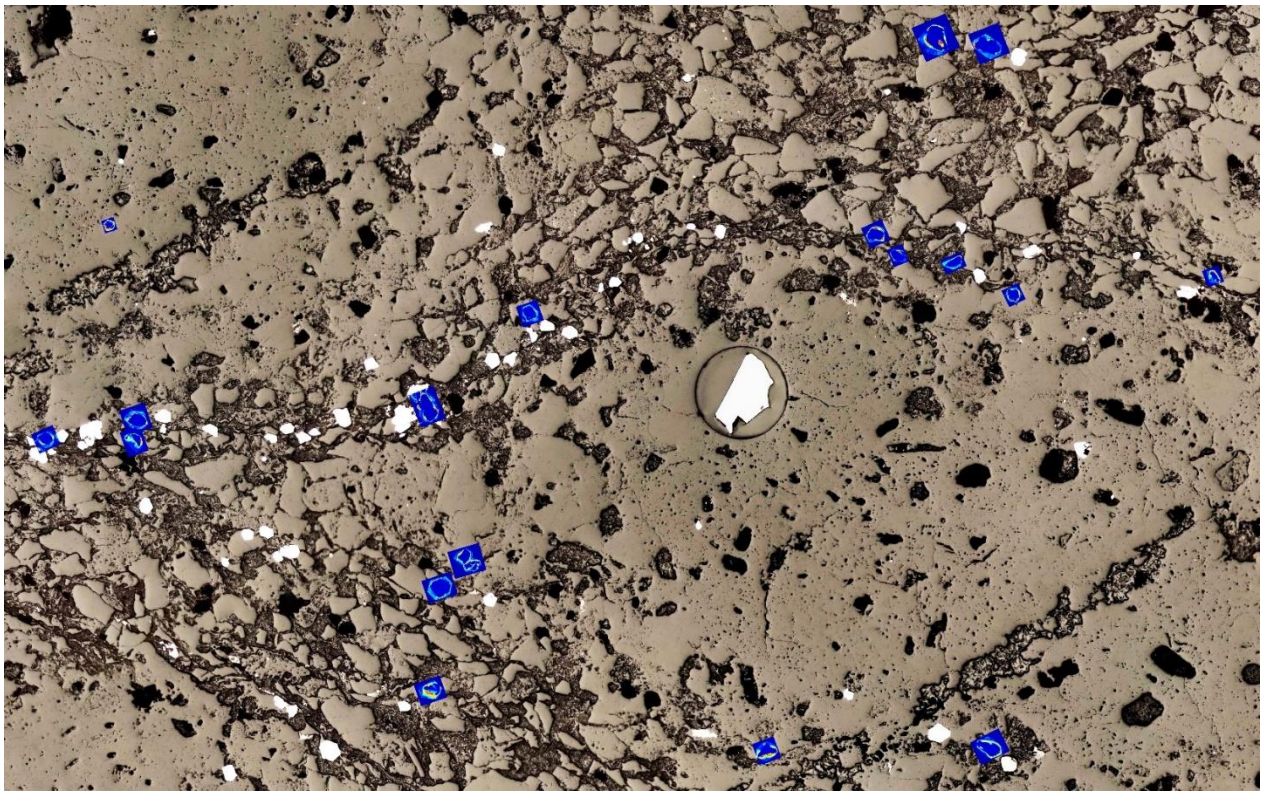

Title Figure: RL-image of sample mount 12;003-4g with overlain TE maps of targeted pyrites for SIMS S-isotope measurements. The large pyrite grain in the pit (center right) is the GM3-Ball standard.

Appendix A: Additional Information to Chapter 2

Appendix A1: Sample List

Appendix A2: Preliminary S-isotope measurements

Appendix A1: Sample List

TABLE A1. LIST OF SAMPLES FROM THE BARBERTON GREENSTONE BELT, SOUTH AFRICA

Sample number	Date	Location	GPS	Comments
12;001-1	05.08.2012	Saddleback, Barberton Reservoir	S 25°48,798' E 031°06,496'	Silicified green Moodies sandstone, no nodules
12;002-1	07.08.2012	Stolzburg, southern limb	S 25°55,273' E 030°50,152'	Tuffaceous sandstone with weathered nodules
12;002-2	07.08.2012	Stolzburg, southern limb	S 25°55,273' E 030°50,152'	Tuffaceous sandstone no nodules
12;003-1	09.08.2012	Stolzburg, northern limb, monkey Hill	S 25°53,834' E 030°51,420'	Ripple plate, gray sandstone
12;003-2	09.08.2012	Stolzburg, northern limb, monkey Hill	S 25°53,841' E 030°51,423'	Ripple plate, ferruginous sandstone
12;003-3	09.08.2012	Stolzburg, northern limb, monkey Hill	S 25°53,874' E 030°51,423'	Crystal lawn weathered
12;003-4	09.08.2012	Stolzburg, northern limb, monkey Hill	S 25°53,910' E 030°51,438'	Large block
12;004-1	10.08.2012	Stolzburg, northern limb, 1760 Hill	S 25°54,432' E 030°51,562'	Tuffaceous sandstone with weathered nodules
12;004-2	21.08.2012	Stolzburg, southern limb fence 2	S 25°55,234' E 030°50,423'	Brown weathered sandstone with nodules
12;004-3	21.08.2012	Stolzburg, southern limb fence 2	S 25°55,107' E 030°50,308'	Strongly weathered sandstone with nodules in tuffaceous layers
12;005-1	12.08.2012	Dycedale, white outcrops	S 25°47,681' E 031°04,914'	Silicified green sandstone, no nodules
12;005-2	12.08.2012	Dycedale, white outcrops	S 25°47,627' E 031°04,968'	Silicified green sandstone, with nodules
12;005-3	12.08.2012	Dycedale, white outcrops	S 25°47,544' E 031°05,041'	Lowermost sandstone with fresh nodules
12;005-4	12.08.2012	Dycedale, white outcrops	S 25°47,595' E 031°05,020'	White mudstone from layer without nodules
12;005-5	12.08.2012	Dycedale, white outcrops		Green mudstone from layer with nodules
12;005-6	12.08.2012	Dycedale, white outcrops		Tuffaceous mudstone from layer with nodules
12;005-7	15.08.2012	Dycedale, white outcrops		Graded sandstone without nodules
12;005-8	15.08.2012	Dycedale, white outcrops		Tuffaceous clasts with nodules, partly weathered
12;006-1	13.08.2012	Eureka, Eureka city road	S 25°42,979' E 031°04,980'	Silicified greenish Sandstone with nodules
12;007-1	16.08.2012	Eureka, Clutha creak	S 25°42,003 E 031°04,692'	Sandstone with sideritic clasts/nodules
12;008-1	16.08.2012	Eureka, Ezzy's Pass Road	S 25°40,491' E 031°05,190'	Possible regolith, pebbly sandstone
12;009-1	18.08.2012	Dycedale, Eriksson ridge	S 25°47,570' E 031°05,342'	Sandstone with possible but unlikely siderite clasts
12;009;2	18.08.2012	Dycedale, Eriksson ridge	S 25°47,550' E 031°05,315'	Mudflake plate with possible tuffaceous VAZ

13;006-1	18.07.2013	Eureka city road	S 25°43,184' E 031°04,834'	Concretionary boulder, siltstone
13;006-2	18.07.2013	Eureka city road	S 25°43,182' E 031°04,846'	Country rock, next to concretion-bearing unit
13;003-1	20.07.2013	Stolzburg, northern limb, 3 firebreaks	S 25°53,793' E 030°51,073'	Uppermost Schoongezicht Fm.
13;003-2	20.07.2013	Stolzburg, northern limb, 3 firebreaks		Laminated Schoongezicht tuff
13;009-1	22.07.2013	Dycedale, Eriksson ridge	S 25°47,511' E 031°05,243'	Mudcracks
13;009-2	22.07.2013	Dycedale, Eriksson ridge	S 25°47,509' E 031°05,233'	Mudclast-bearing sandstone
13;005-1	22.07.2013	White outcrops		Consolidated green shale
13;004-1	23.07.2013	Stolzburg east, 1760 Hill	S 25°54,409' E 030°51,560'	Concretionary layer
13;004-2	23.07.2013	Stolzburg east, 1760 Hill	S 25°54,327' E 030°51,767'	Bolder of fine tuff and nodules
13;004-3	23.07.2013	Stolzburg east, 1760 Hill	S 25°54,418' E 030°51,674'	Sandstone with large nodules
13;004-4	23.07.2013	Stolzburg east, 1760 Hill	S 25°54,454' E 030°51,577'	Tuffaceous sandstone with nodules
13;004-5	26.07.2013	Stolzburg SE, firebreak	S 25°54,874' E 030°51,493'	sandstone with greenish laminae
13;004-6	26.07.2013	Stolzburg SE, firebreak	S 25°54,877' E 030°51,477'	Nodule rich sandstone
13;004-7	26.07.2013	Stolzburg SE, firebreak	S 25°54,875' E 030°51,471'	Tuff clast, large
13;011-1	04.08.2013	Malmani Dol.	S25°22,118' E 030°42,915'	Barite lawn
13;012-3	06.08.2013	Sheba creek		Sandstone with small holes
13;012-4	06.08.2013	Sheba creek	S 25°42,939' E 31°10,014'	Chert with pyrite
13;004-8	07.08.2013	Stolzburg east of 1720 Hill	S 25°54,096' E 030°51,549'	Nodules in cross-bedded sandstone
13;004-9	07.08.2013	Stolzburg east of 1720 Hill		Unusual nodules
13;004-10	07.08.2013	Stolzburg west of 1720 Hill	S 25°54,178' E 030°51,402'	Tuff with nodules
13;004-11	07.08.2013	Stolzburg west of 1720 Hill	S 25°54,239' E 030°51,403'	Medium sandstone silicified with nodules
13;004-12	07.08.2013	Stolzburg west of 1720 Hill	S 25°54,201' E 030°51,473'	Large medium sandstone with nodules

Appendix A2: Preliminary S-isotope measurements

To prepare the *in-situ* SIMS measurements, preliminary bulk S-isotope analysis was done at the Department of Geology and Paleontology of the Westfälische Wilhelms Universität in Münster using a ThermoScientific MAT 253 with attached fluorination system to measure multiple sulfur isotopes (^{32}S, ^{33}S, ^{34}S, and ^{36}S) of sulfur from pyrite converted to SF_6. Four samples from three locations were measured. These represent different depositional environments and contain pyrite that formed due to different processes and from different Sulfur sources.

1. Samples

Sample 13;012-4 was obtained from an outcrop at Fig Tree Creek at the southern limb of the eastern Eureka Syncline (S 25°42,939' E 31°10,014'). The sampled horizon is a 20 cm thick chert bed and forms part of an around 20 m thick, fine-sandy to silty succession (App. Fig. A2.1) in the upper Sheba Formation of the Fig Tree Group. The location is stratigraphically a few tens of meters below the Fig Tree-Moodies Groups contact that is marked by the Sheba fault system. The stratigraphic and lithologic context places the chert bed in a marine environment of a few 10s to about 100 m water depth. The tectonic context with the nearby Sheba fault and the fault-related sulfidic gold deposits implies that the up to 3 mm large euhedral, cubic pyrite crystals in the chert bed are related to this sulfidic mineralization event.

The chert bed shows lamination along which the pyrite crystals are aligned. Thin section microscopy revealed enrichment of pyrite crystals in some lamina while others contain only few or no pyrite. Pyrite-free laminae are enriched in organic material and show numerous, up to 100 µm large dolomite rhombs. Late burial diagenetic or metamorphic quartz veins pass through the sampled material and are in thin sections clearly distinguishable from the original chert due to their brighter appearance (App. Fig. A2.2).

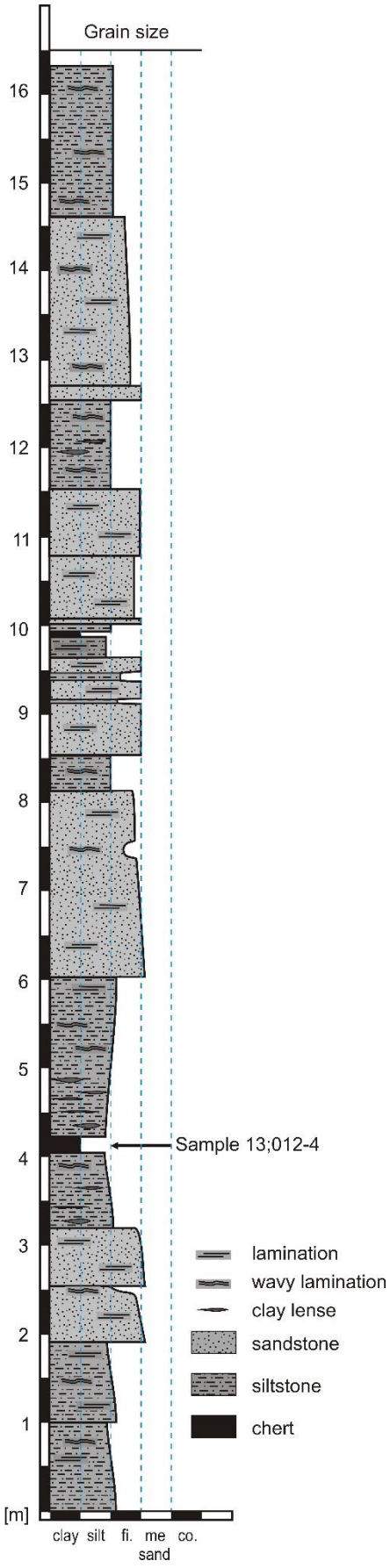

App. Fig. A2.1 (left): Stratigraphic section of the fine-sandy to silty succession of the upper Sheba formation of the Fig Tree Group. The sampled chert bed (sample 13;012-4) around meter 4 of the section is ~20 cm thick. A second, thinner chert bed is located around meter 10. Both chert beds form the top of a fining upward section.

App. Fig. A2.2 (below): Thin section image of sample 13;012-4. The upper part contains numerous up to 3 mm large cubic pyrite crystals aligned along bedding. The lower part of the thin section contains several dark, organic rich laminae (black arrows) and dolomite rhombs (black circles).

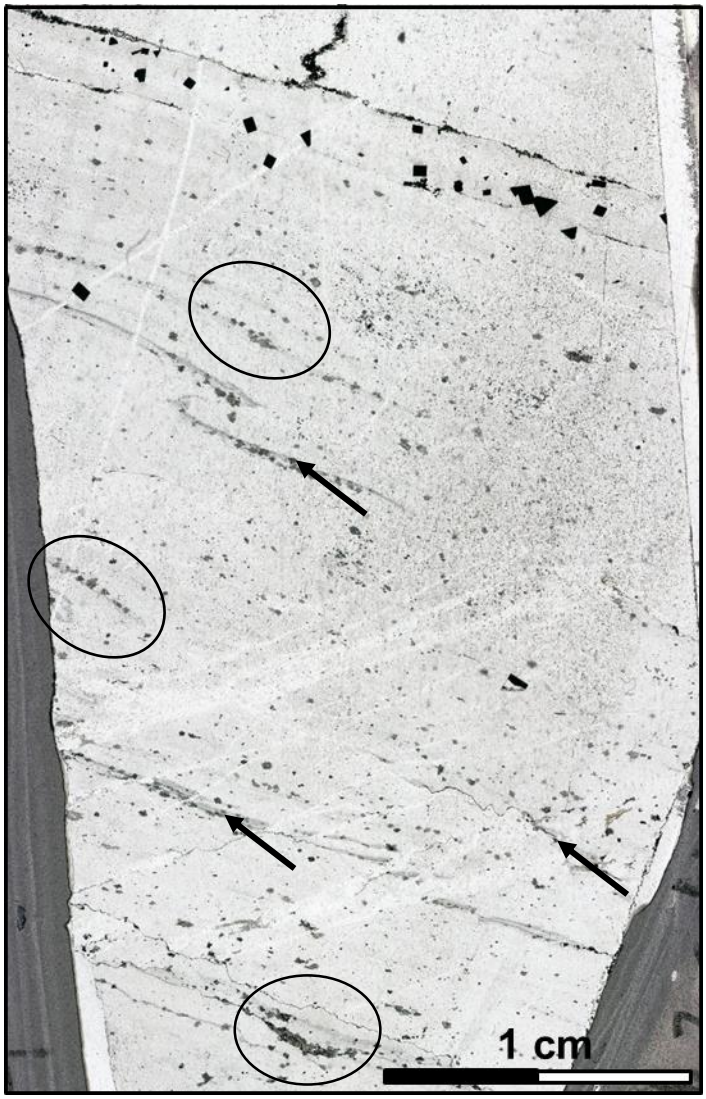

Sample 12;007-1 is an about 15 cm by 25 cm large block from the lower Moodies Group Clutha Formation from the southwestern limb of the Eureka Syncline. Its stratigraphic position is about 50 m above the Fig Tree - Moodies Groups contact. It belongs to a ~5 m thick succession of interbedded coarse-grained sandstone and nearly monomict intraclast conglomerate. The stratigraphically lower part of the sample is composed of greenish, coarse-grained sandstone while its upper part is conglomeratic and dark gray (App. Fig. A2.3). Pyrite within the sandstone occurs spottily in up to 3 mm large subhedral, commonly pore-filling agglomerates. In the conglomerate bed, pyrite is mainly pore-filling, subhedral and up to 1 mm in diameter (App. Fig. A2.3).

Sample 12;003-4 is described in detail in chapter 4. It contains common, mm-thick heavy mineral laminations, mainly composed of detrital pyrite with euhedral secondary overgrowths (Title Fig. chapter 4).

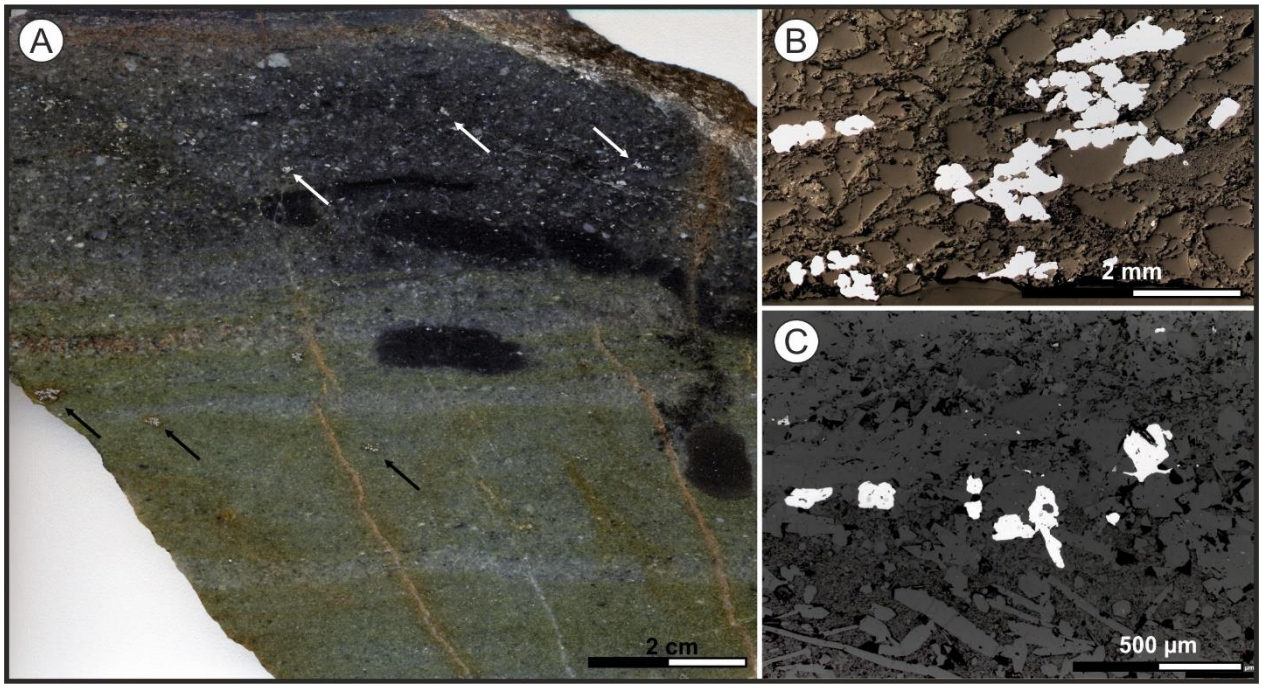

App. Fig. A2.3: Pyrite containing sample 12;007-1. A) Polished slab with dark gray conglomerate on top, containing pore-filling subhedral pyrite (white arrows). The greenish, coarse-grained sandstone below contains larger but spottier pyrites (black arrows). B) Reflected light (RL) image of pyrite rich spot from the coarse-sandy area. The pyrite is mainly pore filling with up to 1.5 mm large subhedral crystals. C) RL image of pyrite from the conglomeratic part of sample 12;007-1. The pore filling pyrite is more widely distributed with smaller crystals comparted to the sandy part of the sample.

2. Sample preparation

All three samples were treated using standard heavy-mineral separation techniques described in chapter 2.6.1. For sample 13;012-4 and 12;007-1 each, only one analysis was performed because of the homogeneous appearance of the separated pyrite. Sample 12;003-4 showed a bimodal distribution of pyrite morphology with subrounded and euhedral grains. Subsequently the two fractions were separated by hand-picking and measured separately as sample 12;003-4 det. (subrounded) and 12;003-4 0.1-0.2 (euhedral).

3. Results

The sulfur-isotopic composition of the measured unknowns and the IAEA-S1 standard are shown in Table A2.1, including the standard deviation for each measured isotope of all samples and in Fig. A2.4. This standard deviation (1 st.) is always ≤ 0.01‰ for ^{34}S and ≤ 0.014‰ for ^{33}S.
Sample 13;012-4 has a slightly positive $\delta^{34}S_{VCDT}$ composition (0.857‰) and a comparatively high $\Delta^{33}S$ (1.272‰) mass-independent sulfur fractionation. Sample 12;007-1 is heavier in $\delta^{34}S_{VCDT}$ (2.368‰) but shows no mass-independent $\Delta^{33}S$ fractionation (0.143‰). Both fractions of sample 12;003-4 show negative $\delta^{34}S_{VCDT}$ values with -6.764‰ for the detrital fraction and -8.232‰ for fraction 0.1-0.2. No mass-independent fraction could be observed. The $\Delta^{33}S$ values (0.056‰ and -0.049‰) are within the $\Delta^{33}S$ range of ±0.2‰ that reflects mass-dependent fractionation.

App. Table A2.1: Bulk S-isotopic composition of pyrite from the BGB. All values are given in ‰.

Sample	$\Delta^{33}S$	$\Delta^{36}S$	$\delta^{34}S$ vs S1	$\delta^{34}S$ vs CDT	StdDev ^{33}S	StdDev ^{34}S	StdDev ^{36}S
IAEA-S1	0.081	-0.058	-0.113	-0.413	0.014	0.007	0.099
13;012-4	1.272	-0.154	1.157	0.857	0.008	0.006	0.114
12;007-1	0.143	0.718	2.368	2.068	0.014	0.010	0.080
12;003-4 det.	0.056	0.773	-6.466	-6.764	0.011	0.007	0.138
12;003-4 0.1-0.2	-0.049	1.064	-7.934	-8.232	0.011	0.006	0.114
IAEA-S1	0.082	0.066	-0.038	-0.338	0.014	0.004	0.115

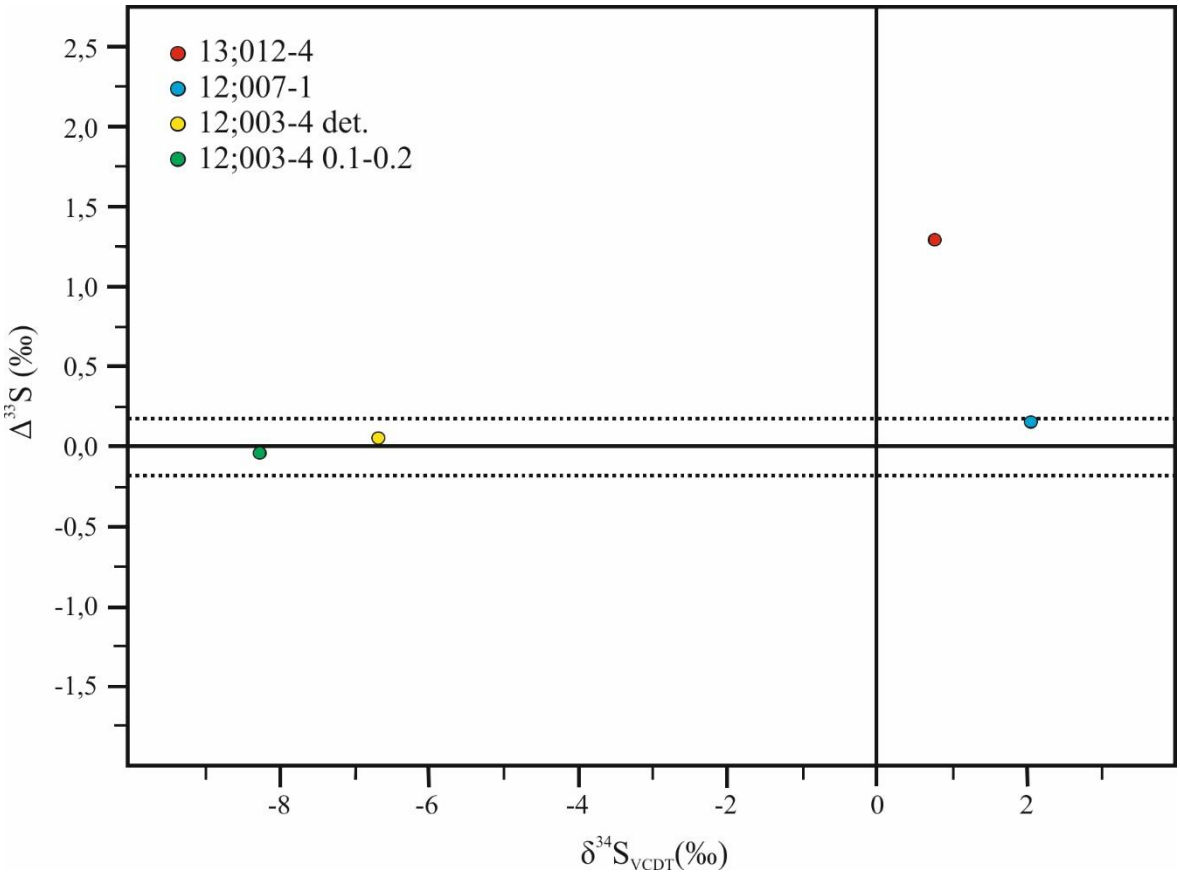

App. Fig. A2.4: Plot of $\Delta^{33}S$ vs $\delta^{34}S_{VCDT}$ for pyrite bulk analyses of samples from the Moodies Group and sample 13;012-4 from the uppermost Fig Tree Group. The S-isotopic composition of sample 12;007-1 plots in the field typical of hydrothermal and volcanogenic massive sulfide. The MIF signal detected in sample 13;012-4 of $\Delta^{33}S = 1.272$ shows the contribution of an atmospheric sulfur source to its formation. The negative $\delta^{34}S_{VCDT}$ signal down to -8.232 shows a possible biogenic involvement in the formation of the measured pyrite.

4. Interpretation

The $\delta^{34}S_{VCDT}$ composition of sample 13;012-4 lies within the range of most Archean sulfides (±5‰; Thomazo et al., 2009). The positive $\Delta^{33}S$ mass-independent fractionation signal, however, shows the involvement of sedimentary derived sulfur that was fractionated by Archean UV radiation (Farquhar et al., 2000, 2001; Pavlov and Kasting, 2002; Mojzsis et al., 2003). The close relation of the sample near the Sheba fault and the Sheba gold mine complex and the cubic shape of the pyrite implies a strong contribution of sulfidic ore mineralization event to the formation of the pyrite. However, the detected MIF signal shows an additional contribution of sedimentarily introduced sulfur that had been in contact with the Archean atmosphere. Therefore, the pyrite of

sample 13;012-4 contains most likely a mixture of sedimentary derived and hydrothermally derived sulfide.

The S-isotopic composition of the pyrite from sample 12;007-1 shows no MIF signal. Its slightly positive $\delta^{34}S_{VCDT}$ composition, together with the pore-filling character and the close spatial relation of the sample near the Fairview gold mine of the Eureka Syncline all suggest a hydrothermal formation of the pyrite as part of the ore-forming mineralization event at about 3126±21 Ma (de Ronde et al., 1991; Agangi et al., 2014).

The bimodal composition of the pyrite from sample 12;003-4 with secondary overgrowth on detrital grains does not allow for a straightforward, simple interpretation of their bulk S-isotopic composition. The documented lack of a MIF signal likely applies to both the detrital and the secondary component. However, it is also possible that the detrital component interferes with the secondary component to create the near-zero $\Delta^{33}S$ signal. The detrital component of the pyrite shows two morphologically distinct fractions, porous and massive, as described in chapter 4. The massive fraction is most likely of igneous provenance while the porous fraction is probably of sedimentary origin (England et al., 2002). While the massive fraction most probably lacks a MIF signal, it is possible that the porous fraction shows a positive signal similar to that detected in sample 13;012-4. Such a signal might mask a negative MIF signal of the secondary overgrowth. The slightly positive (0.056‰) $\Delta^{33}S$ signal of sample 12;003-4 det. that contains a larger portion of the detrital component in contrast to the slightly negative (-0.049‰) $\Delta^{33}S$ signal of sample 12;003-4 0.1-0.2 with a larger portion of the secondary component can be an expression of such a scenario. However, the measured $\Delta^{33}S$ values both being close to zero requires a weak MIF signal within both the detrital and the secondary component.

Both 12;003-4 samples show a light $\delta^{34}S_{VCDT}$ composition; the sample with a larger detrital component (12;003-4 det.) is heavier in $\delta^{34}S_{VCDT}$. The lighter values of sample 12;003-4 0.1-0.2 with the higher proportion of the secondary component implies that this secondary component is of light composition while the detrital component has a heavier $\delta^{34}S_{VCDT}$ composition. This implication is confirmed by the *in-situ* SIMS analysis, described and interpreted in chapter 4.

Appendix B: Additional Information to Chapter 3

Appendix B1: Stratigraphic sections and geological map of the Stolzburg Syncline

Appendix B2: Raman spectrum of anhydrite inclusion

Appendix B3: Raman spectrum of calcite inclusion

Appendix B1: Stratigraphic sections and geological map of the Stolzburg Syncline

Locations of stratigraphic sections are marked with blue lines in the map, red dots are sample locations.
The stratigraphic sections are correlated using the Fig Tree – Moodies Groups contact and distinct, traceable tuff- and concretion-bearing beds (green fields between the sections). The numbers on the horizontal arrows state the lateral distance along strike between the sections.

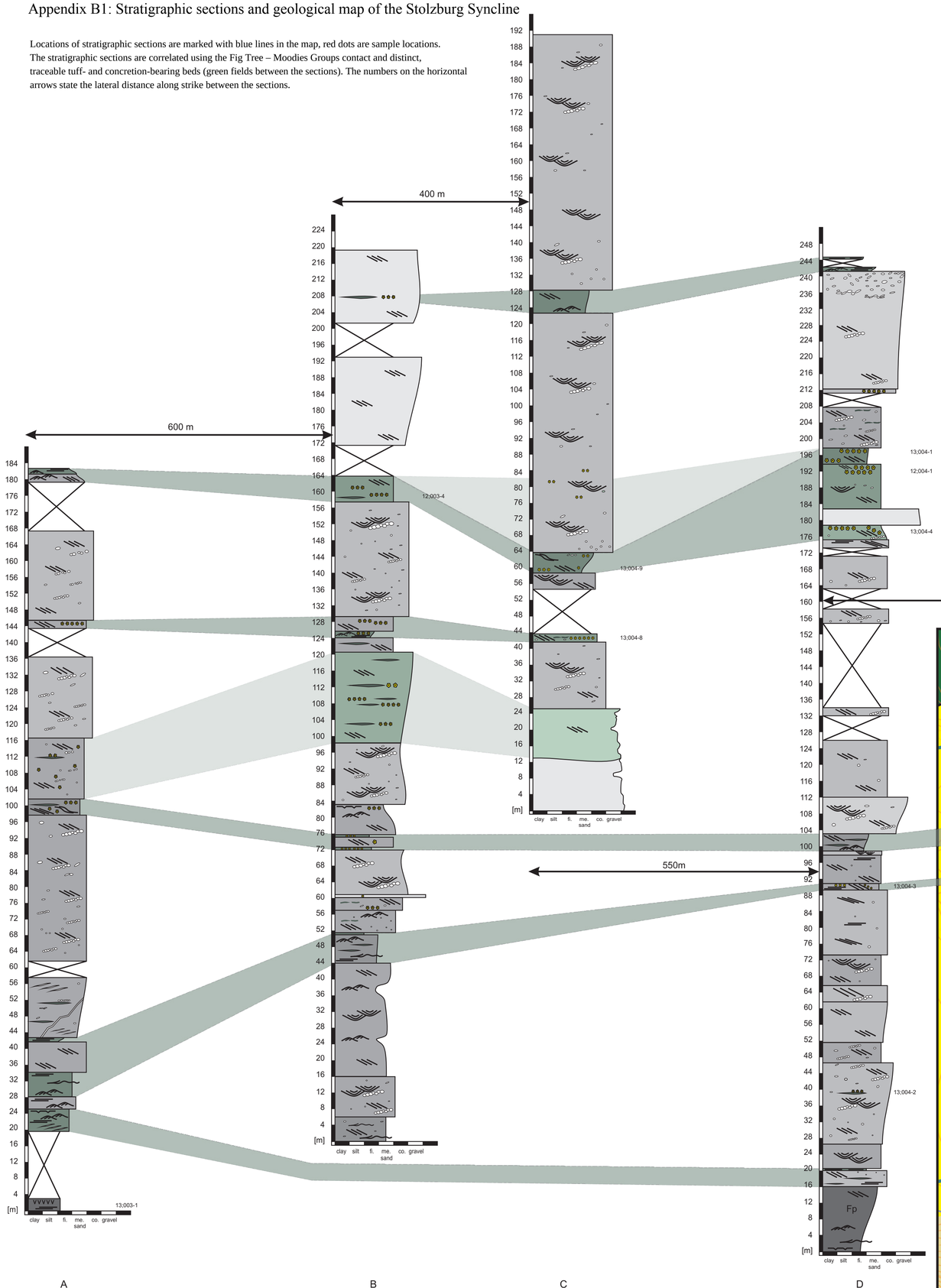

Stratigraphic sectiones of the lower braided fluvial Moodies deposits in the Eastern Stolzburg syncline

Lithologies

Moodies lithologies

- Dacitic tuff
- Tuffaceous fine sandstone
- Fine sandstone
- Tuffaceous medium sandstone
- Medium sandstone
- Tuffaceous coarse sandstone
- Coarse sandstone
- Granulare sandstone
- Tuff clast conglomerate
- Conglomerate

Fig Tree lithologies

- Fp — Feldspar - porphyrie fine sandstone
- vvvv — Vulcanic layer

Structures

Sedimentary structures

- tuff lenses
- concretions
- erosive channels
- tangential cross bedding
- cross bedding
- lamination
- ripples
- tuff clasts
- mud drape
- mudcracks
- pebble string
- pebbles
- tuffaceous clasts

Tectonic structures and others

- Fractures
- Quartz vains
- 13;004-9 Sample number

Legend of the geological map

- 13;004-9 Sampling location/number
- Stratigraphic section
- Road
- Farm boundary
- Fault, inferred
- Fault, mapped
- Inyoka Fault
- Dacitic tuff
- Diabase dike
- Upper Moodies undivided
- Lower Moodies fluvial deposits
- Fig Tree undivided
- Onverwacht undivided

Spheriod WGS 1984
Base map: Chief Directorate, Surveys and Land Information, South Africa
1:50,000, sheet 2630BB Lochiel, third ed., 1984
Mean magnetic declination is 18° 56' E (2013)
Cape Transverse Mercator projection
Elevation is in meters above sea level.

20m contour interval

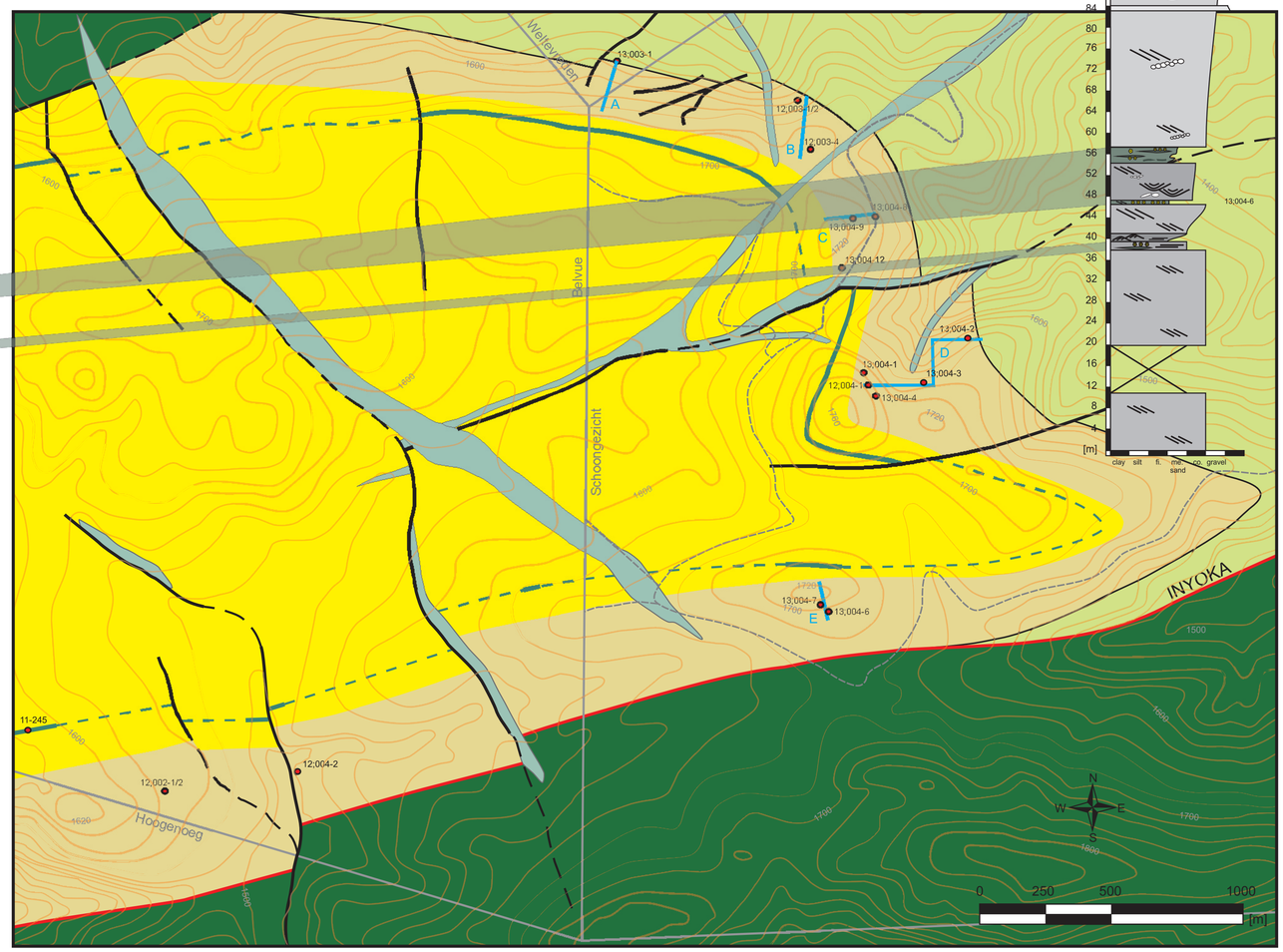

Appendix B2: Raman spectrum of anhydrite inclusion

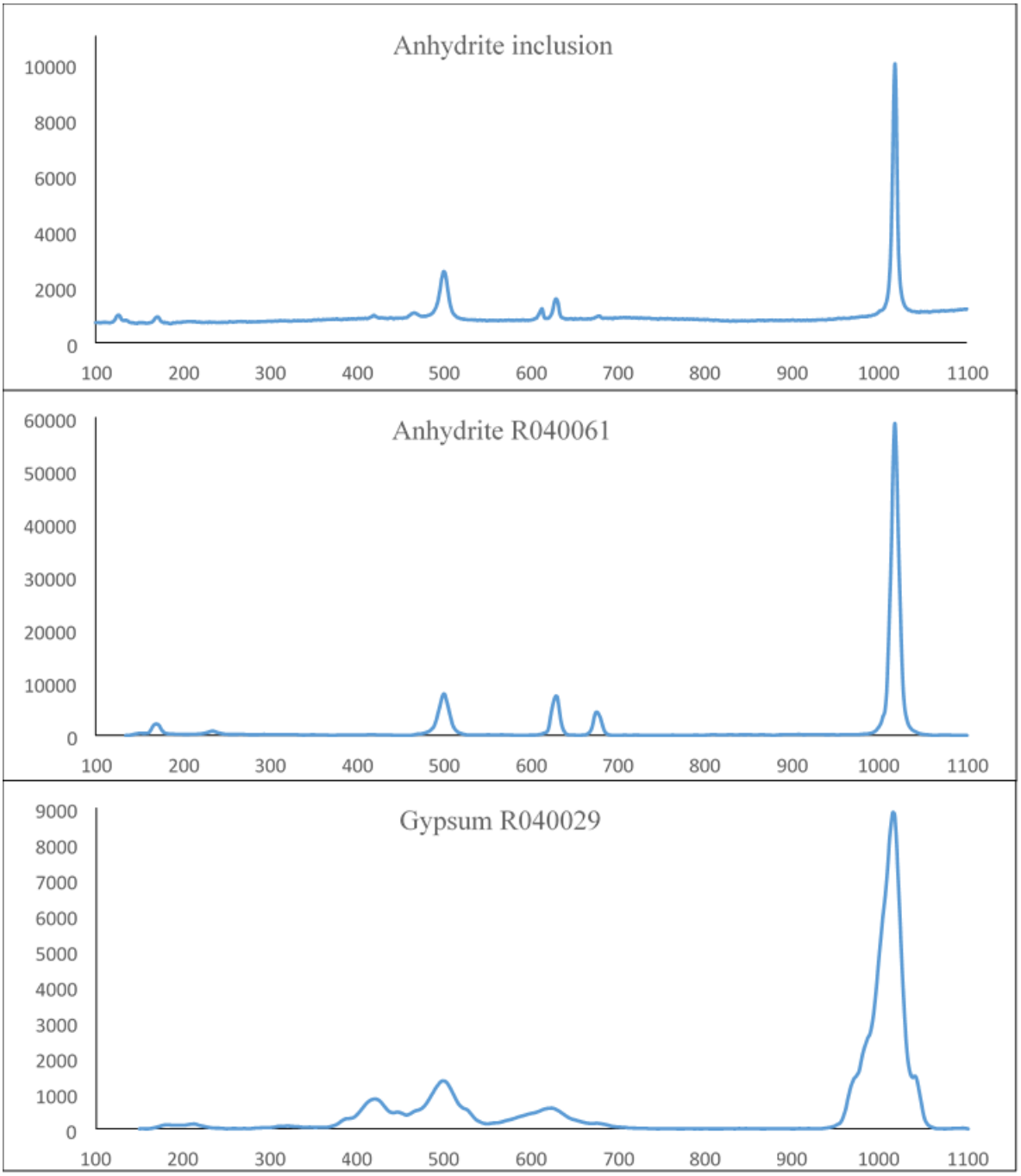

Appendix B2: Raman spectrum of an anhydrite inclusion from a type I concretion (top) compared to two spectra from the RRUFF database (rruff.info; below). The anhydrite spectrum (middle) shows about the same peak positions and similar shapes as the measured inclusion. The gypsum spectrum from the database (below) differs regarding the peak shapes and positions.

Appendix B3: Raman spectrum of calcite inclusion

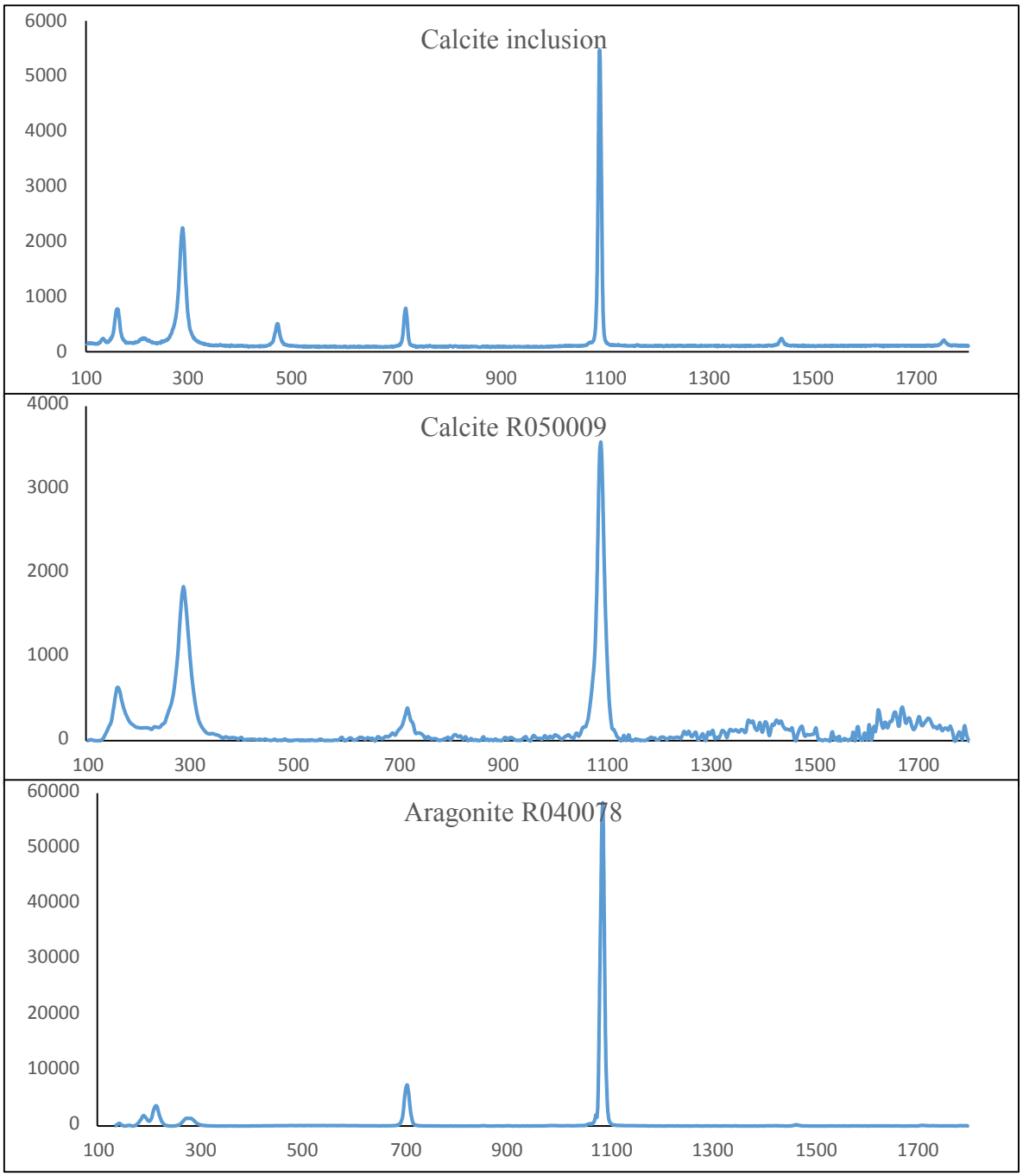

Appendix B3: Raman spectrum of a calcite inclusion from a type-IV concretion (top) compared to two spectra from the RRUFF database (rruff.info; below). The calcite spectrum (middle) shows about the same peak positions and similar shapes as the measured inclusion. The peak shapes of the aragonite spectrum (below) are also similar but the two prominent peaks around 160 cm-1 and 285 cm-1 are absent.

Appendix C: Additional Information to Chapter 4

Appendix C1: Generalized geological maps of the BGB and the eastern SbS

Appendix C2: Stratigraphic column of unit MdQ1 of the lower Moodies Group

Appendix C3: Transmitted-light image of a thin section from sample 12;003-4

Appendix C4: Reflected-light images and TE maps of representative pyrite grains

Appendix C5: Thin-section photomicrograph of sandstone with reworked nodules

Appendix C6: TE maps of metamorphic pyrite from the Eureka Syncline

Appendix C7: EPMA results of zoned pyrite grains

Appendix C8: SIMS results of zoned pyrite grains

Appendix C9: SIMS results of GM3-Bal

Appendix C1: Generalized geological maps of the BGB and the eastern Stolzburg syncline

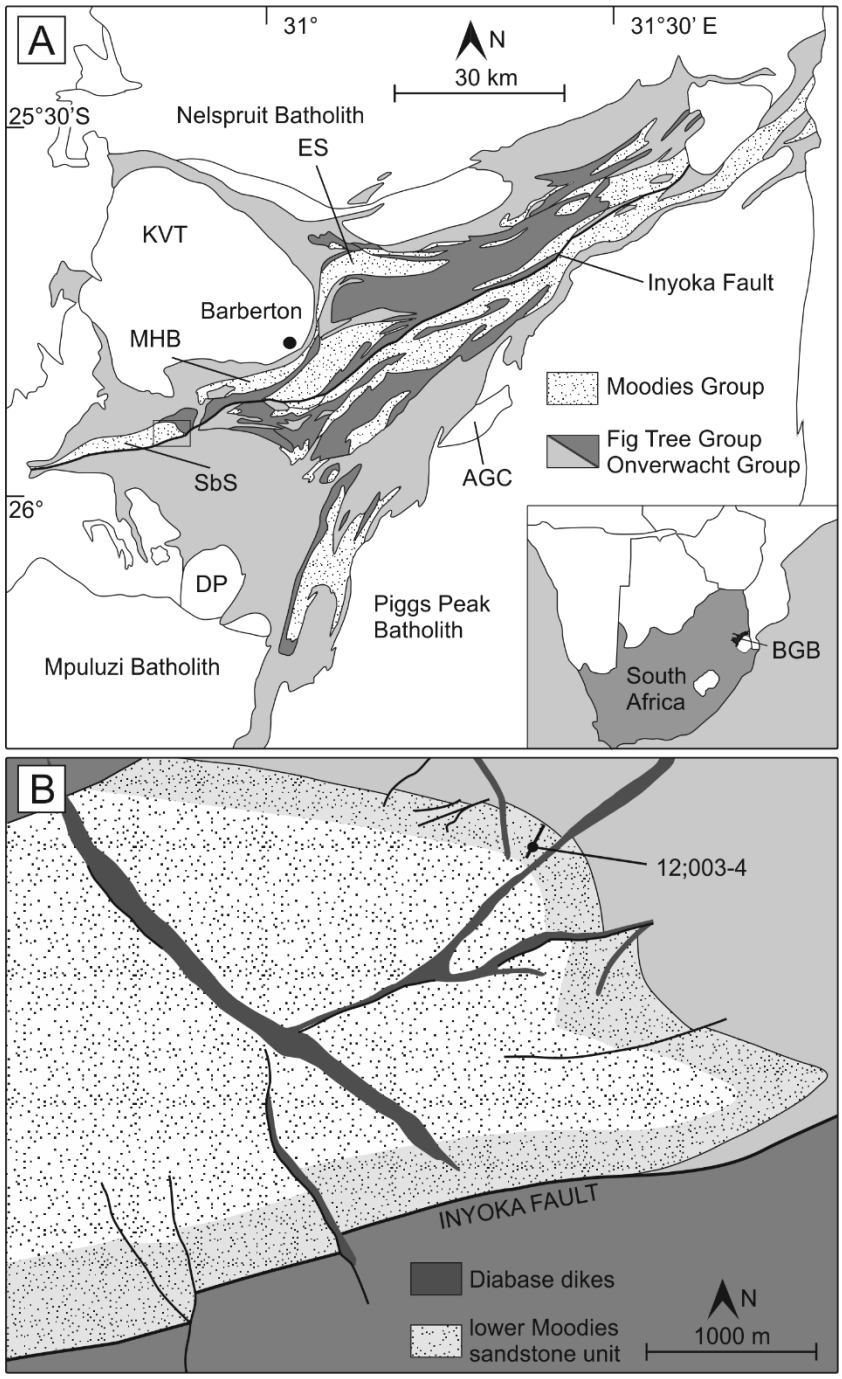

Appendix C1: A: Generalized geological map of the Barberton Greenstone Belt (modified after Heubeck and Lowe, 1994a). The area in the black rectangle is enlarged in B and shows a schematic geological map of the eastern Stolzburg Syncline with the position of sample 12;003-4 (25°53.910' S; 30°51.438' E). AGC: Ancient Gneiss Complex, BGB: Barberton Greenstone Belt, DP: Dalmein Pluton, ES: Eureka Syncline, KVT: Kaap Valley Tonalite, MHB: Moodies Hills Block, SbS: Stolzburg Syncline.

Appendix C2: Stratigraphic column of unit MdQ1 of the lower Moodies Group in the eastern Stolzburg Syncline. The column shows about 220 m of mainly channelized medium- to coarse-grained sandstone in braided-fluvial facies, including the analyzed sample (12;003-4) at m 159. Shorter columns to the right show detailed measured sections.

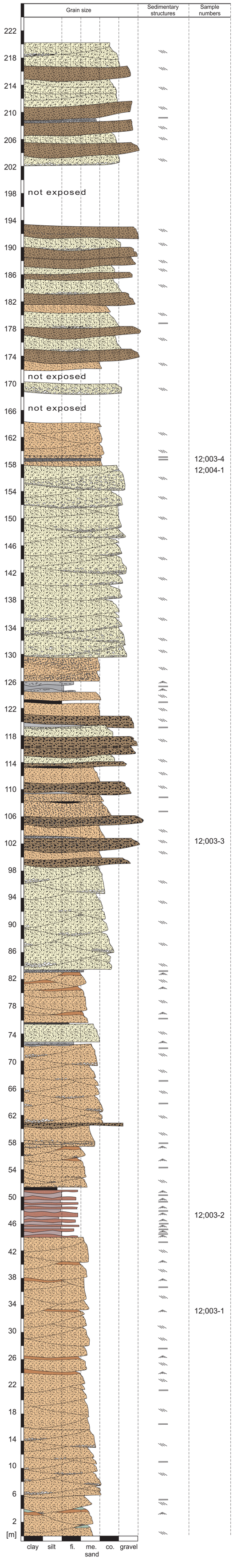

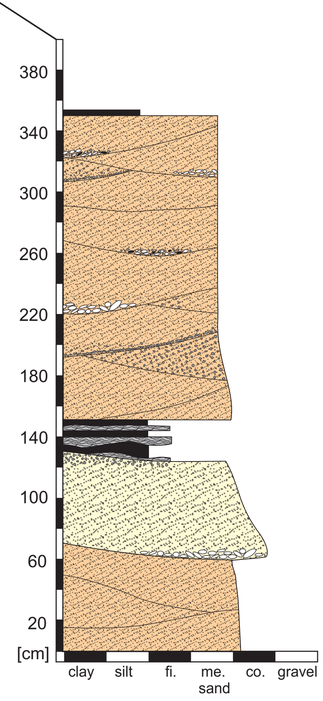

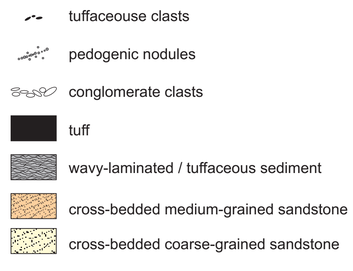

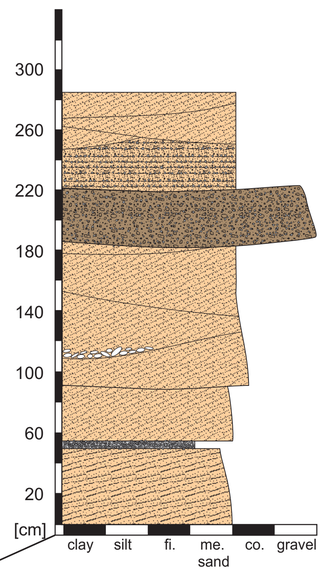

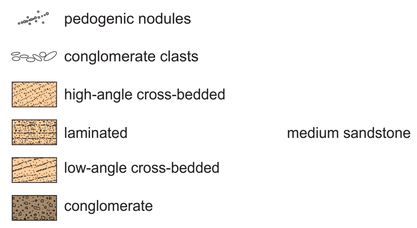

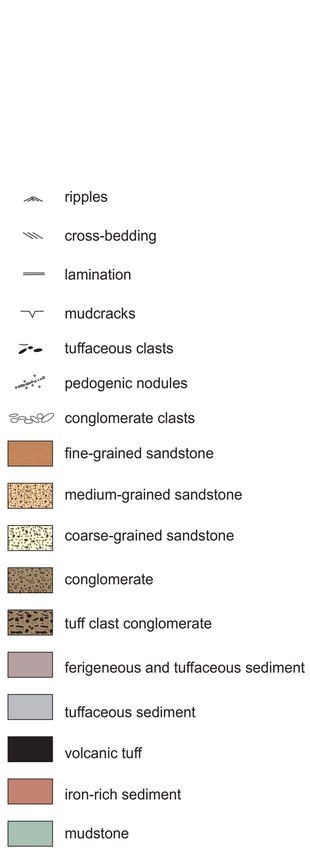

Appendix C3: Transmitted-light image of a thin section from sample 12;003-4

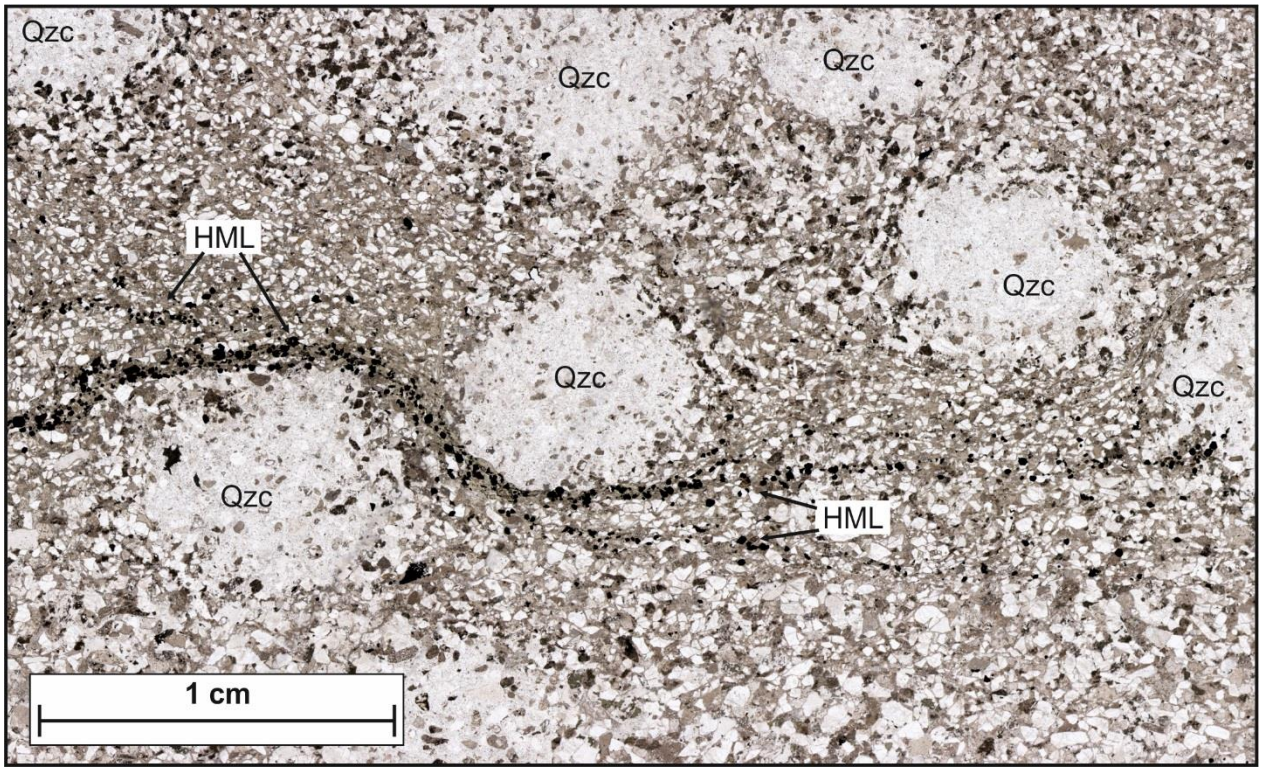

Appendix C3: Transmitted-light image of a representative thin section from sample 12;003-4. Unconsolidated sand, including a heavy-mineral lamina (HML) mainly composed of opaque pyrite, was deformed by compaction around silicified concretions (Qzc). Some heavy mineral grains are overgrown by the concretion to the right.

Appendix C4: Reflected-light images and TE maps of representative pyrite grains

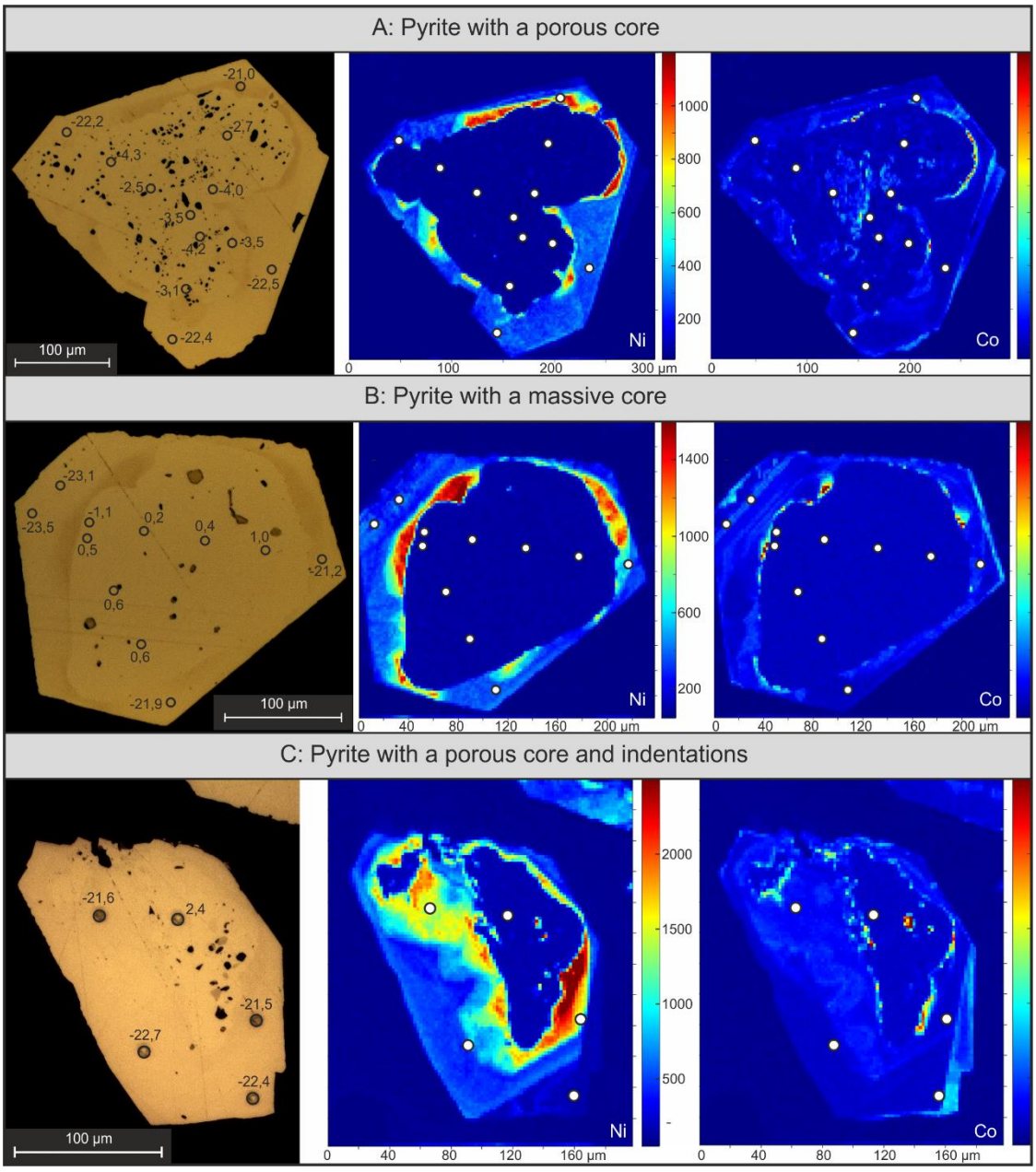

Appendix C4: Reflected-light images (left) and TE maps (center, Ni; right, Co) of representative pyrite grains. SIMS ablation pits are marked by open (left) and filled (center, right) circles. $\delta^{34}S_{VCDT}$ values are noted in the RL images (left). A: Representative pyrite grain with a porous core showing negative $\delta^{34}S$ values. B: Representative pyrite grain with a massive core showing slightly positive $\delta^{34}S$ values. C: Representative pyrite grain with a porous core showing indentations and partial dissolution. The patches of high-TE concentration in the core represent pores filled by secondary pyrite. All grains show a zone of low-TE concentration with slightly heavier $\delta^{34}S$ values than the zone of high- TE concentration.

Appendix C5: Thin-section photomicrograph of sandstone with reworked nodules

Appendix C5. Thin-section photomicrograph of a granuly sandstone with reworked nodules. The large nodule to the upper left shows internal zoning with inward-pointing crystal faces (black arrows) and contains opaque pyrite and magnetite (encircled). The large clast to the upper right is made of chert. The granuly lamina in the lower part of the image contains a small reworked nodule (red circle).

Appendix C6: TE maps of metamorphic pyrite from the Eureka Syncline

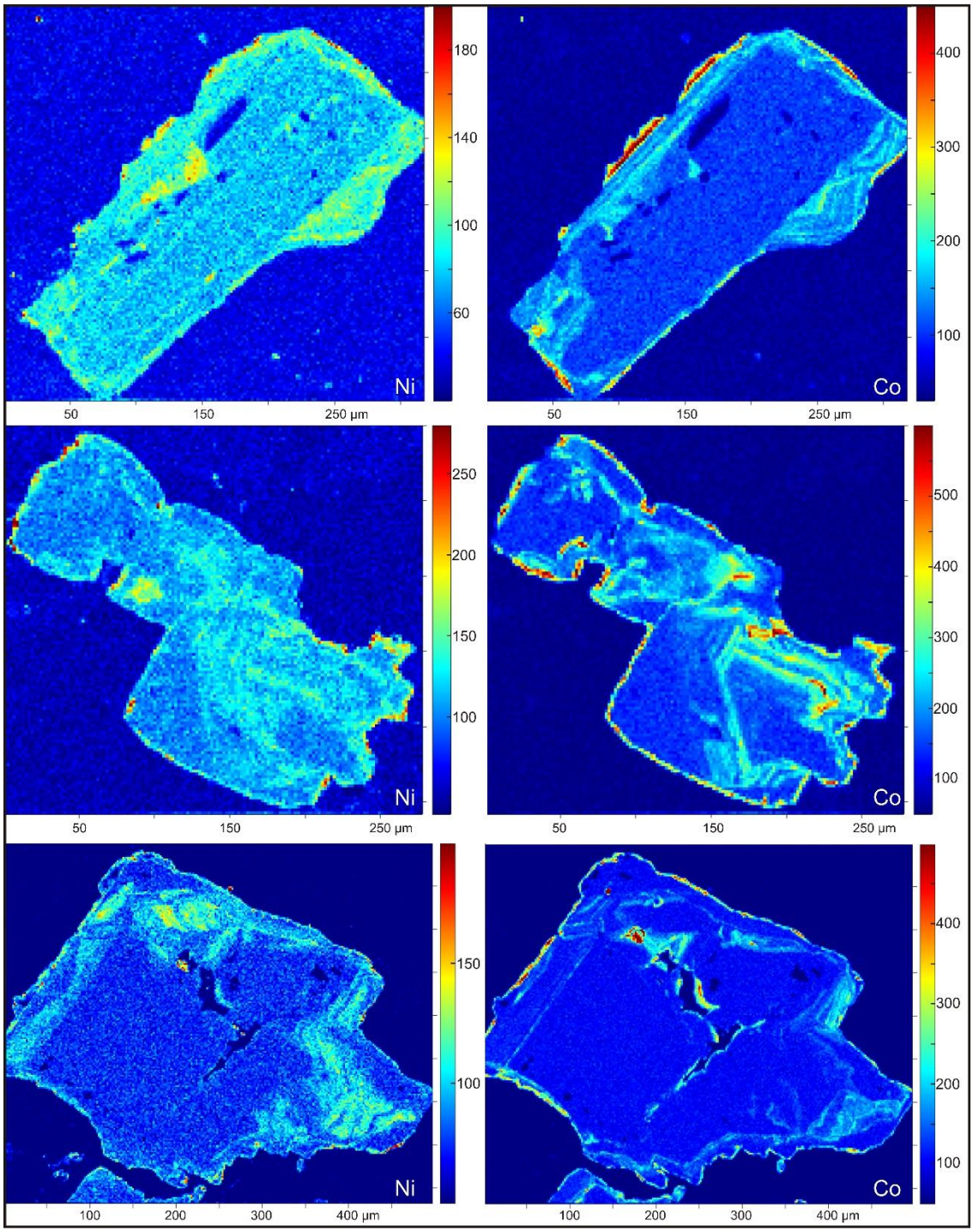

Appendix C6. TE maps (left, Ni; right, Co) of metamorphic pyrite from the Eureka Syncline. TE concentrations, especially of Ni, are generally lower than in the secondary pyrite rims shown in Fig 4.2 and App. C4. Zoning is visible but hardly defined and there is no expression of detrital cores. Color bars to the right show counts per second (cps) of the named TE.

Appendix C7: EPMA results of zoned pyrite grains

TABLE C7. EPMA RESULTS OF ZONED PYRITE GRAINS SHOWING THEIR ELEMENTAL COMPOSITION

Analysis number		Fe (wt.%)	S (wt.%)	Cu (wt.%)	Ni (wt.%)	Co (wt.%)	Total	Co/Ni	Zone
12;003-4f	1	43.974	51.417	0.000	2.474	0.661	98.526	0.27	rim
	2	43.974	51.254	0.000	0.003	0.072	97.674	24.00	core
	3	43.974	51.075	0.010	0.005	0.076	97.057	15.20	core
	6	43.974	48.182	0.032	0.004	0.078	93.843	19.50	core
	7	43.974	50.855	0.005	4.128	0.544	97.859	0.13	rim
	8	43.974	50.806	0.000	0.003	0.069	97.172	23.00	core
	11	43.974	50.637	0.000	0.894	0.145	97.609	0.16	rim
	12	43.974	50.651	0.004	2.656	0.072	97.750	0.03	rim
	13	43.974	48.078	0.009	0.006	0.073	94.574	12.17	core
	14	43.974	50.628	0.000	1.733	0.595	97.284	0.34	rim
	15	43.974	50.641	0.004	0.004	0.073	97.247	18.25	core
	16	43.974	50.778	0.000	4.407	1.048	98.167	0.24	rim
	17	43.974	50.445	0.002	0.010	0.185	96.263	18.50	core
	18	43.974	50.582	0.000	1.159	0.098	97.146	0.08	rim
	19	43.974	50.475	0.001	1.313	0.135	96.725	0.10	rim
	20	43.974	50.168	0.002	0.010	0.071	96.631	7.10	core
	21	43.974	50.588	0.006	0.008	0.072	97.155	9.00	core
	22	43.974	50.211	0.000	0.791	0.079	96.902	0.10	rim
	23	43.974	49.902	0.000	0.028	0.097	96.633	3.46	core
	24	43.974	50.312	0.006	1.225	0.129	96.747	0.11	rim
	25	43.974	50.126	0.009	0.051	0.135	96.532	2.65	core
	26	43.974	50.112	0.001	0.024	0.102	96.251	4.25	core
	27	43.974	50.256	0.005	0.081	0.118	96.170	1.46	core
	28	43.974	50.430	0.000	3.411	0.132	97.047	0.04	rim
	29	43.974	50.017	0.011	0.106	0.179	96.193	1.69	core
	30	43.974	50.231	0.000	0.011	0.078	96.900	7.09	core
	31	43.974	50.630	0.002	0.993	0.079	97.493	0.08	rim
	32	43.974	50.466	0.001	0.004	0.082	96.976	20.50	core
	33	43.974	50.107	0.002	0.017	0.074	96.082	4.35	core
	34	43.974	50.563	0.004	3.226	0.215	97.202	0.07	rim
	35	43.974	50.517	0.000	4.143	0.281	97.992	0.07	rim
	36	43.974	50.406	0.000	0.004	0.085	97.149	21.25	core
	37	43.974	50.455	0.000	0.007	0.094	97.042	13.43	core
12;003-4g	1	43.974	53.959	0.028	0.148	0.307	100.656	2.07	core
	2	43.974	53.321	0.023	0.006	0.031	99.445	5.17	core
	3	43.974	54.515	0.013	0.011	0.015	101.425	1.36	core
	4	43.974	54.737	0.012	3.251	0.261	101.896	0.08	rim
	5	43.974	54.393	0.531	1.614	0.147	101.373	0.09	rim

6	43.974	54.496	0.013	0.134	0.007	101.388	0.05	core
9	43.974	54.490	0.016	0.075	0.037	101.568	0.49	core
10	43.974	54.422	0.005	0.536	0.007	101.174	0.01	rim
11	43.974	54.637	0.024	3.348	0.176	101.767	0.05	rim
12	43.974	54.192	0.032	0.030	0.091	100.745	3.03	core
13	43.974	54.689	0.021	0.007	0.007	101.685	1.00	core
14	43.974	53.869	0.015	0.006	0.003	100.408	0.50	core
17	43.974	54.666	0.009	0.776	0.063	101.805	0.08	rim
18	43.974	53.930	0.017	0.088	0.095	100.667	1.08	core
19	43.974	54.829	0.012	0.976	0.018	101.957	0.02	rim
20	43.974	53.251	0.028	0.056	0.033	98.665	0.59	core

Note: Ni and Co values are plotted in Fig. 4.1. Zones were defined using RL microscopy and TE maps.

Appendix C8: SIMS results of zoned pyrite grains

TABLE C8. SIMS RESULTS OF ZONED PYRITE GRAINS SHOWING THEIR S-ISOTOPIC COMPOSITION.

Sample	Analysis Nr.	34S/32S	δ^{34}S 1sd (‰)	δ^{34}S (‰)	Zone
12;003-4g	Grain1@1	0.0443	0.046	2.495	massive core
	Grain1@2	0.0443	0.031	2.369	massive core
	Grain1@3	0.0432	0.044	-22.725	low-TE rim
	Grain1@4	0.0432	0.040	-21.944	high-TE rim
	Grain2@1	0.0443	0.030	2.000	massive core
	Grain2@2	0.0442	0.057	0.485	massive core
	Grain2@3	0.0432	0.036	-20.762	high-TE rim
	Grain2@4	0.0432	0.034	-22.526	low-TE rim
	Grain2@5	0.0432	0.041	-22.025	low-TE rim
	Grain3@1	0.0441	0.033	-0.987	massive core
	Grain3@2	0.0433	0.038	-20.122	high-TE rim
	Grain3@3	0.0432	0.037	-21.145	high-TE rim
	Grain3@4	0.0432	0.034	-22.594	low-TE rim
	Grain4@1	0.0441	0.029	-1.139	massive core
	Grain4@2	0.0432	0.037	-22.368	low-TE rim
	Grain4@3	0.0437	0.036	-10.473	transitional
	Grain4@4	0.0431	0.040	-23.059	low-TE rim
	Grain4@5	0.0433	0.044	-18.676	high-TE rim
	Grain5@1	0.0441	0.029	-2.204	massive core
	Grain5@2	0.0441	0.028	-1.805	massive core
	Grain5@3	0.0431	0.034	-23.236	low-TE rim
	Grain6@1	0.0440	0.030	-3.554	porous core
	Grain6@2	0.0434	0.045	-16.693	transitional
	Grain6@3	0.0432	0.029	-22.631	low-TE rim
	Grain7@1	0.0438	0.054	-8.404	transitional
	Grain7@2	0.0443	0.032	2.359	massive core
	Grain7@3	0.0442	0.033	0.993	massive core
	Grain7@4	0.0432	0.033	-21.243	high-TE rim
	Grain7@5	0.0442	0.028	1.631	massive core
	Grain7@6	0.0435	0.035	-15.709	transitional
	Grain8@1	0.0442	0.032	-0.094	porous core
	Grain8@2	0.0439	0.028	-6.882	transitional
	Grain8@3	0.0431	0.038	-23.754	low-TE rim
	Grain8@4	0.0431	0.029	-24.107	low-TE rim
	Grain8@5	0.0432	0.029	-21.555	high-TE rim
	Grain8@6	0.0432	0.028	-22.882	high-TE rim
	Grain10@1	0.0441	0.035	-2.032	massive core
	Grain10@2	0.0441	0.028	-0.519	massive core
	Grain10@3	0.0442	0.030	1.493	massive core
	Grain10@4	0.0431	0.043	-23.779	low-TE rim
	Grain10@5	0.0434	0.041	-16.518	transitional
	Grain10@6	0.0431	0.033	-23.356	low-TE rim

Grain11@1	0.0432	0.033	-21.009	high-TE rim
Grain11@2	0.0443	0.027	2.693	massive core
Grain11@3	0.0443	0.040	2.403	massive core
Grain11@4	0.0442	0.041	1.470	massive core
Grain11@5	0.0437	0.029	-10.072	transitional
Grain11@6	0.0431	0.028	-23.774	low-TE rim
Grain12@1	0.0443	0.030	2.354	porous core
Grain12@2	0.0432	0.036	-21.500	high-TE rim
Grain12@3	0.0432	0.044	-22.379	low-TE rim
Grain12@4	0.0432	0.033	-22.749	low-TE rim
Grain12@5	0.0432	0.028	-21.603	high-TE rim
Grain13@1	0.0442	0.045	0.526	massive core
Grain13@2	0.0442	0.036	0.657	massive core
Grain13@3	0.0431	0.041	-23.778	low-TE rim
Grain13@4	0.0432	0.031	-21.086	high-TE rim
Grain14@1	0.0436	0.060	-13.630	high-TE rim
Grain14@2	0.0441	0.034	-0.424	porous core
Grain14@3	0.0435	0.039	-14.897	transitional
Grain14@4	0.0443	0.027	2.315	massive core
Grain14@5	0.0443	0.027	3.105	massive core
Grain14@6	0.0443	0.035	3.254	massive core
Grain14@7	0.0435	0.047	-16.097	transitional
Grain14@8	0.0431	0.027	-22.973	low-TE rim
Grain14@9	0.0443	0.027	2.660	massive core
Grain14@10	0.0442	0.045	1.801	massive core
Grain14@11	0.0443	0.030	2.774	massive core
Grain14@12	0.0431	0.033	-23.479	low-TE rim
Grain15@1	0.0435	0.044	-15.720	high-Co rim
Grain15@2	0.0432	0.031	-22.469	low-TE rim
Grain15@3	0.0443	0.028	2.323	massive core
Grain15@4	0.0443	0.028	2.151	massive core
Grain15@5	0.0432	0.045	-21.817	high-TE rim
Grain16@1	0.0433	0.051	-18.483	high-Co rim
Grain16@2	0.0433	0.097	-20.451	high-TE rim
Grain16@3	0.0443	0.039	2.357	massive core
Grain16@4	0.0443	0.041	2.007	massive core
Grain16@5	0.0437	0.068	-10.942	transitional
Grain16@6	0.0432	0.034	-21.157	low-TE rim
Grain16@7	0.0443	0.035	1.984	massive core
Grain16@8	0.0442	0.037	1.716	massive core
Grain16@9	0.0432	0.032	-21.107	low-TE rim
Grain17@1	0.0432	0.046	-21.790	high-TE rim
Grain17@2	0.0442	0.054	-0.071	porous core
Grain17@3	0.0442	0.039	0.997	porous core
Grain17@4	0.0441	0.031	-0.516	porous core
Grain17@5	0.0431	0.035	-23.292	low-TE rim
Grain17@6	0.0434	0.031	-16.808	transitional
Grain17@7	0.0443	0.031	2.944	porous core
Grain17@8	0.0441	0.042	-1.214	porous core

	Grain17@9	0.0432	0.029	-22.443	low-TE rim
	Grain18@1	0.0431	0.040	-24.478	low-TE rim
	Grain18@2	0.0436	0.041	-11.924	transitional
	Grain18@3	0.0441	0.037	-0.487	porous core
	Grain18@4	0.0441	0.035	-0.353	porous core
	Grain18@5	0.0433	0.029	-19.180	high-TE rim
	Grain18@6	0.0437	0.040	-11.026	transitional
12;003-4a	Grain1@1	0.0431	0.028	-23.525	low-TE rim
	Grain1@2	0.0434	0.028	-17.392	high-TE rim
	Grain1@3	0.0437	0.028	-11.215	transitional
	Grain1@4	0.0434	0.028	-16.715	transitional
	Grain2@1	0.0432	0.028	-22.706	low-TE rim
	Grain2@2	0.0432	0.028	-22.682	low-TE rim
	Grain2@3	0.0432	0.028	-22.721	low-TE rim
	Grain2@4	0.0432	0.029	-21.295	high-TE rim
	Grain2@5	0.0443	0.028	3.335	porous core
	Grain2@6	0.0432	0.028	-22.284	low-TE rim
	Grain2@7	0.0432	0.028	-22.821	low-TE rim
	Grain2@8	0.0432	0.028	-21.202	high-TE rim
	Grain3@2	0.0432	0.028	-22.800	low-TE rim
	Grain3@3	0.0432	0.029	-20.825	high-TE rim
	Grain3@4	0.0441	0.035	-1.602	porous core
	Grain3@5	0.0432	0.028	-20.910	high-TE rim
	Grain3@6	0.0432	0.028	-21.270	low-TE rim
	Grain3@7	0.0442	0.028	0.224	massive core
	Grain4@1	0.0431	0.028	-24.347	low-TE rim
	Grain4@2	0.0432	0.028	-21.281	high-TE rim
	Grain4@3	0.0443	0.028	3.334	massive core
	Grain4@4	0.0444	0.028	4.242	massive core
	Grain4@5	0.0432	0.028	-21.258	high-TE rim
	Grain4@6	0.0432	0.028	-21.639	high-TE rim
	Grain4@7	0.0442	0.028	1.839	massive core
	Grain4@8	0.0443	0.028	3.638	massive core
	Grain4@9	0.0443	0.028	3.260	massive core
	Grain4@10	0.0431	0.028	-23.826	low-TE rim
	Grain5@1	0.0432	0.028	-21.049	high-TE rim
	Grain5@2	0.0442	0.029	-0.117	porous core
	Grain5@3	0.0441	0.028	-0.542	porous core
	Grain5@4	0.0432	0.028	-20.868	high-TE rim
	Grain6@1	0.0442	0.028	1.792	massive core
	Grain6@2	0.0443	0.028	2.084	massive core
	Grain6@3	0.0431	0.028	-23.116	low-TE rim
	Grain8@1	0.0432	0.028	-22.241	low-TE rim
	Grain8@2	0.0440	0.028	-4.291	porous core
	Grain8@3	0.0441	0.028	-2.490	porous core
	Grain8@4	0.0440	0.028	-3.483	porous core
	Grain8@5	0.0440	0.028	-3.545	porous core
	Grain8@6	0.0432	0.028	-22.480	low-TE rim
	Grain8@7	0.0432	0.028	-21.046	high-TE rim

Grain8@8	0.0440	0.028	-2.689	porous core
Grain8@9	0.0440	0.028	-4.048	porous core
Grain8@10	0.0440	0.029	-4.204	porous core
Grain8@11	0.0440	0.030	-3.145	porous core
Grain8@12	0.0432	0.028	-22.419	low-TE rim
Grain9@1	0.0433	0.028	-20.024	high-TE rim
Grain9@2	0.0442	0.027	1.225	massive core
Grain9@3	0.0441	0.027	-0.813	massive core
Grain9@4	0.0433	0.028	-20.221	high-TE rim
Grain9@5	0.0434	0.028	-17.414	transitional
Grain10@1	0.0431	0.028	-23.117	low-TE rim
Grain10@2	0.0442	0.027	0.526	massive core
Grain10@3	0.0442	0.027	0.619	massive core
Grain10@4	0.0442	0.027	0.604	massive core
Grain10@5	0.0432	0.028	-21.921	low-TE rim
Grain10@6	0.0431	0.028	-23.497	low-TE rim
Grain10@7	0.0441	0.028	-1.075	massive core
Grain10@8	0.0442	0.027	0.218	massive core
Grain10@9	0.0442	0.027	0.438	massive core
Grain10@10	0.0442	0.027	0.955	massive core
Grain10@11	0.0432	0.028	-21.206	high-TE rim
Grain11@1	0.0432	0.028	-20.810	high-TE rim
Grain11@2	0.0439	0.028	-5.262	porous core
Grain11@3	0.0439	0.028	-4.969	porous core
Grain11@4	0.0439	0.028	-4.978	porous core
Grain11@5	0.0433	0.028	-19.792	high-TE rim
Grain11@6	0.0431	0.028	-23.966	low-TE rim
Grain11@7	0.0432	0.028	-22.596	low-TE rim
Grain11@8	0.0439	0.028	-5.055	porous core
Grain11@9	0.0439	0.028	-4.957	porous core
Grain11@10	0.0439	0.028	-5.198	porous core
Grain11@11	0.0432	0.028	-21.140	high-TE rim
Grain11@12	0.0434	0.028	-16.990	high-Co rim
Grain12@1	0.0431	0.028	-23.861	low-TE rim
Grain12@2	0.0439	0.028	-6.961	transitional
Grain12@3	0.0442	0.027	-0.283	porous core
Grain12@4	0.0443	0.035	3.415	porous core
Grain12@5	0.0440	0.028	-3.244	porous core
Grain13@1	0.0440	0.028	-4.147	porous core
Grain13@2	0.0441	0.028	-1.422	porous core
Grain13@3	0.0441	0.028	-1.420	porous core
Grain13@4	0.0432	0.028	-21.271	high-TE rim
Grain13@5	0.0432	0.028	-22.615	low-TE rim
Grain13@6	0.0432	0.028	-22.641	low-TE rim
Grain13@7	0.0441	0.028	-1.407	porous core
Grain13@8	0.0441	0.028	-1.671	porous core
Grain13@9	0.0441	0.028	-1.608	porous core
Grain13@10	0.0431	0.028	-22.985	low-TE rim
Grain14@1	0.0431	0.028	-24.242	low-TE rim
Grain14@2	0.0432	0.028	-22.014	high-TE rim

Grain14@3	0.0440	0.028	-2.600	porous core
Grain14@4	0.0440	0.028	-2.738	porous core
Grain14@5	0.0441	0.028	-1.755	porous core
Grain14@6	0.0431	0.028	-23.173	low-TE rim
Grain15@1	0.0432	0.028	-22.557	low-TE rim
Grain15@2	0.0440	0.028	-3.083	porous core
Grain15@3	0.0440	0.028	-2.988	porous core
Grain15@4	0.0440	0.028	-2.835	porous core
Grain15@5	0.0432	0.028	-22.797	low-TE rim
Grain18@1	0.0431	0.028	-24.085	low-TE rim
Grain18@2	0.0432	0.028	-22.142	high-TE rim
Grain18@3	0.0443	0.028	2.759	porous core
Grain18@4	0.0443	0.028	3.250	porous core
Grain18@5	0.0432	0.028	-22.192	low-TE rim
Grain18@6	0.0433	0.028	-20.650	high-TE rim
Grain18@7	0.0443	0.028	2.056	porous core
Grain18@8	0.0443	0.028	3.066	porous core
Grain18@9	0.0436	0.028	-13.161	high-Co rim
Grain19@1	0.0431	0.028	-23.042	low-TE rim
Grain19@2	0.0443	0.028	2.647	massive core
Grain19@3	0.0443	0.028	2.933	massive core
Grain19@4	0.0443	0.028	2.614	massive core
Grain19@5	0.0432	0.028	-21.723	high-TE rim
Grain19@6	0.0431	0.028	-23.836	low-TE rim
Grain19@7	0.0431	0.028	-23.554	low-TE rim
Grain19@8	0.0432	0.028	-21.080	high-TE rim
Grain19@9	0.0442	0.028	1.270	massive core
Grain19@10	0.0442	0.028	0.613	massive core
Grain19@11	0.0432	0.028	-22.606	high-TE rim
Grain19@12	0.0431	0.028	-23.858	low-TE rim
Grain20@1	0.0442	0.028	1.958	porous core
Grain20@2	0.0441	0.028	-1.158	porous core
Grain20@3	0.0435	0.028	-15.981	transitional
Grain21@1	0.0431	0.028	-23.411	low-TE rim
Grain21@2	0.0443	0.028	2.959	porous core
Grain21@3	0.0443	0.028	2.032	porous core
Grain21@4	0.0432	0.028	-21.551	high-TE rim
Grain21@5	0.0432	0.029	-22.111	low-TE rim

Note: Values are plotted in Fig. 4.3. The positions of the spots were defined using EPMA TE maps.

Appendix C9: SIMS results of GM3-Bal

TABLE C9. SIMS RESULTS OF GM3-BALL (BALMAT PYRITE) STANDARD

Sample	Analysis Nr.	34S/32S	$\delta^{34}S$ 1sd (‰)	$\delta^{34}S$ (‰)
GM3-Bal 1	Std@01	0.044839	0.038	15.31
session 1	Std@02	0.044821	0.055	14.91
	Std@03	0.044832	0.037	15.16
	Std@04	0.044839	0.036	15.31
	Std@05	0.044830	0.031	15.11
	Std@06	0.044826	0.033	15.01
	Std@07	0.044831	0.039	15.13
	Std@08	0.044828	0.032	15.06
	Std@09	0.044829	0.038	15.09
	Std@10	0.044829	0.028	15.09
	Std@11	0.044829	0.028	15.07
	Std@12	0.044822	0.030	14.93
	Std@13	0.044826	0.028	15.01
	Std@14			
	Std@15	0.044824	0.032	14.96
	Std@16	0.044826	0.029	15.01
	Std@17	0.044834	0.034	15.19
	Std@18	0.044839	0.029	15.30
	Std@19	0.044822	0.037	14.92
	Std@20	0.044830	0.028	15.09
	Std@21	0.044831	0.028	15.13
	Std@22	0.044833	0.040	15.17
	Std@23	0.044835	0.035	15.23
GM3-Bal 2	std@1	0.0448	0.027	15.03
session 2	std@02	0.0448	0.027	15.07
	std@03	0.0448	0.027	15.12
	std@04	0.0448	0.027	15.20
	std@05	0.0448	0.027	15.22
	std@06	0.0448	0.027	15.00
	std@07	0.0448	0.027	15.19
	std@08	0.0448	0.027	14.92
	std@09	0.0448	0.027	15.05
	std@10	0.0448	0.027	15.18
	std@11	0.0448	0.027	15.04
	std@12	0.0448	0.027	15.13
	std@13	0.0448	0.027	15.26
	std@14	0.0448	0.027	15.15
	std@15	0.0448	0.027	15.06

	std@16	0.0448	0.027	14.99

Note: Session 1 relates to sample 12;003-4g; session 2 to sample 12;003-4a, respectively.

CV; Lebenslauf

Der Lebenslauf ist in der Online-Version aus Gründen des Datenschutzes nicht enthalten

Der Lebenslauf ist in der Online-Version aus Gründen des Datenschutzes nicht enthalten